2011

Mesoporous silica nanoparticles as smart and safe devices for regulating blood biomolecule levels

Yannan Zhao
Iowa State University

Mesoporous silica nanoparticles as smart and safe devices for regulating blood biomolecule levels

by

Yannan Zhao

A dissertation submitted to the graduate faculty

in partial fulfillment of the requirements for the degree of

DOCTOR OF PHILOSOPHY

Major: Chemistry

Program of Study Committee
Brian G. Trewyn, Major Professor
Nicola L. Pohl
Zhiqun Lin
Marek Pruski
Keith Woo

Iowa State University
Ames, IA
2011

TABLE OF CONTENT

ACKNOWLEDGEMENTS

First and foremost, I owe my deepest gratitude to my major professor Dr. Victor S.-Y. Lin. Dr. Lin exemplified everything a major professor and a great scientist should be. His perpetual energy and enthusiasm in research had motivated all his students, including me. Although he is no longer with us, his intelligence, creativity, dedication and his mentoring will continue to guide me spiritually throughout my life.

I would like to extend my sincere gratitude to my advisors Dr. Brian G. Trewyn and Dr. Igor I. Slowing, for guiding my research for the past several years and helping me with my degree completion. I am extraordinarily fortunate in having you both as my advisors and friends. Because of you, research life became smooth, rewarding and joyful for me.

My special thanks also go to my co-major professor Dr. Nicola L. Pohl and my POS committee members, Dr. Zhiqun Lin, Dr. Marek Pruski, and Dr. Kieth Woo, in no particular order, for their encouragement, insightful comments and valuable advice.

Many thanks to all the past and current group members for the stimulating discussions, for the time we were working hard together, and for all the fun we have had in the past five years. Thank you for making this laboratory a convivial place to work.

I greatly appreciate the U.S. National Science Foundation and the U.S. Department of Energy, Ames Laboratory for the funding of the projects in this dissertation.

Words fail me to express my appreciation to my parents, whose unflagging love, encouragement and support has helped develop the person I am today.

Lastly, my regards and blessings to all of those who have supported me in any respect during my research and thesis completion.

ABSTRACT

Stimuli-responsive end-capped MSN materials are promising drug carriers that securely deliver a large payload of drug molecules without degradation or premature release. A general review of the recent progress in this field is presented, including a summary of a series of hard and soft caps for drug encapsulation and a variety of internal and external stimuli for controlled release of different therapeutics, a discussion of the biocompatibility of MSN both *in vitro* and *in vivo*, and a description of the sophisticated stimuli-responsive systems with novel capping agents and controlled release mechanism.

The unique internal and external surfaces of MSN were utilized for the development of a glucose-responsive double delivery system end-capped with insulin. This unique system consists of functionalized MSNs capable of releasing insulin when the concentration of sugar in blood exceeds healthy levels. The insulin-free nanoparticles are then up taken by pancreatic cells, and release inside of them another biomolecule that stimulates the production of more insulin.

The *in vivo* application of this system for the treatment of diabetes requires further understanding on the biological behaviors of these nanoparticles in blood vessels. The research presented in this dissertation demonstrated the size and surface effects on the interaction of MSNs with red blood cell membranes, and discovered how the surface of the nanoparticles can be modified to improve their compatibility with red blood cells and avoid their dangerous side effects.

In order to optimize the properties of MSN for applying them as efficient intracellular drug carriers it is necessary to understand the factors that can regulate their internalization into and exocytosis out of the cells. The correlation between the particle morphology and aggregation of MSNs to the effectiveness of cellular uptake is discussed and compared with different cell lines. The differences in the degree of exocytosis of MSNs between healthy and cancer cells is reported and found to be responsible for the asymmetric transfer of the particles between both cell types.

The fundamental studies on the hemocompatibility, endo- and exocytosis of MSN along with its ability to sequentially release multiple therapeutics in response to different stimuli, allow us to propose MSN as an intravascular vehicle with a great potential for various biomedical applications.

CHAPTER 1. DISSERTATION ORGANIZATION

This dissertation is organized in seven chapters. The first chapter describes the organization of the dissertation. Chapters 2 to 6 are published journal articles and chapter 7 concludes this dissertation with summaries of the results.

Chapter 2 is a literature review describing the current state of the intravascular application of MSNs to the field of stimuli-responsive controlled release and intracellular drug/gene delivery, and the directions that research is expected to take in the following years. My personal contribution represents 90% of the work.

Chapter 3 presents a glucose-responsive double-delivery system for a sequential release of insulin and cyclic adenosine monophsphate (cAMP). This therapeutic system is highly appealing for its ability to simultaneously sense and regulate blood glucose levels. My personal contribution represents 90% of the presented research.

However, such system cannot be a candidate for clinical use unless its interactions with blood cells have been evaluated and controlled. Herein, chapter 4 describes the size- and surface-dependent interaction of MSNs with human red blood cell membranes, and shows, for the first time, how MSNs are internalized by red blood cells. My personal contribution represents 90% of the presented research.

A preliminary condition for using MSNs as controllable intracellular carriers is to understand the factors that regulate the efficiency of their cellular uptake and retention inside the cells. Chapters 5 and 6 are the studies that address these questions. Chapter 5 describes the effects of size and morphology of MSNs on their uptake by normal and cancerous cells.

Chapter 6 compares the abilities of healthy and cancerous cells to exocytose out MSNs. My personal contribution represents 20% of the work presented in each chapter.

This dissertation finished in chapter 7 with a general conclusion on the results and the significance of the research.

CHAPTER 2. CAPPED MESOPOROUS SILICA NANOPARTICLES AS STIMULI-RESPONSIVE NTROLLED RELEASE SYSTEMS FOR INTRACELLULAR DRUG/GENE DELIVERY

A paper published in ***Expert Opinion on Drug Delivery***, **2010**, *7*, 1013-1029.

Yannan Zhao, Juan L. Vivero-Escoto, Igor I. Slowing, Brian G. Trewyn and Victor S.-Y. Lin

ABSTRACT

Importance of the field: The incorporation of stimuli-responsive properties into nanostructured systems has recently attracted significant attention in the research of intracellular drug/gene delivery. In particular, numerous surface functionalized, end-capped mesoporous silica nanoparticle (MSN) materials have been designed as efficient stimuli-responsive controlled release systems with the advantageous "zero premature release" property.

Areas covered in this review: Herein, the most recent research progress on the design of biocompatible, capped MSN materials for stimuli-responsive intracellular controlled release of therapeutics and genes is reviewed. A series of hard and soft caps for drug encapsulation and a variety of internal and external stimuli for controlled release of different cargoes are summarized. Recent investigations on the biocompatibility of MSN both *in vitro* and *in vivo* are also discussed.

What the reader will gain: The reader will gain an understanding of the challenges for the future exploration of smart and biocompatible stimuli-responsive MSN devices.

Take home message: With a better understanding of the unique features of capped MSN and its behaviors in biological environment, these multifunctional materials will find a wide variety of applications in the field of drug/gene delivery.

1. Introduction

The parallel developments in the design of pharmaceutical drugs and in the controlled manipulation of materials at the nanometer scale have recently begun to merge in order to produce new generations of diagnostic and therapeutic agents. Many agents used for pharmacotherapy, such as antitumor drugs, show side effects and limited effectiveness that restrict their clinical application. To maximize therapeutic efficacy and minimize side effects, numerous efforts have been made on the design of target-specific drug delivery systems that can securely transport the medications to targeted cells and tissues, without degradation or untimely release.

Of the various drug nanocarriers explored, stimuli-responsive end-capped mesoporous silica nanoparticle (MSN) materials have demonstrated to be excellent candidates to fulfill the abovementioned requirements owing to their advantageous "zero premature release" property. This property is particularly useful when the drug to be delivered is toxic or its therapeutic dosage requires precise control. Conventional polymer-based drug delivery systems suffer from inherent problems including limited capacity of drug loading and poor stability in blood after injection and the difficulty in temporally controlling the release of matrix-encapsulated compounds, since it usually takes place immediately on dispersion of these materials. In contrast to traditional polymer-based "soft" nanomaterials, these highly stable inorganic MSN drug carriers are able to deliver a large payload of drug

molecules with much lower degradation kinetics. The use of capping agents controls the pore opening and closing so that the encapsulated cargoes could be released with precise temporal control. In addition, the unique internal and external surfaces of these materials make them ideally suited to the design of sophisticated drug delivery systems by incorporating one or more different diagnostic and therapeutic capabilities into a single vehicle with precise release control in response to one or more stimuli, either reversibly or non-reversibly. As illustrated in Figure 1, the internal mesopores of these materials can serve as a safe microenvironment where molecules can be loaded and protected from degradation or deactivation before entering target cells. Upon drug loading, the openings of the mesoporous channels can be blocked with a series of hard caps such as iron oxide (Fe_3O_4), cadmium sulfide (CdS) and gold nanoparticles (Au NPs), or soft caps including organic molecules, biomolecules and supramolecular assemblies, to prevent the drugs from leaching before reaching the targeted site. The external surface can be functionalized further with ligands capable of cell targeting and diagnosing disease.[1] In addition, the fact that these materials are readily taken up by animal and plant cells at low concentrations without posing any *in vitro* cytotoxicity,[2-4] or any apparent negative health effects *in vivo*,[5-8] makes these multifunctional nanoparticles promising candidates for target-specific stimuli-controlled delivery of therapeutics.

This review focuses on the latest developments of biocompatible, capped MSN with special attention given to sophisticated stimuli-responsive systems with newl capping agents and controlled release mechanisms designed for intracellular drug/gene delivery.

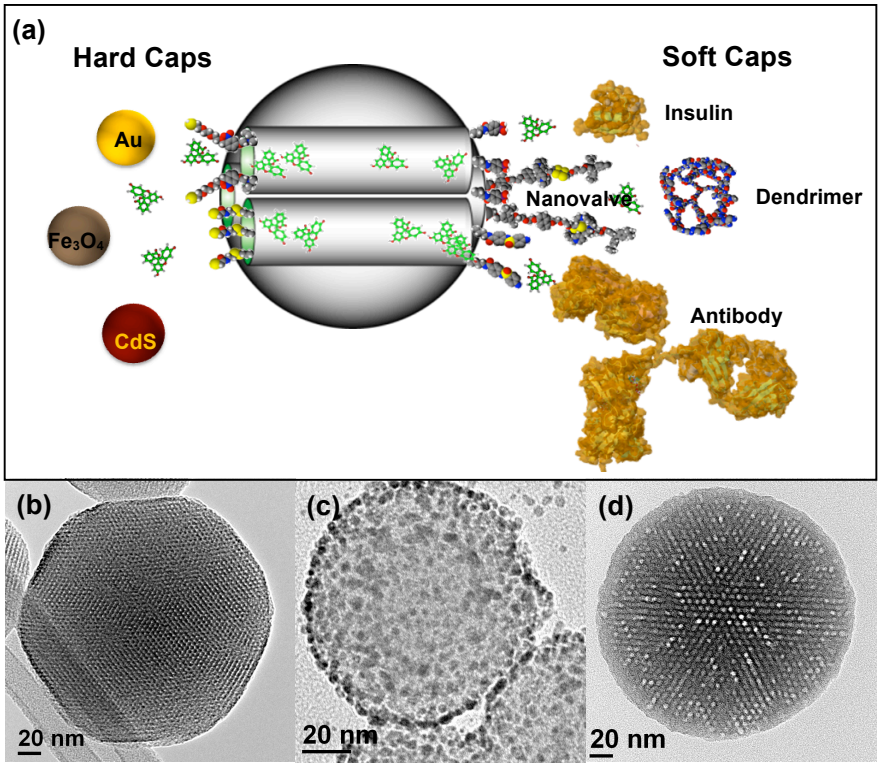

Figure 1. (a) Schematic representation of a MSN loaded with drugs and capped with hard and soft caps highlighted in this review. Transmission electron micrographs of (b) a MSN along the axis of the mesopores, (c) capped with hard (Au NP) and (d) soft (polymer) caps.

2. Intracellular delivery and biocompatibility of MSN

The first hexagonally ordered mesoporous silica material (designated as MCM-41) reported by researchers at the Mobil Oil Company consisted of micron-sized particles with variable morphology.[9] Whereas mesoporous silica microparticles are potentially useful for many non-biological applications such as adsorption, catalysis and chemical separations, they are not ideally suited for biotechnological and biomedical devices due to the large particle size and irregular morphology. For example, for these materials to serve as intracellular carriers for drug/gene delivery, they have to be efficiently internalized by mammalian cells, which require the particle size of the materials to be on the submicron scale.[10,11] In addition, microparticles are within the size window of many pathogens and could potentially trigger

acute immune responses when introduced *in vitro*. In the pursuit of biocompatible materials for controlled release and drug delivery applications, extensive research effort has been devoted to achieve control over particle size and morphology.

Mesoporous silica nanoparticles are prepared by a simple and rapid synthetic approach characterized by uniform particle size (80-500 nm) adjustable particle morphology, high surface areas (900–1100 m^2/g), large accessible pore volumes (0.5–1.5 cm^3/g), tunable pore size (2-10 nm), and a wide variety of surface functional groups that can be attached on the internal and external surfaces of MSNs to manipulate surface properties for drug loading and release.[12] The MSN shown in Figure 1b, for example, has a particle size around 150 nm with a hexagonal mesoporous structure, and pores around 2 nm in diameter, this material has a surface area around 900 m^2/g, and pore volume around 0.9 cm^3/g. Some reviews on the synthesis, size and morphology control and surface functionalization of MSN have been recently published.[13,14]

2.1. Intracellular uptake of MSN and *in vitro* biocompatibility

2.1.1. Intracellular uptake of MSN

After the first discovery by Lin and co-workers that MSNs were readily internalized by eukaryotic cells without inducing cytotoxicity and were capable of delivering DNA,[2] intensive efforts have been directed to understanding the mechanism of cellular uptake and various biological applications of MSN *in vitro*. Many different research groups have demonstrated that MSN can be rapidly and efficiently endocytosed by a variety of mammalian cells including cancer cells (HeLa, CHO, lung, PANC-1, breast cancer MCF-7, pancreatic RIN-5F), noncancer cells (neural glia, liver, endothelial, skin fibroblast), macrophage, stem cells (3TL3, mesenchymal) and others.[2,3,15-23]

To determine the efficiency and mechanism of the cellular uptake of MSN, several spectroscopic techniques have been used, including flow cytometry, confocal fluorescent microscopy, transmission electron microscopy (TEM), and differential interference contrast microscopy (DIC).[2,3,15-17,22,24] The uptake efficiency (EC_{50}) of MSN by mammalian cells range from 1 to 50 μg/ml, dependent upon the surface properties of the particles. The uptake occurs in a relatively short time frame, usually within 30 min of introduction of MSN into the culture medium.[3,25] By using confocal fluorescence microscopy, MSNs can be observed inside the cells and capable of escaping from endosomes to reach the cytosol (Figure 2d-f).[3] TEM micrographs also provide direct evidence on the internalization and subcellular localization of the particles (Figure 2a-c).[2] Recently, Lin, Yeung and co-workers followed the uptake of individual MSNs into single cells by DIC, in real time.[24]

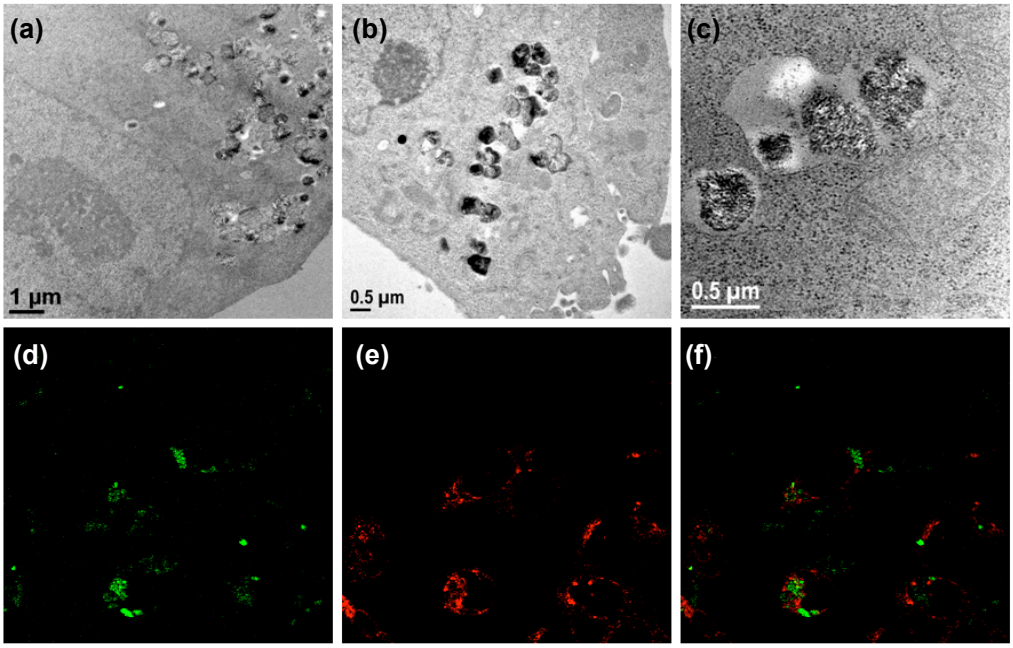

Figure 2. (a-c) Transmission electron microscopy images of CHO cell with endocytosed MSN. (d-f) Confocal fluorescence images of fluorescein labeled MSN (green, panel d) endocytosed by HeLa cells co-stained with an endosome marker (FM 4-64, red, panel e). The merged images (panel f) show little coincidence of green and red spots (giving yellow), indicating that MSN (green) have already escaped from the (red) endosomes.

As outlined below, various factors have been demonstrated to influence the efficiency, kinetics and mechanism of the intracellular uptake of MSN materials.

(1). *Surface property of MSN.* Lin and co-workers showed that the functionalization of the external surface of MSNs affects not only the efficiency of their internalization, but also the uptake mechanism and their ability to escape from the endosomal entrapment.[3] In general, positively charged MSNs have a higher endocytosis efficiency compared to negatively charged materials owing to the higher affinity to the negatively charged cell surface. The uptake of MSN has been found to take place mainly through a clathrin-mediated endocytosis, whereas some surface-functionalized MSNs, such as amine- and guanidinium-functionalized MSNs enter the cells through a clathrin- and caveolae-independent mechanism. In addition, a notable increase in the endocytosis efficiency by cancer cells was observed for folic acid grafted MSN by means of folic acid receptor-mediated endocytosis. It has also been observed that MSNs with a highly negatively charged surface can easily escape from endosomal entrapment as depicted in Figure 2d-f, probably attributed to the 'proton sponge effect'. Similar results were reported later by Mou and co-workers, and Linden and co-workers.[16,26]

2. *Particle size and aggregation ability.* The particle shape, size and agglomeration effect on the endocytosis of MSN has been investigated by the Lin research group.[21] The smaller particles with higher dispersibility in aqueous solution were shown to be endocytosed with a higher efficiency and faster kinetics than the larger particles. Later, Mou and co-workers also studied the effect of particle size on cellular uptake of MSNs, showing that the maximum uptake by Hela cells occurs at a particle size of 50 nm.[23]

3. *Particle morphology*. Lin and co-workers also reported that the cellular uptake of MSNs is morphology and cell line dependent.[21] A cancer cell line showed a higher endocytosis efficiency and rate for both spherical and tubular particles compared to a normal cell line. Interestingly, tubular MSNs achieved a more efficient uptake by cancerous and non-cancerous cells than the spherical ones. This was later confirmed by Tang and co-workers.[27]

All these factors lead to the conclusion that intracellular uptake of MSN can be regulated by choosing an appropriate nanoparticle formulation, which opens the possibilities of achieving high specificity and efficacy of the intracellular controlled delivery of therapeutic agents.

2.1.2. *In vitro* biocompatibility

The biocompatibility of MSN with cellular systems has been tested by different methods. Studies on the viability and proliferation of various mammalian cells indicate that these properties are not affected by MSN at dosages < 100 μg/ml even after 6 days of incubation.[2,3] Cell morphology and membrane integrity are conserved after the internalization of MSN as determined by microscopic analysis and selective DNA staining followed by flow cytometry.[3] Colorimetric assay with 3-[4,5-dimethylthiazol-2-yl]-2,5-diphenyltetrazolium bromide (MTT) shows that mitochondrial activity remains at normal levels after uptake of MSN.[16] However, the effects of MSN on diverse aspects of cellular metabolism still need to be more carefully and deeply evaluated. For example, although a number of studies have indicated that MSN internalization does not affect human mesenchymal stem cell (hMSC) morphology, viability, proliferation, and differentiation capacities,[25,28] Chen and co-workers have recently observed that the internalization of MSN

induces a significant but transient protein response (actin polymerization, small GTP-bound protein RhoA activation) and the generation of osteogenic signals in hMSCs.[29] Meanwhile, Goodisman, Asefa and co-workers also reported on the physical property-, concentration- and time-dependent effects of MSNs on cellular bioenergetics (cellular respiration and ATP content).[30] These findings suggest that more research efforts should be directed to the detailed characterizations of cellular activities with MSN internalization to provide comprehensive baseline information for the use of MSN as therapeutic drug carriers.

2.2. *In vivo* biocompatibility

Any clinical application of MSN is contingent on good biocompatibility. The small particle size of MSN allows for their use as intravenous drug delivery systems. However, one prerequisite for intravenous administration of MSN drug carriers is their biocompatibility with red blood cells. Lin and co-workers have recently reported that in contrast to the pronounced hemolytic activity of amorphous silica, MSNs exhibit high biocompatibility towards red blood cells at concentrations up to 100 μg/ml as shown in Figure 3.[4] By comparing the hemolytic activities of different surface functionalized MSNs and amorphous silica with the same surface functional groups, it was demonstrated that the enhanced biocompatibility of MSN with red blood cells is related to its unique honeycomb-like structure with arrays of mesopores where most silanol groups are hidden in the interior of the particles, resulting in a low surface density of silanols accessible to the cell membranes of red blood cells.

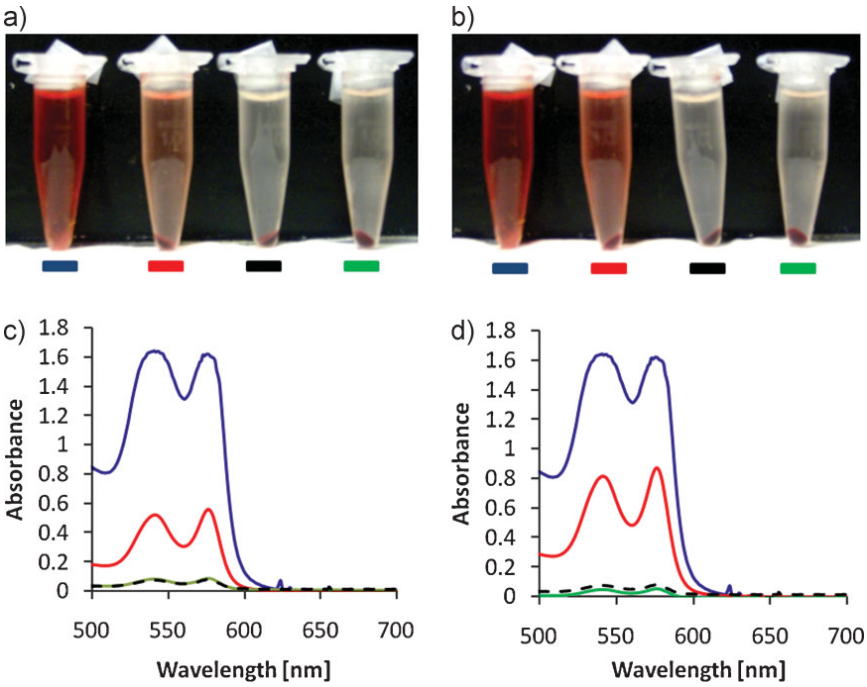

Figure 3. Hemolysis assay for amorphous silica (red lines) and MSN (green lines), compared with water as a positive control (blue lines) and PBS as a negative control (dashed black lines). The presence of hemoglobin (red) in the supernatant was detected visually (a, b) and by absorption at 541nm (c, d) after centrifugation of the cells. The materials were suspended at (a, c) 60 and (b, d) 100 mg/ml.

Additionally, recent investigations on the biodistribution and circulation properties of MSN in mice and rats demonstrated that the intravenous administration of these nanoparticles did not cause observable toxicity at doses < 200 mg/kg.[5-8,31] However, when the dosage is increased to > 200 mg/kg, toxic effects start to appear, as reported by Kohane and co-workers.[31] It should be noted that the dosage (1200 mg/kg) used in Kohane's study is two orders of magnitude higher than the one that would be necessary for drug delivery applications, especially considering the high drug loading capacity of MSN. Nevertheless, the biocompatibility of MSN could be further enhanced by surface functionalization. For example, PEGylated mesoporous silicates have been shown to be non-toxic in peripheral lung tissue.[32] Such surface coating strategy may also mitigate any systemic toxicity.

Hyeon and co-workers studied the biodistribution of the NPs (< 200 nm) in murine models of cancer, observing the accumulation of the NPs in tumors 24 h after injection. The authors attributed the localization to the enhanced permeability and retention (EPR) effect. They also observed NP accumulation in the rest of the organs, including liver and kidney, with no apparent toxicity.[6] In another study recently reported by Mou and co-workers,[8] the intravenous injection of MSN (50-100 nm, surface modified with positively charged groups) led to accumulation of the NPs mainly in the liver (35.3%), followed by the kidney (9.0%), lung (8.3%), spleen (8.0%), and heart (4.5%). In a long-term biodistribution study, they also observed the accumulation of MSNs in the liver for up to 3 months without any apparent toxicity, suggesting that MSNs are resistant to decomposition and biocompatible *in vivo* at low concentrations.[5] These interesting findings are promising steps towards the *in vivo* biomedical application of these multifunctional nanoparticles.

In a few words, MSN materials have demonstrated to be biocompatible drug carriers at dosage < 100 μg/ml for up to 1 week *in vitro* and < 200 mg/kg *in vivo* for up to 3 months. The final fate and long-term toxicity of MSNs should be investigated continuously before biomedical applications. Surface modifications should also be explored to reduce toxicity for applications in drug delivery and other biomedical fields.

3. Capped MSN-based stimuli-responsive controlled release systems

Since Vallet-Regí proposed using mesoporous silica materials for drug loading and release,[33] many mesoporous silica-based drug delivery systems have been studied and research efforts directed to attaining controlled release. The first capped mesoporous silica material for controlled release was reported by Tanaka and coo-workers.[34] A reversible

photo-triggered controlled release was developed by taking advantage of a photodimerization reaction of coumarin to control the opening and closing of the mesopores. However, these early applications were based on MCM-41 materials without defined shapes or monodispersed sizes. Short after Tanaka's report, Lin's research group prepared a CdS NP capped MSN for drug release, the uncapping of which was triggered by disulfide reducing agents.[35] The same research group later developed the first examples of using biocompatible MSNs as drug carriers and nanoparticles as capping agents for stimuli-responsive controlled release, the caps including chemically or physically removable nanoparticles such as Fe_3O_4 [17] and Au NPs.[18,36] In related works, Tseng, Nguyen and co-workers, designed a variety of stimuli-responsive nanovalves for the controlled release of dyes.[37-39] Although many of their early, established capping and release systems operated exclusively in non-aqueous solvents, they presented challenges in terms of the operational applicability under physiological conditions. Cyclodextrin (CD) and cucurbit[n]uril (CB[n]) were later used to increase the biocompatibility of the nanovalve systems.[40,41] However, intracellular drug delivery behaviors of these systems are still under investigation. Nevertheless, these systems greatly improved the diversity of capped mesoporous silica materials for stimuli-responsive controlled release with their "on-off" reversible control. Many excellent reviews of nanovalve-based mesoporous silica materials for controlled release have been written by Liong and co-workers.[42-44]

The cellular uptake and intracellular drug/gene delivery property of a capped MSN system was demonstrated for the first time by Lin and co-workers using G2-PAMAM-coated MSN as a vehicle to deliver plasmid DNA into astroglia, human and hamster cancer cells.[2] This system proved to be able to protect plasmid DNA against enzymatic digestion and

induce the expression of enhanced green fluorescent protein (EGFP) in cells more effectively than commercial transfection reagents. This work opened the door to the design of many stimuli-responsive polymer based soft caps and the investigation of drug delivery behavior of capped MSN systems inside cells. So far, only a few capped MSN systems have been applied to cellular systems for controlled drug/gene delivery and biocompatibility investigations,[2,17-20,36] which is fundamental for future cell- and organ-specific delivery of therapeutics and other *in vivo* applications.

In this review, the capping agents that were introduced onto mesoporous silica materials are classified as hard caps such as CdS, Fe_3O_4 and Au NPs and soft caps including organic molecules, biomolecules and supramolecular assemblies. This review is focused on those capped MSNs that have been designed and/or applied to the intracellular controlled release of drugs and genes (Table 1 and Figure 1a). Interestingly, among the various caps that have been exploited, biomolecules have emerged only recently as a new type of biocompatible capping agents for highly specialized tasks, including insulin for diabetes treatment, antibody for target-specific controlled release, and biotin-avidin for cell targeted drug delivery, as will be described later.

In general, stimuli-responsive capped MSN systems have the following three features that distinguish them from other drug delivery materials:

(1) Capped MSN can encapsulate a large payload of unmodified therapeutic compounds to achieve high intracellular concentrations, reducing undesired side effects resulting from leaching of the cargoes, and protecting the therapeutics from degradation by the environment. The mesoporous structure of MSN with tunable pore size offers the possibility of loading a large quantity of biogenic molecules, including antitumor drugs,

Table 1. Stimuli and triggers applied in capped MSNs for intracellular drug/gene delivery.

Stimuli			Trigger	Cap	Responsive moiety of linker or stalk	Ref
Internal Stimuli	pH		Acid	Poly-(dimethydiallylammonium chloride) (PDDA)	Carboxylic acid	45
			Acid	Cyclodextrin (CD)	Polyethyleneimine (PEI)	46
			Acid	Cucurbit[6]uril (CB[6])	Trisammonium	47
			Acid	CB[6]	Dialkyl-4,4'-bipyridinium (viologen)	48
			Acid	Borate	Saccharide	49
	Temperature		Temperature increase	Poly(N-isopropylacrylamide) (PNIPAM)	Thermoresponsive polymer	50,51
	Redox		Dithiothreitol (DTT), Mercaptoethanol (ME)	CdS NP	Disulfide	35,52
			DTT, Dihydrolipoic acid (DHLA)	Fe_3O_4 NP	Disulfide	17*
			DTT	Au NP	Disulfide	36*
			DTT, tris(2-carboxyethyl)phosphine (TCEP)	Polyamidoamine (PAMAM) dentrimer	Disulfide	2,52*
			DTT	crosslinked Poly(N-acryloxysuccinimide) (PNAS)	Disulfide	53
			DTT	Polyelectrolyte multilayers PEM-aptamer	Disulfide	20*
	Biomolecule	Enzyme	Porcine liver esterase (PLE)	α-CD	Ester-linked adamantyl stopper	41
			β-D-Galactosidase	Lactose	Glycosidic bond	54
			Protease (trypsin)	Biotin–Avidin	Avidin	55
		Blood sugar	Glucose	G-Insulin	Phenylboronic acid	19*
		Antigen	Sulfathiazole (STZ)	Antibody	Hapten	56
External stimuli	Light		UV light	Au NP	o-Nitrobenzyl ester	18*
			UV light	β-CD	o-Nitrobenzyl ester	57
			UV light	Py-β-CD	Azobenzene stalks	58
	ultrasound		ultrasound	ferrocene	Amide	59
	Electric field		Voltage	β-CD	Ferrocene	60
Double/Multiple Stimuli			Visible light, pH	Carboxylate-terminated G1.5 PAMAM	Spiropyran	61
			UV, pH	Au NP	Phenylboronic acid	62
			UV, pH	CB[6], Azobenzene Nanoimpeller	Trisammonium	63
			UV, DTT, α-CD	cross-linked β-CD-bearing PNAS	Diazo, Disulfide	64
			α-amylase, lipase, UV	β-CD	CD, ester, o-nitrobenzyl ester	65

* Intracellular drug/gene release and *in vitro* biocompatibility have been tested with mammalian/plant cells.

imaging dyes, DNA, proteins and other chemicals of pharmaceutical interest, and in particular those that are cell membrane-impermeable or incompatible with biological fluids. In a typical cargo loading process, MSNs functionalized with organic groups (linkers) are incubated with concentrated drug solution to facilitate the diffusion of drug molecules into the mesopores of MSN. Capping agents are then added to the solution to block the pore entrance by forming covalent bonds or through electrostatic interaction with the linkers on the surface of MSN, so that loaded cargoes are prevented from leaching out of the mesopores. Physisorbed drug molecules could be washed off and the loading could be calculated by subtracting the amount of cargoes remaining in the solution and that has been washed off from the initial concentrated drug solution. Typically, the amount of cargoes that can be loaded in the mesoporous channels of MSN varies from 0.2 to 50 μmol/g. In contrast to conventional drug carriers that require covalent attachment of therapeutic compounds to their matrices, capped MSN system does not require any modification of the drug molecules but physically traps them inside the mesopores. Capping prevents the loaded species from leaching out and allows drug release only in the presence of specific stimuli that trigger the removal of the caps. In this aspect, the structural integrity and consequently the pharmacological property of encapsulated drugs can be retained. These encapsulation methods make possible the simultaneous delivery of one or more therapeutic agents to achieve synergistic therapeutic outcomes. Furthermore, the pharmacokinetic properties and biodistribution of the payloads can be controlled by manipulating the surface properties of the capped MSN carrier.

(2) The capping agent can provide extra functionality to the MSN drug carrier, such as cell targeting, facilitating endosomal escape, loading more therapeutics and serving as

diagnostic agents. For example, by using superparamagnetic iron oxide nanoparticles as removable caps for MSN,[17] Lin and co-workers were able to manipulate cells that had internalized Fe_3O_4-MSN by applying an external magnetic field. The combination of this magnetic motor effect with the stimuli-responsive controlled release property, also demonstrated for this capped MSN, showed that it was possible to direct therapeutic agents to cells or tissues of interest by loading them inside of the material. Gold nanoparticles have also been well established as hard caps for MSN.[18,36] Besides their role as biocompatible caps, AuNPs can also increase the density of individual MSN to enable their use with a gene gun system. In that way Lin, Wang and co-workers were able to demonstrate for the first time the ability of AuNP capped MSN to act as a co-delivery agent of a gene and its promoter into plant cells (Figure 4).[36] The laser-induced plasmonic heating property of AuNPs was utilized for triggering drug release in addition to other stimuli-cleavable chemistries. This has been demonstrated recently by Martínez-Máñez in a pH and NIR laser-controlled delivery system.[62] The local plasmonic heating induced by a NIR laser resulted in the cleavage of the boronic ester linkage between the AuNPs and the MSN, allowing the release of entrapped Safranine O molecules. The cap itself could also play a role in therapeutic treatment. For example, insulin is known to regulate blood glucose level in the treatment of diabetes. In a glucose-responsive double delivery system recently published by the Lin group, gluconic acid modified insulin (G-Insulin) was employed both as a cap to control the delivery of cyclic AMP to pancreas beta-cells and as a therapeutic agent to directly regulate blood glucose levels (Figure 5).[19]

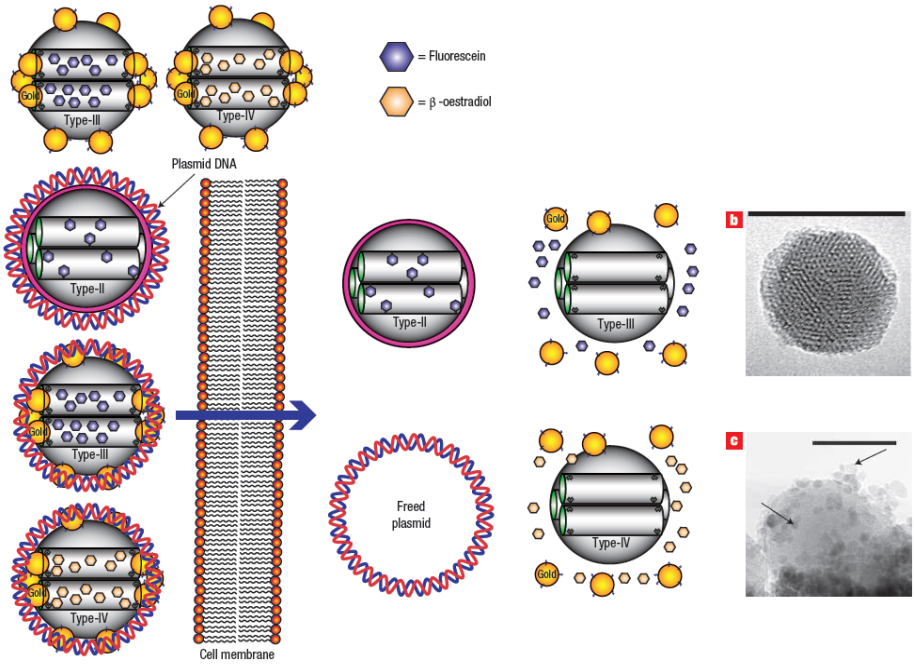

Figure 4. Schematic representation of a series of surface-functionalized MSNs for intracellular controlled release of genes and chemicals into plant cells triggered by addition of reducing agent, DTT.

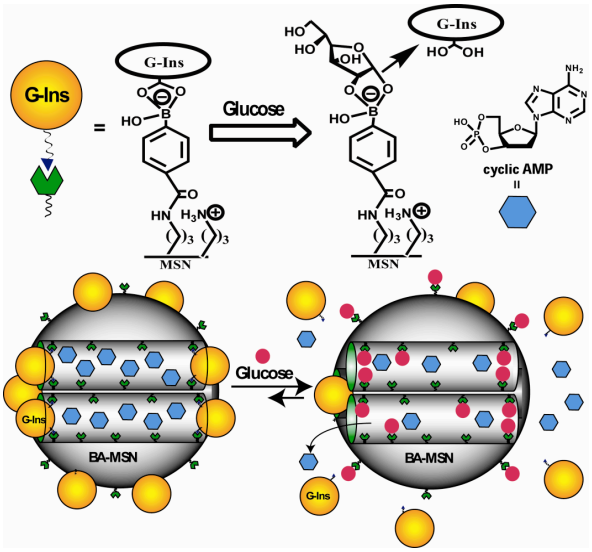

Figure 5. Schematic representation of the glucose-responsive MSN-based double delivery system for controlled release of bioactive G-Ins and cyclic AMP. The controlled release mechanism was achieved by means of the displacement reaction between blood glucose and G-Ins based on reversible boronic acid-diol complexation. High glucose concentration triggers the G-Ins uncapping and the release of cyclic AMP sequentially to diminish the higher than normal level of blood glucose.

(3) The versatile and selective surface functionalization of MSN allows pore uncapping and drug release with a high degree of control. The introduction of one or more types of stimuli-responsive functional groups to the capped MSN system enables them to perform a series of special tasks on command, as will be described in the next section. The diffusion of encapsulated molecules can be controlled by selectively decorating the interior surface and by choosing appropriate caps; in other words, the release kinetics of drugs can be tuned to match the needs of the biological system of interest. For example, by using real-time imaging, Yeung, Lin and co-workers demonstrated that the kinetics and amounts of ATP encapsulated in MSN could be tuned by using different types of caps. The study revealed that hard nanoparticle caps such as CdS are more suitable for the fast release of relatively small amounts of payloads, whereas flexible soft caps such as PAMAM dendrimers are more convenient for slow and sustained release of larger amounts of cargoes.[52]

Above all, the ability to independently functionalize each section of capped-MSN (interior surface, exterior surface and caps), along with the good biocompatibility and tunable endocytosis efficiency, makes these capped-MSN materials with multiple, orthogonal and controllable functions for biomedical applications.

4. Stimuli-responsive controlled release mechanisms

To achieve precise spatial and temporal delivery of therapeutic agents to target sites, a variety of stimuli-responsive groups have been introduced to MSN, including groups that respond to stimuli found in the interior of biological systems (pH, temperature, redox potential, and biomolecules) and stimuli that can be applied externally from biological

systems (light, ultrasound, electrical field). Various responses to stimuli are feasible, including bond cleavage, competitive binding, and conformational changes. Capped-MSN systems are designed to take advantage of these responses and to trigger the release of encapsulated molecules. An overview of stimuli and triggers that have been applied to capped mesoporous silica materials for controlled release and intracellular drug/gene delivery are given in Table 1. In this section, we analyze the most recent stimuli-responsive controlled release systems found in the literature, with a particular focus on biomolecule, light and double responsive controlled release systems.

4.1. Internal stimuli-responsive controlled release

Stimuli-responsive controlled release systems are especially advantageous when the triggering stimuli are unique to the targeted pathology. This allows the drug carriers to respond specifically to the desired species and release drugs in a self-regulated fashion. Examples of internal stimuli that have been exploited for intracellular drug and gene delivery include pH, temperature, redox state and some specific biomolecules such as enzymes, carbohydrates and antigens.

4.1.1. pH

The acidic pH found in tumor and inflammatory tissues (pH ~ 6.8) as well as in the endosomal and lysosomal compartments of cells (pH ~ 5-6) provides a potential internal trigger for the release of drugs from a pH-responsive drug carrier .[66] To exploit this condition the carrier must be stable at physiological pH (~7.4) but release their encapsulated payload in acidic environments. A series of pH-responsive caps including polyelectrolyte, pseudorotaxanes and organic molecules have been used for controlling the release of drug molecules, as summarized in Table 1.[45-48] Although exciting, none of these systems have

been tested with cells or animals for intracellular pH-responsive controlled release; Possibly due to the weak response of these systems at mildly acidic conditions.

4.1.2. Temperature

Temperature is another internal stimulus that can be exploited for triggering drug/gene release at specific sites. For example, it has been shown that the local temperature in many tumors is slightly higher than normal body temperature. Therefore, a temperature-responsive drug carrier that releases drugs only at temperatures > 37 °C but keeps the drugs encapsulated while in circulation is highly desirable. Poly-(N-isopropylacrylamide) (PNiPAM) is a well-studied thermoresponsive polymer for controlled release studies. By growing PNiPAM on the external surface of MSN, Lin and co-workers were able to control thermally its partition between water and toluene, which could lead to applications in temperature dependent phase transfer and thermoresponsive controlled release in different solution environments.[67] López and co-workers prepared PNiPam coated mesoporous silica microparticles and demonstrated that the coated particles were able to absorb fluorescein from an aqueous solution at high temperature and release their cargo to a fresh solution upon temperature increase.[50,51] However, it should be noted that depending on the pore size of the particle, the drug loading and release behavior could be different.[68,69]

4.1.3. Redox potential

It is known that intracellular glutathione (GSH) levels in most tumor cells are 100–1000 fold higher than the extracellular levels, therefore the naturally occurring redox potentials between the mildly oxidizing extracellular space and the reducing intracellular space can be utilized as a stimulus to trigger the release of encapsulated molecules from drug carriers.[70] The potential of disulfide bonds to reduce into free thiols as a response to this

reductive condition has attracted much attention for the design of redox-responsive controlled release systems. This has been well established by the use of disulfide linked nanoparticles (CdS, Fe_3O_4 and Au NP)[17,18,35,36] and PAMAM dendrimers[2,52] as capping agents. Remarkably, these redox-responsive capped-MSN systems have been utilized as intracellular delivery devices for dyes, drugs and genes into mammalian and plant cells.[17,20,36]

In an effort to extend the applications of MSN as an intracellular delivery agent for plant cells, Lin and co-workers were able to deliver DNA and chemicals into plants by the use of Au NP-capped redox-responsive MSNs as depicted in Figure 4.[36] The MSN materials were first loaded with β-estradiol, which is a promoter for the activation of a green fluorescent protein (GFP) encoding plasmid DNA (GFP pDNA) to be delivered into the plant cells, and the pore entrances were then capped with Au NPs by means of a disulfide bond. The Au NP-capped MSN was then coated with the GFP pDNA and introduced into the plant cells by a gene gun. Interestingly, the plant cells could express the delivered gene only when the reducing agent was added by perfusion to induce the release of the entrapped β-estradiol for DNA activation. This demonstrated for the first time that MSN has the ability to co-deliver different chemicals into plant cells with a precise control of location, time and the sequence of release.

Later, the strategy of introducing disulfide bonds for redox-responsive controlled release was also used by Yang, Wang and co-workers, when they used it for the reversible crosslinking of a polyelectrolyte multilayer-coated MSN (MSN-PEM).[20] On addition of disulfide reducing agent dithiothreitol (DTT), they were able to observe the release of loaded fluorescein. Interestingly, a cancer-specific DNA aptamer was also attached to the MSN-PEM for targeted drug delivery. By comparing the endocytosis efficiency of aptamer-bound

MSN-PEM with the aptamer-free system, as well as the viability of cancer and the non-cancerous cells when incubated with these two materials loaded with anticancer drugs, they demonstrated cell-targeted redox-responsive controlled release ability of the aptamer-bound MSN-PEM.

4.1.4. Biomolecules

Biomolecules have recently emerged as a new type of internal stimulus that has attracted a growing interest owing to their biocompatibility and interesting biological activities. So far, the types of biomolecules that have been introduced to capped mesoporous silica materials include enzymes, blood sugars and antigens.

In a first proof-of-concept, Patel *et al.* developed an enzyme-responsive capped mesoporous silica material.[41] The material was loaded with luminescent rhodamine B (RhB) and capped with a [2]-rotaxane by threading β-cyclodextrin onto a polyethylene glycol stalk and held with an ester-linked adamantyl stopper. The release of RhB was observed only upon the addition of porcine liver esterase (PLE) resulting in the hydrolysis of the adamantyl ester, which led to the dethreading of the [2]-rotaxane. In another example, Bein and co-workers exploited biotin-avidin as a protease-responsive cap to encapsulate fluorescein molecules.[55] The controlled release was achieved by addition of the protease trypsin leading to the hydrolysis of the attached protein avidin and the release of the entrapped fluorescein dyes. Recently, Bernardos *et al.* developed a lactose-capped mesoporous silica support with RhB dye encapsulated and capped by a network of lactose linked by hydrogen bonding interactions.[54] The presence of β-D-galactosidase caused the hydrolysis of glycosidic bond in the anchored lactose leaving only a glucose derivative on the surface. This decrease in the size of the capping agent induced the release of the entrapped dye. In addition, β-amylase

and lipase have also been employed as triggers in a multiresponsive controlled release system, as will be described later.

Blood sugars have shown to be excellent biomolecular triggers by the Lin group in the development of a glucose-responsive double delivery system for sequential delivery of insulin and cyclic adenosine monophosphate (cAMP), as illustrated in Figure 5.[19] As mentioned above, G-insulin was exploited to encapsulate cyclic AMP inside mesopores and also served as a therapeutic agent to regulate blood glucose level. Phenylboronic acid linkers on the external surface of MSN could sense the glucose level and regulate the pore opening and closing. A competitive binding between G-insulin and saccharides with phenylboronic acid resulted in the G-insulin uncapping once a higher-than-normal blood glucose level was encountered. Surface zeta-potential change upon the G-insulin uncapping enhanced the cellular uptake of the material for efficient intracellular cAMP delivery. The fast insulin release (within 30 min) is especially important for diabetic patients requiring high dosage of insulin after meals, and the sustained intracellular release of cAMP can induce insulin production from pancreas beta cells in between meals for a long term effect. This co-delivery system with control over the sequence of release is particular attractive for biomedical applications.

Also, antigens were also exploited as biomolecule-based stimuli for triggering drug release from an antibody-capped mesoporous silica nanocarrier.[56] Martínez-Máñez and co-workers attached a hapten linker to the external surface of a $Ru(bipy)_3^{2+}$ dye loaded mesoporous silica and capped the pores with a polyclonal antibody. A selective uncapping of the pores with consequent release of the dye was observed by addition of sulfathiazole

(STZ) antigen by means of a displacement reaction. The use of bio-controlled drug delivery systems is highly appealing for a wide variety of biomedical applications.

4.2. External stimuli-responsive controlled release

4.2.1. Light

Light is very attractive as a remote control for the site-specific delivery of drugs. In principle, the release of entrapped molecules can be rapidly induced on exposure to light at a specific time and location without any change in the chemical environmental. Suitable chromophores, such as azobenzene,[58,63,64] spiropyran,[61] and a photocleavable linker o-nitrobenzyl ester[18,57,65] have been incorporated into capped MSN systems to render them susceptible to light for photo-responsive controlled release.

Recently, Kim and co-workers have reported a photoresponsive cyclodextrin-capped MSN by the introduction of a photocleavable o-nitrobenzyl ester linker. On irradiation at 350 nm this system was able to release preloaded calcein.[57] At the same time, a photoresponsive Au NP-capped MSN was reported by Lin *et al*, as shown in Figure 6.[18] The gold nanoparticles were functionalized with the photocleavable linker thioundecyl-tetraethyleneglycoestero-nitrobenzylethyldimethyl ammonium bromide (TUNA), and were incorporated onto the MSN surface by means of electrostatic interaction. On irradiation with UV light, TUNA is converted to the negatively-charged thioundecyltetraethyleneglycol-carboxylate (TUEC), leading to the dissociation of the Au NPs from the MSN surface owing to charge repulsion, with the consequent release of the cargo from the mesopores. This system was then loaded with the anticancer drug paclitaxel and administered to fibroblast and liver cells. The drug loaded MSN were readily endocytosed by the cells without inducing any cytotoxicity, indicative of “zero premature release”. On irradiation under biocompatible

conditions, the preloaded drugs were released leading to significant cell death. An alternative approach by Ferris *et al.* took advantage of the difference between the binding affinity of β-CD with the *cis* and *trans* isomers of azobenzene to control the release of cargo molecules from MSN.[58] Irradiation of azobenzene stalks with 351 nm light induced the isomerization from the *trans* to the *cis* isomer, resulting in the β-CD rings dethreading from the stalks and releasing a previously loaded cargo.

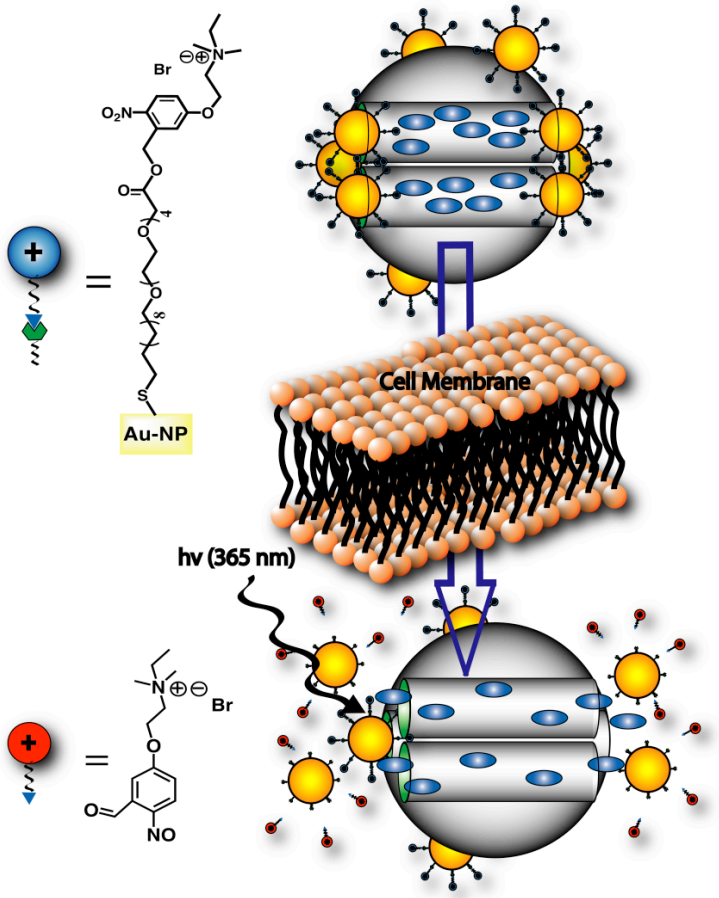

Figure 6. Schematic representation of a photoresponsive gold nanoparticle-capped MSNs. Upon UV irradiation, the photolabile linker on the Au NPs was cleaved, changing the surface charge property (zeta-potential) of these gold nanoparticles from positive to negative. The charge repulsion between the Au NPs and MSN would then uncap the mesopores and allowed the release of guest molecules.

4.2.2. Other external stimuli

Ultrasound can also serve as a stimulus to trigger the release of drugs and to achieve the targeted delivery by local sonication. An ultrasound-responsive MSN system was recently developed by Kwon and Lee by means of amide bond coupling of a carboxy substituted ferrocene complex and an aminopropyl functionalized MSN.[59] They demonstrated that the complex could be cleaved on ultrasound irradiation, consequently opening the pores of MSN.

Redox-responsive drug carriers may also find applications in the externally controlled release of drugs by applying electric current. For example, Khashab *et al.* used the inclusion complex between β-CD and ferrocene to encapsulate Rhodamine B.[60] By applying a voltage (+1 V) to the solution, ferrocene threads were oxidized to the positively charged ferrocenium ions, resulting in the dethreading of the β-CD macrocycles and release their cargo.

4.3. Double stimuli-responsive controlled release

Dual-controlled or multiresponsive controlled release systems are able to use two or more stimuli either in an independent or in a synergistic fashion, which opens the possibility for developing more complex controlled release behaviors.

The first dual-controlled system was reported by Martínez-Máñez and co-workers based on the use of a spiropyran photochrome. The compound they used can be reversibly transformed from a neutral spiropyran structure into a positively charged merocyanine by irradiation with UV light. The merocyanine form is stable when kept in the dark but converts into the spiropyran on irradiation with visible light or by heating.[61] The researchers anchored the positive merocyanine moieties to the pore entrance of mesoporous silica and added carboxylate-terminated G1.5 PAMAM to block the pores via electrostatic interaction. Two

responses were established for this system: photo-responsiveness, achieved through merocyanine transformation to the neutral spiropyran form by irradiation with visible light; and pH-responsiveness by decreasing the pH to neutralize the carboxylate groups of the dendrimer. Both stimuli proved to be capable of disrupting the electrostatic interaction between the negatively charged dendrimer and the positively charged merocyanine-functionalized surface, leading to the release of preloaded dye molecules. The same authors demonstrated recently a pH and photoresponsive Au NP-capped mesoporous silica material.[62] The interaction between boronic acid functionalized Au NP and saccharide-derivatized mesoporous silica surface could be reversibly regulated by pH due to the formation of boronic esters. The laser-induced plasmonic heating properties of Au NP account for the photoresponsiveness of this system.

Another pH and photo-responsive controlled release system based on the combination of pH-responsive nanovalves and light-responsive nanoimpellers was reported recently by Angelos *et al.*[63] They demonstrated that the release of the encapsulated molecules requires activation of both stimuli, acting as an AND logic gate. Feng and co-workers published a multiresponsive supramolecular capped mesoporous silica system by grafting β-CD-bearing polymer on the surface of mesoporous silica and cross-linking by the addition of disulfide-groups to form a polymeric network that blocked the pores.[64] They demonstrated the release of preloaded calcein dye on UV irradiation, on addition of α-CD and on the introduction of disulfide reducing agents such as DTT, causing the isomeric transformation of azobenzene groups, displacement of β-CD by α-CD, and cleavage of disulfide bond between β-CD and polymer main chains, respectively. In addition, an enzyme- and photoresponsive cyclodextrin-capped MSN was established by Kim and co-workers.[65] The CD was anchored

on the MSN surface through an *o*-nitrobenzyl ester containing stalk, which could be ruptured by UV irradiation or hydrolyzed by lipase. Besides, the CD caps could also be degraded by α-amylase, allowing enzyme- and photoresponsive controlled release of guest molecules.

5. Conclusion

The development of several capped MSN systems containing stimuli-responsive linkers has shown promising properties for the intracellular delivery of drugs and nucleic acids. Capped MSN-based controlled release systems are continuously evolving, giving rise to newer, more sophisticated multifunctional devices that are gradually approaching a state at which their biomedical application is imminent. It is particularly encouraging to witness the fast expansion of capping agents and controlled release mechanisms introduced to MSN drug carriers, which now includes the use of bioactive molecules (insulin, antibody and biotin-avidin) as capping agents and biomolecules of pharmaceutical interest (blood sugar, antigens, and enzymes) as triggers. It is also remarkable to observe that one or more types of stimuli, drugs or other functionality have been integrated into single MSN carriers to achieve highly specialized delivery tasks. The recent studies on the biocompatibility of these materials both *in vitro* and *in vivo* also lead us to believe that these stimuli-responsive capped MSN materials will find a wide variety of applications in the field of cell targeted and organ specific drug and nucleic acids delivery.

6. Expert opinion

Major efforts have been put forth to create increasingly sophisticated stimuli-responsive MSN materials that release one or more therapeutics with ever more control.

Significant challenges remain, however, since the controlled release properties of many of the existing stimuli-responsive capped MSN systems are yet to be tested with living cells or tissues, and most of them have not been tested in organisms. Furthermore, some systems have minimal potential to succeed as vehicles for therapeutics unless significant improvements are performed to increase their response to real biological conditions. For example, some of the reported pH-responsive capped MSNs require relatively strong acidic environments (pH < 5) for pore opening and drug release, which is not compatible for *in vitro* or *in vivo* drug delivery. Although there is now a large number of release mechanisms available, the field remains open for the discovery of even more internal and external stimuli to expand the diversity of triggers for release by capped MSN. This progress will certainly provide even higher degrees of specificity and control in drug delivery by capped MSN. It is worthwhile to highlight that biomolecules with advantageous biocompatibility and selectivity properties have been actively investigated both as triggers and as capping agents in the recent years. Still, reports on biomolecular caps are rare throughout the literature. More work is necessary to enlarge this promising area of the field.

The introduction of switchable properties to these stimuli-responsive capped MSN is another subject for future development. Many of the established systems release drugs on uncapping irreversibly, which limits their applications. Besides using capping agents that can be reversibly controlled, switches could also be created by using guest molecules that interact with the capping agents or other sensing moieties once released, providing a closed feedback loop capable to self-regulating the amount and rate of the release. Introducing such a reversible control to these materials will lead to active smart drug delivery devices.

It is also of particular interest to develop new biocompatible, capped MSN systems for intracellular delivery of bioactive molecules to reduce or enhance certain cellular activities. Intracellular delivery of cyclic AMP to stimulate insulin production[19] and the release of gene expression promoter β-estradiol inside cells for DNA activation[36] are examples of such a goal. Although a great number of anticancer drugs and imaging dyes have been loaded and released, the demonstration of controlled release of biogenic molecules, such as genes, enzymes and proteins, and other molecules of pharmaceutical interest are still scarce. In the future, it will be highly desirable to design a drug carrier that could be efficiently internalized by specific cells and participate in a variety of biochemical or catalytic reactions inside of cells. Much work still lies ahead in developing such smart and biocompatible, capped MSN devices.

Despite recent encouraging progress in improving the biocompatibility of these materials, most of today's materials are still investigated outside biological systems. In other words, what sets today's synthetic materials apart from *in vivo* biomedical applications of tomorrow are the lack of proof on biocompatibility, cellular uptake and intracellular controlled release properties of these capped MSN materials. Further work is required in order to fully understand how these systems function both *in vitro* and *in vivo*. As more biocompatibility and drug delivery data both *in vitro* and *in vivo* become available, it is envisaged that these multifunctional stimuli-responsive capped MSN systems will be playing a key role in clinical and other biomedical and biotechnological applications.

REFERENCES

(1) Tsai, C. P.; Chen, C. Y.; Hung, Y.; Chang, F. H.; Mou, C. Y. *J. Mater. Chem.* **2009**, *19*, 5737.

(2) Radu, D. R.; Lai, C.-Y.; Jeftinija, K.; Rowe, E. W.; Jeftinija, S.; Lin, V. S. Y. *Journal of the American Chemical Society* **2004**, *126*, 13216.

(3) Slowing, I.; Trewyn, B. G.; Lin, V. S. Y. *Journal of the American Chemical Society* **2006**, *128*, 14792.

(4) Slowing, I. I.; Wu, C.-W.; Vivero-Escoto, J. L.; Lin, V. S. Y. *Small* **2009**, *5*, 57-62.

(5) Wu, S.-H.; Lin, Y.-S.; Hung, Y.; Chou, Y.-H.; Hsu, Y.-H.; Chang, C.; Mou, C.-Y. *ChemBioChem* **2008**, *9*, 53.

(6) Kim, J.; Kim, H. S.; Lee, N.; Kim, T.; Kim, H.; Yu, T.; Song, I. C.; Moon, W. K.; Hyeon, T. *Angewandte Chemie, International Edition* **2008**, *47*, 8438.

(7) Taylor, K. M. L.; Kim, J. S.; Rieter, W. J.; An, H.; Lin, W.; Lin, W. *Journal of the American Chemical Society* **2008**, *130*, 2154.

(8) Lee, C.-H.; Cheng, S.-H.; Wang, Y.-J.; Chen, Y.-C.; Chen, N.-T.; Souris, J.; Chen, C.-T.; Mou, C.-Y.; Yang, C.-S.; Lo, L.-W. *Advanced Functional Materials* **2009**, *19*, 215.

(9) Kresge, C. T.; Leonowicz, M. E.; Roth, W. J.; Vartuli, J. C.; Beck, J. S. *Nature (London, United Kingdom)* **1992**, *359*, 710.

(10) Mayor, S.; Pagano, R. E. *Nature Reviews Molecular Cell Biology* **2007**, *8*, 603.

(11) Rejman, J.; Oberle, V.; Zuhorn, I. S.; Hoekstra, D. *Biochemical Journal* **2004**, *377*, 159.

(12) Huh, S.; Wiench, J. W.; Yoo, J.-C.; Pruski, M.; Lin, V. S. Y. *Chemistry of Materials* **2003**, *15*, 4247.

(13) Slowing, I. I.; Vivero-Escoto, J. L.; Wu, C.-W.; Lin, V. S. Y. *Advanced Drug Delivery Reviews* **2008**, *60*, 1278.

(14) Trewyn, B. G.; Slowing, II; Giri, S.; Chen, H. T.; Lin, V. S. Y. *Accounts Chem. Res.* **2007**, *40*, 846.

(15) Slowing, I. I.; Trewyn, B. G.; Lin, V. S. Y. *Journal of the American Chemical Society* **2007**, *129*, 8845.

(16) Chung, T.-H.; Wu, S.-H.; Yao, M.; Lu, C.-W.; Lin, Y.-S.; Hung, Y.; Mou, C.-Y.; Chen, Y.-C.; Huang, D.-M. *Biomaterials* **2007**, *28*, 2959.

(17) Giri, S.; Trewyn, B. G.; Stellmaker, M. P.; Lin, V. S. Y. *Angewandte Chemie, International Edition* **2005**, *44*, 5038.

(18) Vivero-Escoto, J. L.; Slowing, I. I.; Wu, C.-W.; Lin, V. S. Y. *Journal of the American Chemical Society* **2009**, *131*, 3462.

(19) Zhao, Y.; Trewyn, B. G.; Slowing, I. I.; Lin, V. S. Y. *Journal of the American Chemical Society* **2009**, *131*, 8398.

(20) Zhu, C.-L.; Song, X.-Y.; Zhou, W.-H.; Yang, H.-H.; Wen, Y.-H.; Wang, X.-R. *Journal of Materials Chemistry* **2009**, *19*, 7765.

(21) Trewyn, B. G.; Nieweg, J. A.; Zhao, Y.; Lin, V. S. Y. *Chemical Engineering Journal (Amsterdam, Netherlands)* **2008**, *137*, 23.

(22) Lu, C.-W.; Hung, Y.; Hsiao, J.-K.; Yao, M.; Chung, T.-H.; Lin, Y.-S.; Wu, S.-H.; Hsu, S.-C.; Liu, H.-M.; Mou, C.-Y.; Yang, C.-S.; Huang, D.-M.; Chen, Y.-C. *Nano Letters* **2007**, *7*, 149.

(23) Lu, F.; Wu, S.-H.; Hung, Y.; Mou, C.-Y. *Small* **2009**, *5*, 1408.

(24) Sun, W.; Fang, N.; Trewyn, B. G.; Tsunoda, M.; Slowing, I. I.; Lin, V. S. Y.; Yeung, E. S. *Analytical and Bioanalytical Chemistry* **2008**, *391*, 2119.

(25) Huang, D.-M.; Hung, Y.; Ko, B.-S.; Hsu, S.-C.; Chen, W.-H.; Chien, C.-L.; Tsai, C.-P.; Kuo, C.-T.; Kang, J.-C.; Yang, C.-S.; Mou, C.-Y.; Chen, Y.-C. *FASEB Journal* **2005**, *19*, 2014.

(26) Rosenholm, J. M.; Meinander, A.; Peuhu, E.; Niemi, R.; Eriksson, J. E.; Sahlgren, C.; Linden, M. *ACS Nano* **2009**, *3*, 197.

(27) Huang, X.; Teng, X.; Chen, D.; Tang, F.; He, J. *Biomaterials*, *31*, 438.

(28) Hsiao, J.-K.; Tsai, C.-P.; Chung, T.-H.; Hung, Y.; Yao, M.; Liu, H.-M.; Mou, C.-Y.; Yang, C.-S.; Chen, Y.-C.; Huang, D.-M. *Small* **2008**, *4*, 1445.

(29) Huang, D.-M.; Chung, T.-H.; Hung, Y.; Lu, F.; Wu, S.-H.; Mou, C.-Y.; Yao, M.; Chen, Y.-C. *Toxicology and Applied Pharmacology* **2008**, *231*, 208.

(30) Tao, Z.; Morrow, M. P.; Asefa, T.; Sharma, K. K.; Duncan, C.; Anan, A.; Penefsky, H. S.; Goodisman, J.; Souid, A.-K. *Nano Letters* **2008**, *8*, 1517.

(31) Hudson, S. P.; Padera, R. F.; Langer, R.; Kohane, D. S. *Biomaterials* **2008**, *29*, 4045.

(32) Blumen, S. R.; Cheng, K.; Ramos-Nino, M. E.; Taatjes, D. J.; Weiss, D. J.; Landry, C. C.; Mossman, B. T. *Am. J. Respir. Cell Mol. Biol.* **2007**, *36*, 333.

(33) Vallet-Regi, M.; Ramila, A.; del Real, R. P.; Perez-Pariente, J. *Chemistry of Materials* **2001**, *13*, 308.

(34) Mal, N. K.; Fujiwara, M.; Tanaka, Y. *Nature (London, United Kingdom)* **2003**, *421*, 350.

(35) Lai, C.-Y.; Trewyn, B. G.; Jeftinija, D. M.; Jeftinija, K.; Xu, S.; Jeftinija, S.; Lin, V. S. Y. *Journal of the American Chemical Society* **2003**, *125*, 4451.

(36) Torney, F.; Trewyn, B. G.; Lin, V. S. Y.; Wang, K. *Nature Nanotechnology* **2007**, *2*, 295.

(37) Hernandez, R.; Tseng, H.-R.; Wong, J. W.; Stoddart, J. F.; Zink, J. I. *Journal of the American Chemical Society* **2004**, *126*, 3370.

(38) Nguyen, T. D.; Tseng, H.-R.; Celestre, P. C.; Flood, A. H.; Liu, Y.; Stoddart, J. F.; Zink, J. I. *Proceedings of the National Academy of Sciences of the United States of America* **2005**, *102*, 10029.

(39) Nguyen, T. D.; Leung, K. C. F.; Liong, M.; Pentecost, C. D.; Stoddart, J. F.; Zink, J. I. *Organic Letters* **2006**, *8*, 3363.

(40) Angelos, S.; Yang, Y.-W.; Patel, K.; Stoddart, J. F.; Zink, J. I. *Angewandte Chemie, International Edition* **2008**, *47*, 2222.

(41) Patel, K.; Angelos, S.; Dichtel, W. R.; Coskun, A.; Yang, Y.-W.; Zink, J. I.; Stoddart, J. F. *Journal of the American Chemical Society* **2008**, *130*, 2382.

(42) Coti, K. K.; Belowich, M. E.; Liong, M.; Ambrogio, M. W.; Lau, Y. A.; Khatib, H. A.; Zink, J. I.; Khashab, N. M.; Stoddart, J. F. *Nanoscale* **2009**, *1*, 16.

(43) Liong, M.; Angelos, S.; Choi, E.; Patel, K.; Stoddart, J. F.; Zink, J. I. *Journal of Materials Chemistry* **2009**, *19*, 6251.

(44) Angelos, S.; Liong, M.; Choi, E.; Zink, J. I. *Chemical Engineering Journal (Amsterdam, Netherlands)* **2008**, *137*, 4.

(45) Yang, Q.; Wang, S.; Fan, P.; Wang, L.; Di, Y.; Lin, K.; Xiao, F.-S. *Chemistry of Materials* **2005**, *17*, 5999.

(46) Park, C.; Oh, K.; Lee, S. C.; Kim, C. *Angewandte Chemie, International Edition* **2007**, *46*, 1455.

(47) Angelos, S.; Khashab, N. M.; Yang, Y.-W.; Trabolsi, A.; Khatib, H. A.; Stoddart, J. F.; Zink, J. I. *Journal of the American Chemical Society* **2009**, *131*, 12912.

(48) Khashab, N. M.; Belowich, M. E.; Trabolsi, A.; Friedman, D. C.; Valente, C.; Lau, Y.; Khatib, H. A.; Zink, J. I.; Stoddart, J. F. *Chemical Communications (Cambridge, United Kingdom)* **2009**, 5371.

(49) Aznar, E.; Coll, C.; Marcos, M. D.; Martinez-Manez, R.; Sancenon, F.; Soto, J.; Amoros, P.; Cano, J.; Ruiz, E. *Chemistry--A European Journal* **2009**, *15*, 6877.

(50) Fu, Q.; Rao, G. V. R.; Ista, L. K.; Wu, Y.; Andrzejewski, B. P.; Sklar, L. A.; Ward, T. L.; Lopez, G. P. *Advanced Materials (Weinheim, Germany)* **2003**, *15*, 1262.

(51) Fu, Q.; Rao, G. V. R.; Ward, T. L.; Lu, Y.; Lopez, G. P. *Langmuir* **2007**, *23*, 170-174.

(52) Gruenhagen, J. A.; Lai, C.-Y.; Radu, D. R.; Lin, V. S. Y.; Yeung, E. S. *Applied Spectroscopy* **2005**, *59*, 424.

(53) Liu, R.; Zhao, X.; Wu, T.; Feng, P. *Journal of the American Chemical Society* **2008**, *130*, 14418.

(54) Bernardos, A.; Aznar, E.; Marcos, M. D.; Martinez-Manez, R.; Sancenon, F.; Soto, J.; Barat, J. M.; Amoros, P. *Angewandte Chemie, International Edition* **2009**, *48*, 5884.

(55) Schlossbauer, A.; Kecht, J.; Bein, T. *Angewandte Chemie, International Edition* **2009**, *48*, 3092.

(56) Climent, E.; Bernardos, A.; Martinez-Manez, R.; Maquieira, A.; Marcos, M. D.; Pastor-Navarro, N.; Puchades, R.; Sancenon, F.; Soto, J.; Amoros, P. *Journal of the American Chemical Society* **2009**, *131*, 14075.

(57) Park, C.; Lee, K.; Kim, C. *Angewandte Chemie, International Edition* **2009**, *48*, 1275.

(58) Ferris, D. P.; Zhao, Y.-L.; Khashab, N. M.; Khatib, H. A.; Stoddart, J. F.; Zink, J. I. *Journal of the American Chemical Society* **2009**, *131*, 1686

(59) Kwon, E. J.; Lee, T. G. *Applied Surface Science* **2008**, *254*, 4732.

(60) Khashab, N. M.; Trabolsi, A.; Lau, Y. A.; Ambrogio, M. W.; Friedman, D. C.; Khatib, H. A.; Zink, J. I.; Stoddart, J. F. *European Journal of Organic Chemistry* **2009**, 1669.

(61) Aznar, E.; Casasus, R.; Garcia-Acosta, B.; Marcos, M. D.; Martinez-Manez, R.; Sancenon, F.; Soto, J.; Amoros, P. *Advanced Materials (Weinheim, Germany)* **2007**, *19*, 2228.

(62) Aznar, E.; Marcos, M. D.; Martinez-Manez, R.; Sancenon, F.; Soto, J.; Amoros, P.; Guillem, C. *Journal of the American Chemical Society* **2009**, *131*, 6833.

(63) Angelos, S.; Yang, Y.-W.; Khashab, N. M.; Stoddart, J. F.; Zink, J. I. *Journal of the American Chemical Society* **2009**, *131*, 11344.

(64) Liu, R.; Zhang, Y.; Feng, P. *Journal of the American Chemical Society* **2009**, *131*, 15128.

(65) Park, C.; Kim, H.; Kim, S.; Kim, C. *Journal of the American Chemical Society* **2009**, *131*, 16614.

(66) Gerweck, L. E.; Seetharaman, K. *Cancer Research* **1996**, *56*, 1194.

(67) Chung, P.-W.; Kumar, R.; Pruski, M.; Lin, V. S. Y. *Advanced Functional Materials* **2008**, *18*, 1390.

(68) Yang, Y.; Yan, X.; Cui, Y.; He, Q.; Li, D.; Wang, A.; Fei, J.; Li, J. *Journal of Materials Chemistry* **2008**, *18*, 5731.

(69) You, Y.-Z.; Kalebaila, K. K.; Brock, S. L.; Oupicky, D. *Chemistry of Materials* **2008**, *20*, 3354.

(70) Saito, G.; Swanson, J. A.; Lee, K.-D. *Advanced Drug Delivery Reviews* **2003**, *55*, 199.

CHAPTER 3. MESOPOROUS SILICA NANOPARTICLE-BASED DOUBLE DRUG DELIVERY SYSTEM FOR GLUCOSE-RESPONSIVE CONTROLLED RELEASE OF INSULIN AND CYCLIC AMP

A paper published in ***Journal of American Chemical Society***, **2009**, *131*, 8398-8400.

Yannan Zhao, Brian G. Trewyn, Igor I. Slowing, and Victor S.-Y. Lin

Abstract

A boronic acid-functionalized mesoporous silica nanoparticle-based drug delivery system (BA-MSN) was synthesized for glucose-responsive controlled release of both insulin and cyclic adenosine monophosphate (cAMP). Fluorescein isothiocyanate-labeled, gluconic acid-modified insulin (FITC-G-Ins) proteins are immobilized on the exterior surface of BA-MSN and also serve as caps to encapsulate cAMP molecules inside the mesopores of BA-MSN. The release of both G-Ins and cAMP was triggered by the introduction of saccharides. The selectivity of FITC-G-Ins release towards a series of carbohydrate triggers was determined to be fructose > glucose > other saccharides. The unique feature of this double release system is that the decrease of FITC-G-Ins release with cycles could be compensated for by the release of cyclic AMP (cAMP) from mesopores of MSN that is regulated by the gatekeeper effect of FITC-G-Ins. *In vitro* controlled release of cAMP was studied at two pH conditions (pH 7.4 and 8.5). Furthermore, the cytotoxicity of cAMP-loaded G-Ins-MSN with four different cell lines was investigated by cell viability and proliferation studies. The cellular uptake properties of cAMP-loaded FITC-BA-MSN with and without G-Ins capping

were investigated by flow cytometry and fluorescence confocal microscopy. We envision that this glucose-responsive MSN-based double release system could lead to a new generation of self-regulated insulin releasing devices.

ARTICLE

Stimuli-responsive controlled release systems have attracted much attention for their potential applications in the area of drug and gene delivery.[1-3] In particular, surface-functionalized, end-capped mesoporous silica nanoparticle (MSN) materials have been demonstrated as efficient stimuli-responsive controlled-release systems having the advantageous "zero premature release" property. The biocompatibility of MSN both *in vitro* and *in vivo* has been demonstrated by several recent studies.[4-7] Furthermore, the literature reports on the biodistribution and circulation properties of MSN administrated in animals by intravenous injection have highlighted the promising potential of these multifunctional nanoparticles for *in vivo* biomedical application and organ-specific delivery of therapeutics.

In contrast to nonporous nanoparticles, MSN offers both interior pore and exterior particle surfaces for loading different guest molecules. This is particularly useful for controlling the sequence of release for different cargos, which is crucial for the efficacy of many codelivery applications. These codelivery systems with control over the sequence of release could play a key role in overcoming several current challenges in therapy. For example, conventional glucose-responsive insulin delivery systems suffer from the decrease of insulin release with repeated cycles.[8,9] This problem could be overcome if the secretion of insulin from live cells could also be induced by sequential delivery of cyclic adenosine monophosphate (cAMP), which activates Ca^{2+} channels of pancreas beta cells and hence

stimulate insulin secretion.[10,11] However, due to the poor membrane permeability of cAMP, many attempts have been made to develop cAMP analogues[12] with good membrane permeability to study the insulin secretion mechanism. Unfortunately, to the best of our knowledge, no report of intracellular cAMP delivery by any drug carriers to control insulin production has appeared in the literature.

Herein, we report on the synthesis of a glucose-responsive MSN-based double delivery system for both insulin and cAMP with precise control over the sequence of release. As depicted in Figure 1a, gluconic acid-modified insulin (G-Ins)[8] proteins are immobilized on the exterior surface of MSN and also serve as caps to encapsulate cAMP molecules inside the mesopores of MSN. The release of both G-Ins and cAMP from MSN can be triggered by the introduction of saccharides, such as glucose. Also, we have demonstrated that the uncapped MSN could be efficiently endocytosed by live mammalian cells, leading to effective intracellular release of the cell-membrane-impermeable cAMP.

We first synthesized an aminopropyl-functionalized (1.6 mmol g^{-1}) mesoporous silica nanosphere material (AP-MSN) with an average particle diameter of 120 nm and MCM-41-type channel-like mesoporous structure (BJH pore diameter = 2.3 nm) *via* a method that we previously reported.[13] The particle size is small enough (≤ 200 nm) to evade rapid sequestration by phagocytotic cells of the spleen and to allow long blood circulation.[14] As described in the Supporting Information (SI), 4-carboxyphenylboronic acid (0.15 g), N-hydroxysuccinimide (0.10 g) and 1-ethyl-3-(3-dimethyl-aminopropyl)carbodiimide hydro-chloride (0.2 g) were introduced to AP-MSN (400 mg) in DMSO (20 mL) to yield the boronic acid-functionalized (0.5 mmol g^{-1}) BA-MSN material (Figure 1b). The presence of both aminopropyl and phenylboronic acid groups stabilizes the formation of borates with 1,2

or 1,3 diols (Figure 1a). A fluorescein isothiocyanate (FITC)-labeled G-insulin (FITC-G-Insulin) was prepared according to a literature procedure.[8] The bioactivity of G-Ins was demonstrated to be similar to that of unmodified insulin.[8] The mesopores of BA-MSN (100 mg) were loaded with cAMP (1 mM) in PBS buffer (10 mL, pH 7.4) and then capped with the FITC-G-Ins (200 mg) through reversible covalent bonding between phenylboronic acid and the vicinal diols of FITC-G-Ins, giving rise to the desired FITC-G-Ins-MSN material (Figure 1c). The loadings of cAMP and FITC-G-Ins were determined to be 27 and 64 μmol g^{-1} by HPLC[15] and fluorescence emission spectroscopy, respectively. As detailed in the SI, the structures and surface properties of BA-MSN and FITC-G-Ins-MSN were characterized by powder X-ray diffraction (XRD), N_2 surface analysis, ζ potential measurement, and transmission electron microscopy.

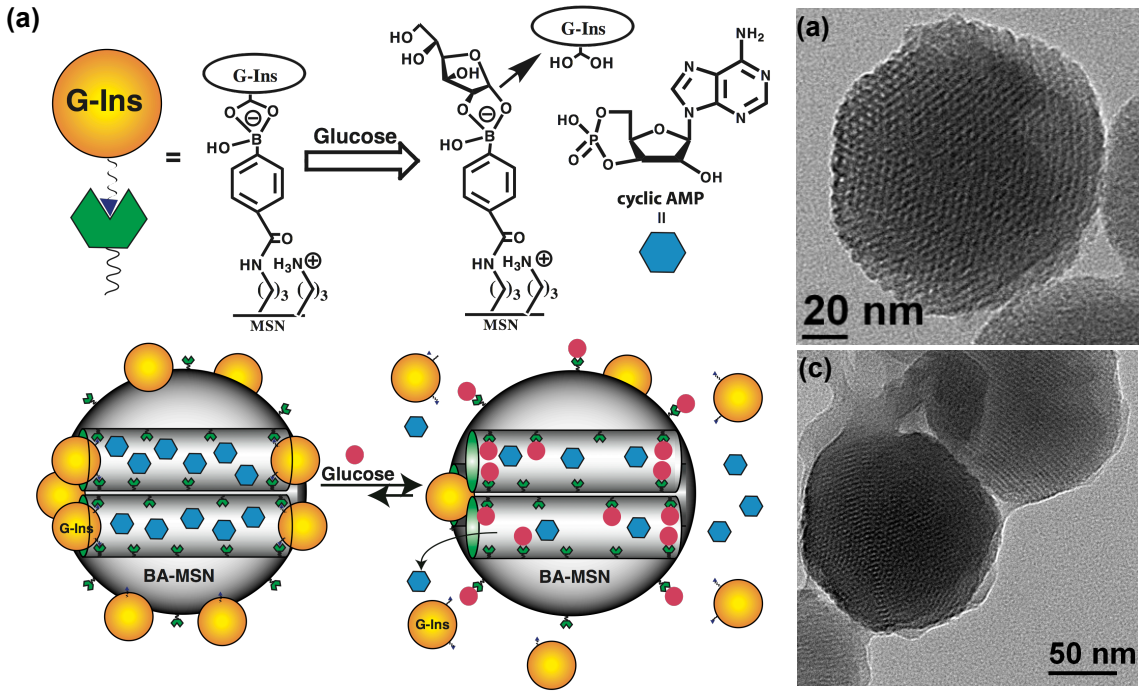

Figure 1. (a) Schematic representation of glucose-responsive MSN-based delivery system for the controlled release of bioactive G-Ins and cyclic AMP (cAMP). Transmission electron micrographs of (b) boronic acid-functionalized MSN and (c) FITC-G-Ins-capped MSN.

As demonstrated in literature,[16] phenylboronic acid forms much more stable cyclic esters with the adjacent diols of saccharides than with acyclic diols. This means that the linkage between FITC-G-Ins and BA-MSN could be cleaved by introducing various saccharides. Therefore, it was expected that the release of FITC-G-Ins would be sensitive to the chemical structures and concentrations of different carbohydrate triggers in forming stable cyclic boronic esters with BA-MSN. Among different saccharide triggers, the release of FITC-G-Ins indeed showed a strong preference for fructose, followed by glucose, as shown in Figure 2a. The observed high selectivity for fructose is consistent with other reported monoboronic acid-based sensors for saccharide recognition.[17] It is known that saccharides can interconvert between their pyranose and furanose isomeric forms, and phenylboronic acid has a strong preference for binding with the hydroxyls of saccharides in their furanose form. The high selectivity towards fructose could be explained by its high percentage of furanose form in water (25% for fructose vs. 0.14% for glucose).[18]

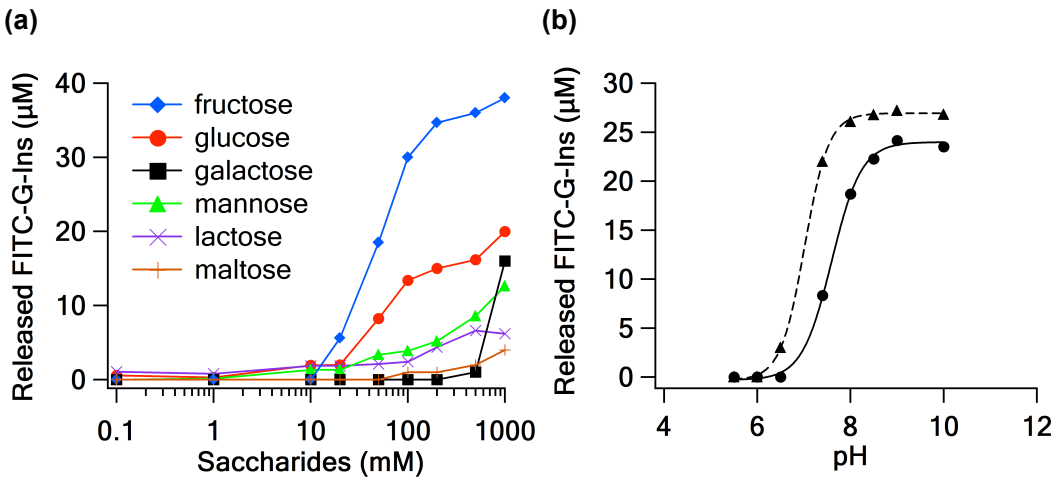

Figure 2. (a) Dependence of FITC-G-Ins release from FITC-G-Ins-MSN (2 mg mL^{-1} in PBS, pH 7.4) on the concentration of saccharide triggers. (b) The pH titration of insulin release from FITC-G-Ins-MSN (2 mg mL^{-1} in PBS) triggered by 50 mM glucose (solid line) and 50 mM fructose (dashed line).

For monoboronic acids in water with 1:1 saccharide/boronic acid complexation, high selectivity for fructose and low selectivity for glucose were observed, and the difference was attributed to the relative percentage of the furanose forms of these carbohydrates.[18] Interestingly, our system was highly responsive toward fructose and glucose in comparison with other saccharides (Figure 2a). This could be attributed to the heterogeneous spacing of boronic acid groups, which leads to the coexistence of 1:1 and 1:2 complexation, where the 1:2 complexation is widely used in the design of diboronic acid systems for selective glucose sensing.[19] In contrast, disaccharides (lactose and maltose) were not able to adopt a furanose form and hence could not serve as effective triggers for pore uncapping. While a stronger preference for fructose than for glucose was observed, the FITC-G-Ins-MSN system is still suitable for glucose-responsive insulin release due to the much lower level of blood fructose ($\leq$ 0.1 mM) than that of glucose ($\geq$ 10 mM) in diabetic patients.

The release of FITC-G-Ins triggered by all saccharides was found to be complete within 30 min, which is within the time frame of normal insulin secretion. The complexation of fructose and glucose with phenylboronic acid and the corresponding release of FITC-G-Ins exhibited a high pH dependency. As shown in Figure 2b, the release of FITC-G-Ins triggered by 50 mM fructose reached 85% of maximum release at pH 7.4. In contrast, significant release of FITC-G-Ins was only observed at pH values above 8 in the case of glucose. This is likely due to the fact that the formation of tetrahedral borate intermediate requires a pH higher than the pKa of boronic acid. The observed pH dependency in our material, which is indicative of the controlled release mechanism, is consistent with those of other literature-reported insulin delivery systems.[20]

To further examine the applicability of this system, FITC-G-Ins released by a

stepwise treatment of glucose at two diabetic levels (50 and 100 mM) was monitored (Figure S6 in the SI). A typical decrease in insulin release after the second cycle was observed. However, this problem of decreasing insulin level could be overcome by delivering the cell-membrane-impermeable cAMP into the cytosol to stimulate insulin secretion from pancreas beta cells. This double-release system sets up a new model for self-regulated insulin-releasing devices.

The glucose-triggered release of cAMP by FITC-G-Ins uncapping was determined by HPLC[15] at pH 7.4 and 8.5, as shown in Figure 3. In PBS (pH 7.4), the cAMP-loaded FITC-G-Ins-MSN exhibited less than 10 % leaching in the absence of glucose trigger, suggesting a good capping efficiency of FITC-G-Ins. The rate of cAMP release triggered by 50 mM glucose at pH 7.4 and 8.5 showed similar diffusion-controlled kinetic profiles. Specifically, ~ 80% of total release was obtained within 20 h. Furthermore, 55 and 67% of the total loaded cAMP (27 μmol g^{-1}) were released after 30 h at pH 7.4 and 8.5, respectively (Figure 3a). As shown in Figure 3b, the release of cAMP strongly depends on the concentration of glucose. A significant cAMP release at pH 7.4 was observed when the concentration of glucose trigger was above 100 mM, whereas 50 mM glucose triggered almost 60% of maximum release at pH 8.5. This pH dependency of cAMP release is consistent with that of FITC-G-Ins release from MSN.

To correlate these *in vitro* results with the physiological concentrations for potential *in vivo* applications, the therapeutic dosage of this material was estimated. Between meals, insulin level typically rises from a fasting level of 20-30 pM to a 30 min-maximum of 250-300 pM depending upon the amount and quality of carbohydrates consumed, while the diabetic insulin level remains at 20-30 pM or below. It has been reported in literature that at

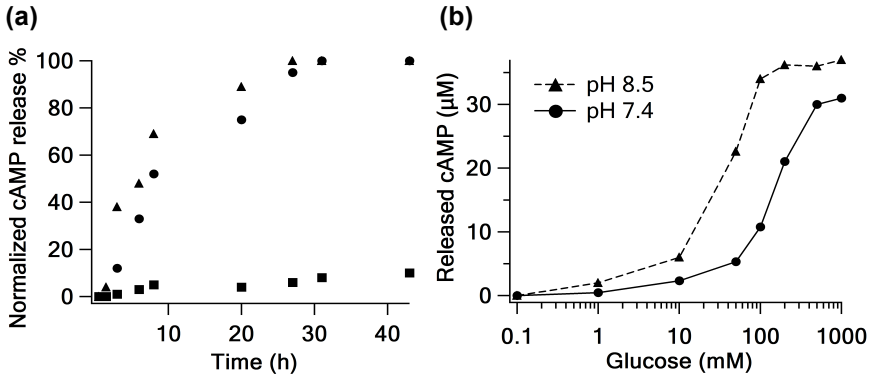

Figure 3. Controlled release of cAMP from FITC-G-Ins-MSN (2 mg mL^{-1} in PBS) (**a**) triggered by 50 mM glucose at pH 7.4 (●) and pH 8.5 (▲), with control data at pH 7.4 in absence of glucose (■), and (**b**) triggered by different concentrations of glucose at pH 7.4 (solid line) and 8.5 (dashed line) measured 48 h after glucose treatment.

least 250-300 pM of insulin is needed to decrease the diabetic blood glucose concentration to the normal level.[21] Our results indicate that 20 mM glucose indeed induced the release of 2 μM G-Ins from 2 mg mL^{-1} of our material (Figure 2a). Delivery of 250-300 pM of G-Ins would require only 0.25-0.3 μg mL^{-1} MSN material, which is 4 orders of magnitude lower in concentration than what we have demonstrated above. As reported previously, the MSN dosage has minimal effect on viability and proliferation of mammalian cells at concentrations below 100 μg mL^{-1} after 6 days.[22] Also, the maximum concentration of cAMP released from 2 mg mL^{-1} of the G-Ins-MSN material was 30 μg mL^{-1} (Figure 3b). On the basis of these results, we envision that the application of 0.25-0.30 μg mL^{-1} G-Ins-MSN *in vivo* could sufficiently deliver both G-Ins and cAMP for blood glucose regulation and insulin secretion, respectively, and would not pose any acute toxic effect.

To examine the cytotoxicity of the cAMP-loaded G-Ins-MSN material, cell viability and proliferation profiles of four different cell lines [rat pancreatic islet tumor (RIN-5F), mouse liver, skin fibroblast, and human cervical cancer (HeLa) cells] were evaluated by

Guava ViaCount cytometry assay after 24 h inoculation with the material. Good cell viability (> 90%) and proliferation (> 80%) were observed for all cell lines containing 5 or 20 μg mL^{-1} G-Ins-MSN. These results further indicate that this MSN-based double delivery system is biocompatible.

The cellular uptake properties of the cAMP-loaded BA-MSN *with* and *without* G-Ins capping were investigated with RIN-5F cells. As detailed in the SI, BA-MSN was labeled with FITC (FITC-BA-MSN) for this study prior to cAMP loading and G-Ins capping. The endocytosis efficiency was quantified by flow cytometry after 1 h incubation with 10 μg mL^{-1} of the materials (Figure S8). Interestingly, the cAMP-loaded FITC-BA-MSN without G-Ins capping showed a 2-fold higher endocytosis efficiency than that of the G-Ins-capped material. The result could be attributed to the difference in their surface charge properties: the ζ potentials were -28.3 mV for the uncapped material and -44.5 mV for the G-Ins-capped version.[13] This difference between the endocytosis efficiencies of the capped and uncapped materials implies that the G-Ins-MSN could circulate in regulatory system before the glucose-induced G-Ins release, and the enhanced cellular uptake of cAMP-loaded BA-MSN after the pore uncapping would allow efficient intracellular cAMP delivery.

To quantify the degree of intracellular release of cAMP from our system, the cAMP-loaded BA-MSN was allowed to be internalized by RIN-5F cells. After 6 hour of incubation, the total cellular concentration of cAMP was measured using a Millipore cAMP HTS immunoassay (see SI). The result was compared with that of RIN-5F cells introduced to free solution cAMP. As shown in Figure 4a, the total cellular concentration of cAMP indeed increased proportional to the dosage of cAMP-loaded BA-MSN. In contrast, no significant elevation of the cellular concentration of cAMP was observed in the case of free solution

cAMP even at the high dosage of 20 μg mL^{-1}, which is consistent with the poor cell-membrane permeability of free solution cAMP.

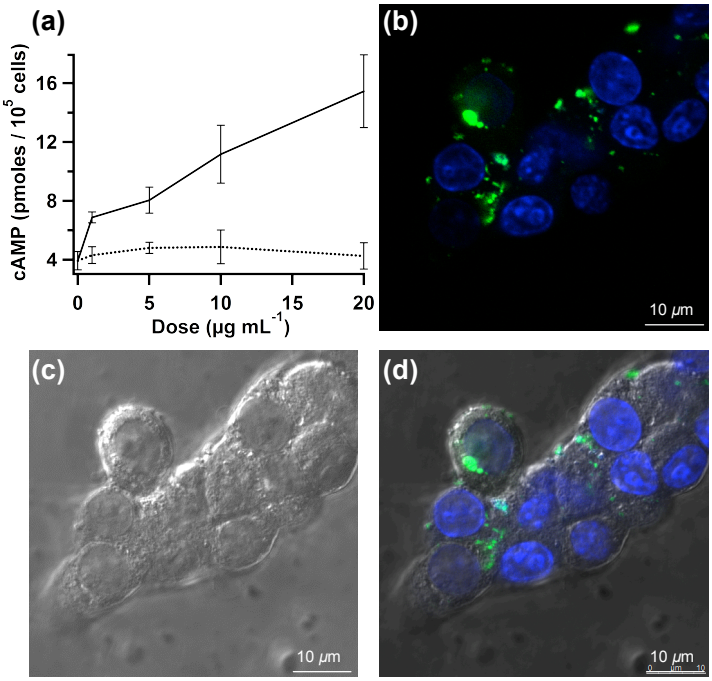

Figure 4. (a) Intracellular cAMP concentration of rat pancreatic RIN-5F cells treated with the cAMP-loaded BA-MSN (solid line) and with free-solution cAMP (dashed line), measured after 6 h of introduction. (b) Fluorescence confocal micrograph of RIN-5F cells incubated with 20 μg mL^{-1} of Fluo-cAMP-loaded BA-MSN (green) for 6 h. Cell nuclei were stained with DAPI (blue). (c) The corresponding differential interference contrast (DIC) micrographs. (d) Fluorescence confocal and DIC merged image. Enlarged individual and merged images are shown in Figure S9 in the SI.

To visualize intracellular delivery of cAMP, a membrane impermeable, fluorescence-labeled cAMP (8-Fluo-cAMP)[23] was loaded into the BA-MSN. Fluo-cAMP-loaded BA-MSN (20 μg mL^{-1}) was incubated with RIN-5F cells for 6 h. The fluorescence confocal micrographs (Figure 4b-d) clearly showed that Fluo-cAMP-loaded BA-MSN was indeed internalized by live RIN-5F cells. Green fluorescence was observed for both Fluo-cAMP-loaded BA-MSN particles and the free Fluo-cAMP molecules released from the MSN intracellularly.

In conclusion, we have successfully demonstrated that the phenylboronic acid-functionalized MSN can serve as an efficient codelivery system for saccharide-responsive controlled release of insulin and cAMP. The good biocompatibility, cellular uptake properties, and efficient intracellular release of cAMP set up the basis for future *in vivo* controlled-release biomedical applications.

ACKNOWLEDGMENT

This research is supported by the U.S. National Science Foundation NSF (CHE-0809521).

REFERENCES

(1) For review, see: Slowing, I. I.; Vivero-Escoto, J. L.; Wu, C.-W.; Lin, V. S. Y. *Adv. Drug Delivery Rev.* **2008**, *60*, 1278.

(2) For review, see: Descalzo, A. B.; Martinez-Manez, R.; Sancenon, F.; Hoffmann, K.; Rurack, K. *Angew. Chem., Int. Ed.* **2006**, *45*, 5924.

(3) For review, see: Angelos, S.; Liong, M.; Choi, E.; Zink, J. I. *Chem. Eng. J. (Amsterdam, Neth.)* **2008**, *137*, 4.

(4) Lee, C.-H.; Cheng, S.-H.; Wang, Y.-J.; Chen, Y.-C.; Chen, N.-T.; Souris, J.; Chen, C.-T.; Mou, C.-Y.; Yang, C.-S.; Lo, L.-W. *Adv. Funct. Mater.* **2009**, *19*, 215.

(5) Slowing, I. I.; Wu, C.-W.; Vivero-Escoto, J. L.; Lin, V. S. Y. *Small* **2009**, *5*, 57.

(6) Taylor, K. M. L.; Kim, J. S.; Rieter, W. J.; An, H.; Lin, W.; Lin, W. *J. Am. Chem. Soc.* **2008**, *130*, 2154.

(7) Wu, S.-H.; Lin, Y.-S.; Hung, Y.; Chou, Y.-H.; Hsu, Y.-H.; Chang, C.; Mou, C.-Y.

ChemBioChem **2008**, *9*, 53.

(8) Shiino, D.; Kataoka, K.; Koyama, Y.; Yokoyama, M.; Okano, T.; Sakurai, Y. *J. Intell. Mater. Syst. Struct.* **1994**, *5*, 311.

(9) Shiino, D.; Murata, Y.; Kubo, A.; Kim, Y. J.; Kataoka, K.; Koyama, Y.; Kikuchi, A.; Yokoyama, M.; Sakurai, Y.; Okano, T. *J. Controlled Release* **1995**, *37*, 269.

(10) Charles, M. A.; Fanska, R.; Schmid, F. G.; Forsham, P. H.; Grodsky, G. M. *Science* **1973**, *179*, 569.

(11) Dyachok, O.; Idevall-Hagren, O.; Saagetorp, J.; Tian, G.; Wuttke, A.; Arrieumerlou, C.; Akusjaervi, G.; Gylfe, E.; Tengholm, A. *Cell Metab.* **2008**, *8*, 26.

(12) Schultz, C.; Vajanaphanich, M.; Genieser, H.-G.; Jastorff, B.; Barrett, K. E.; Tsien, R. Y. *Mol. Pharmacol.* **1994**, *46*, 702.

(13) Slowing, I.; Trewyn, B. G.; Lin, V. S. Y. *J. Am. Chem. Soc.* **2006**, *128*, 14792.

(14) Awasthi, V. D.; Garcia, D.; Goins, B. A.; Phillips, W. T. *Int. J. Pharm.* **2003**, *253*, 121.

(15) Hoewer, H.; Zoch, E. *Fresenius' Z. Anal. Chem.* **1987**, *327*, 555.

(16) Springsteen, G.; Wang, B. *Tetrahedron* **2002**, *58*, 5291.

(17) Phillips, M. D.; James, T. D. *J. Fluoresc.* **2004**, *14*, 549.

(18) Lorand, J. P.; Edwards, J. O. *J. Org. Chem.* **1959**, *24*, 769.

(19) Fang, H.; Kaur, G.; Wang, B. *J. Fluoresc.* **2004**, *14*, 481.

(20) Matsumoto, A.; Ikeda, S.; Harada, A.; Kataoka, K. *Biomacromolecules* **2003**, *4*, 1410.

(21) Suckale, J.; Solimena, M. *Front. Biosci.* **2008**, *13*, 7156.

(22) Radu, D. R.; Lai, C.-Y.; Jeftinija, K.; Rowe, E. W.; Jeftinija, S.; Lin, V. S. Y. *J. Am. Chem. Soc.* **2004**, *126*, 13216.

(23) Moll, D.; Prinz, A.; Brendel, C. M.; Berrera, M.; Guske, K.; Zaccolo, M.; Genieser, H.-

G.; Herberg, F. W. *BMC Biochem.* **2008**, *9:18*.

Appendix: Supporting Information

1. Experimental

1.1. Synthesis of AP-MSN

N-Cetyltrimethylammonium bromide (CTAB, 1.00 g, 2.74 mmol) was dissolved in 480 mL of nanopure water. Sodium hydroxide aqueous solution (2.00 M, 3.50 mL) was introduced to the CTAB solution and the temperature of the mixture was adjusted to 353 K. Tetraethoxysilane (TEOS, 5.00 mL, 22.4 mmol) was added dropwise to the surfactant solution under vigorous stirring. The mixture was allowed to react for 2 h to give rise to a white precipitate. This solid crude product was filtered, washed with nanopure water and methanol, and dried under high vacuum to yield the as-synthesized MSN. To remove the surfactant template (CTAB), 1.50 g of the as-synthesized MSN was refluxed for 6 h in a methanolic solution of 1.50 mL HCl (37.2%) in 150 mL methanol. The resulting material was filtered and extensively washed with nanopure water and methanol. The surfactant-free MSN material was placed under high vacuum with heating at 333 K to remove the remaining solvent from the mesopores. MSN (1.00 g) was refluxed for 20 h in 80.0 mL of anhydrous toluene with 1.00 mL (5.67 mmol) of 3-aminopropyltrimethoxysilane to yield the 3-aminopropyl-functionalized MSN (AP-MSN) material. The surface amine groups were quantified at 1.6 mmol/g by ninhydrin test.[1]

1.2. Synthesis of BA-MSN

The purified AP-MSN (400 mg) was dispersed in 20 mL dimethyl sulfoxide (DMSO). 0.15 g (0.90 mmol) 4-carboxyphenylboronic acid (CBA) was reacted with 0.10 g (0.87 mmol) N-hydroxysuccinimide (NHS) and 0.20 g (1.04 mmol) 1-ethyl-3-(3-dimethylaminopropyl)

carbodiimide hydrochloride (EDC) in 5.0 mL DMSO, stirring at room temperature for 15 min before adding to the AP-MSN suspension. The mixture was stirred at room temperature for another 24 h, followed by filtration and washing with DMSO, water and methanol. The remaining surface amine groups were quantified at 1.1 mmol/g by ninhydrin test,[1] and surface boronic acid groups were calculated to be around 0.5 mmol/g by subtracting the amount of remaining surface amine groups from that on AP-MSN surface.

1.3. Synthesis of FITC-G-Ins

Gluconic acid modified insulin (G-Ins) was prepared according to the reported procedure,[2] and was further labeled with FITC for *in vitro* controlled release study. G-Ins (200 mg) was dissolved in 50 mL sodium carbonate buffer (0.1 M, pH 9), and 2.5 mL FITC in DMSO (1 mg/mL) was added in 5 μL aliquots while gently stirring the G-ins solution in dark. The reaction was stirred for another 2 h at room temperature before adding NH_4Cl (2.5 mL, 1 M) to quench excess FITC. After stirring for another 1 h, the solution was dialyzed in phosphate-buffered saline (PBS) (Spectra/Por 3, MWCO = 3500, Spectrum) and freeze dried to yield FITC labeled G-Ins (FITC-G-Ins). The ratio of FITC to G-ins was estimated at 1.3 by measuring the absorbance at 495 nm and 280 nm.

1.4. Synthesis of cAMP loaded FITC-G-Ins-MSN

The purified BA-MSN (100.0 mg) was stirred in a solution of cAMP (1 mM) in PBS solution (10 mL, 154 mM, pH 7.4) for 24 h in dark. Then, FITC-G-Ins (200 mg) was added to the suspension. The mixture was stirred in dark for another 24 h, following by filtration and washing extensively with PBS to remove physisorbed, uncapped cAMP and uncoated FITC-G-Ins from the exterior surface of the material. The resulting precipitate was isolated and dried under high vacuum. The loading of cAMP (27 μmol/g) and FITC-G-Ins (64

μmol/g) was calculated by subtracting the amount of cAMP/FITC-G-insulin remaining in the phosphate buffer and combined washings from the amount of cAMP/insulin initially added to the reaction.

1.5. Saccharides triggered G-Ins and cAMP release study

Cyclic AMP loaded FITC-G-Ins-MSN (6.00 mg) was dispersed in 3.00 mL of PBS with different concentrations of saccharides triggers. Aliquots (1.5 mL) were taken after 2 days stirring in dark at room temperature, followed by centrifuge (14000 rpm, 20 min). The release of FITC-G-Ins was determined by fluorescence emission spectroscopy (exc. at 488 nm, em. at 515 nm). The release of cAMP was monitored by HPLC (Hitachi LC/3DQMS with a reverse phase C18 column (Vydac), 0.4 cm x 25 nm), according to the literature reported method.[3] For the release kinetics study, cAMP loaded FITC-G-Ins-MSN (30.00 mg) was dispersed in 15.00 mL of PBS with 50 mM glucose. Aliquots (1.2 mL) were taken periodically from the suspension, followed by centrifuge (14000 rpm, 20 min), and the release kinetics of FITC-G-Ins and cAMP were monitored by fluorescence emission spectroscopy and HPLC, respectively.

1.6. G-Ins release study by stepwise glucose treatment

Cyclic AMP loaded FITC-G-Ins-MSN (20.00 mg) was dispersed in 10.00 mL of PBS and treated with 50 mM/ 100 mM glucose every 50 min. The release of FITC-G-Ins was monitored after 10 and 30 min glucose treatment, immediately followed by washing with 10.00 mL fresh PBS without glucose. The concentration of FITC-G-Ins in the washing PBS was recorded as the data point 40 min after treatment. The treatment was repeated until the release of FITC-G-Ins was stable without any increase (Figure S6).

2. Characterization

2.1. Powder X-Ray Diffraction

X-ray diffraction patterns of the MSN materials were obtained in a Scintag XDS-2000 powder diffractometer using Cu Kα irradiation.

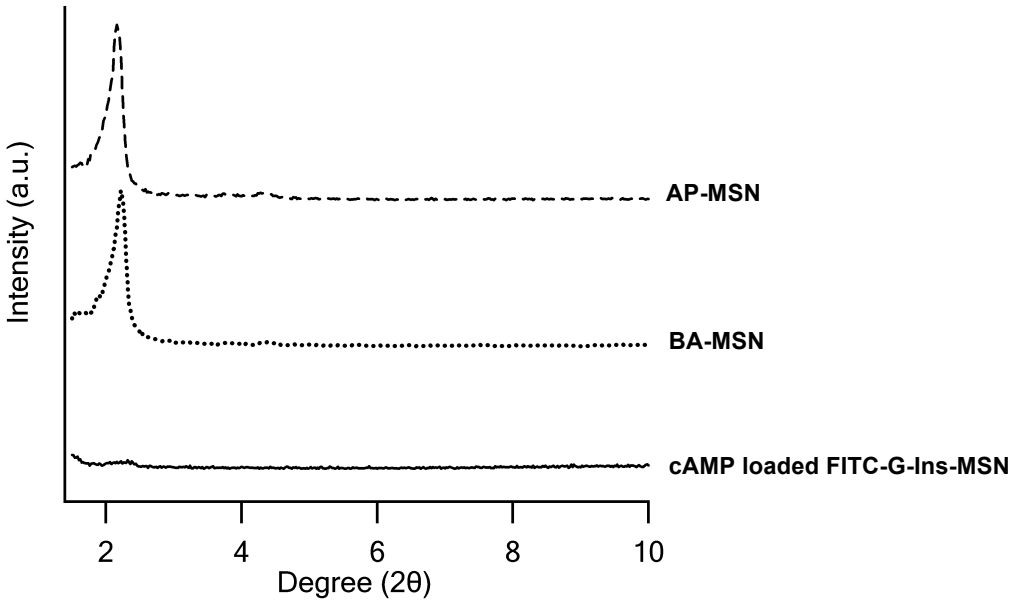

Figure S1. Powder X-Ray Diffraction patterns of AP-MSN, BA-MSN, and cAMP loaded FITC-G-Ins-MSN. Both AP-MSN and BA-MSN exhibit the typical diffraction patterns of MCM-41 type mesoporous silica with hexagonal symmetry. The changes in the cAMP loaded FITC-G-Ins-MSN diffraction pattern might be caused by pore filling and insulin coating effects.

Table S1. Powder X-Ray diffraction patterns

Material	d_{100} (Å)	a_0 (Å)	$d_{\text{pore wall}}$ (Å)
AP-MSN	40.9	47.2	6.3
BA-MSN	39.7	45.8	6.1

The d_{100} numbers represent the d-spacing corresponding to the main (100) XRD peak. The unit-cell size (a_0) is calculated from the d_{100} data using the formula $a_0 = 2\ d_{100}/3^{1/2}$. The pore wall thickness $d_{\text{pore wall}} = a_0 - W_{BJH}$.

2.2. Nitrogen adsorption/desorption isotherms

Surface analysis of the MSN materials was performed by nitrogen sorption isotherms in a Micromeritics Tristar 3000 sorptometer. The surface areas were calculated by the Brunauer–Emmett–Teller (BET).

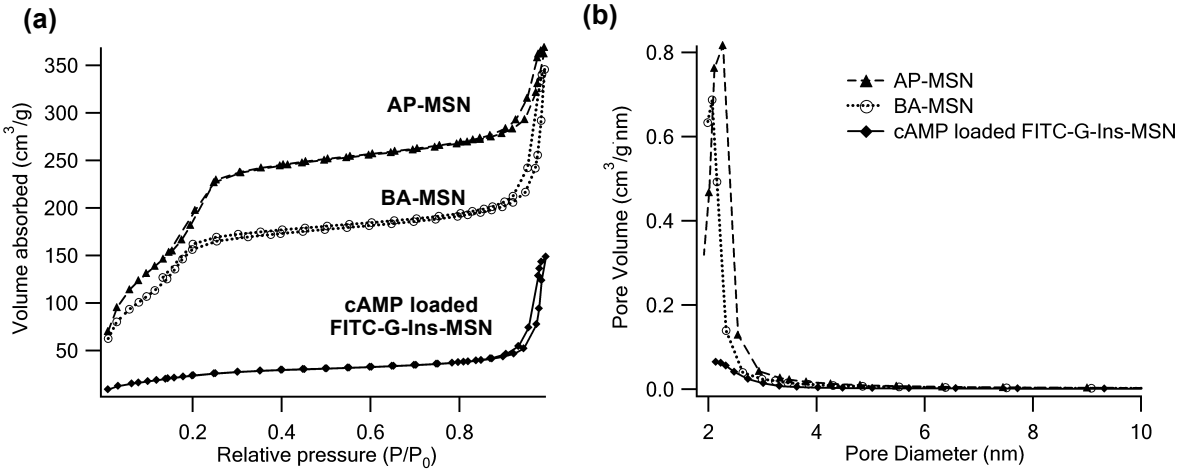

Figure S2. (a) BET nitrogen adsorption/desorption isotherms and (b) BJH pore size distributions of AP-MSN, BA-MSN and cAMP loaded FITC-G-Ins-MSN.

Table S2. BET and BJH parameters

Material	BET surface area S_{BET} (m^2/g)	BET Pore Volume V_P (cm^3/g)	BJH Pore diameter W_{BJH} (Å)
AP-MSN	708.2	0.652	23
BA-MSN	634.6	0.520	21
cAMP loaded FITC-G-Ins-MSN	93.8		

2.3. Transmission Electron Micrographs (TEM) of BA-MSN and FITC-G-Ins-MSN

The TEM examination was completed on a Tecnai G2 F20 electron microscope operated at 200 kV to examine at electron optical magnification of 64,000 to 550,000.

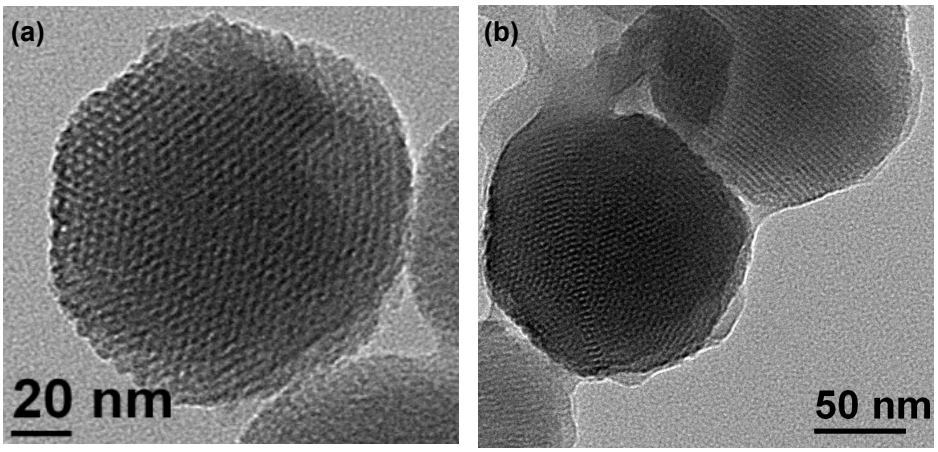

Figure S3. TEM micrographs of (a) BA-MSN and (b) FITC-G-Ins-MSN.

2.4. Surface charge

The ζ-potential the MSN materials was measured in a Malvern Nano HT Zetasizer. 200 μg/mL suspensions of each of the materials in PBS (20 mM, pH 7.4) were prepared for this measurement.

Table S3. ζ -potential results

Material	ζ -potential (mV)
AP-MSN	+ 5.86
BA-MSN	- 14.6
cAMP loaded FITC-G-Ins-MSN	- 44.8

2.5. Alizarin Red S. (ARS) assay for boronic acid groups of BA-MSN

The stability and binding ability of boronic acid groups on BA-MSN surface was examined using the fluorescent reporter Alizatin Red S. (ARS), according to published literature procedures.[4,5] The fluorescence intensities were measured with an excitation wavelength of 468 nm and an emission wavelength of 572 nm. A typical set of fluorescence spectra, which reflect the large changes in fluorescence intensity upon addition of BA-MSN to and ARS solution, is shown in Figure S4.

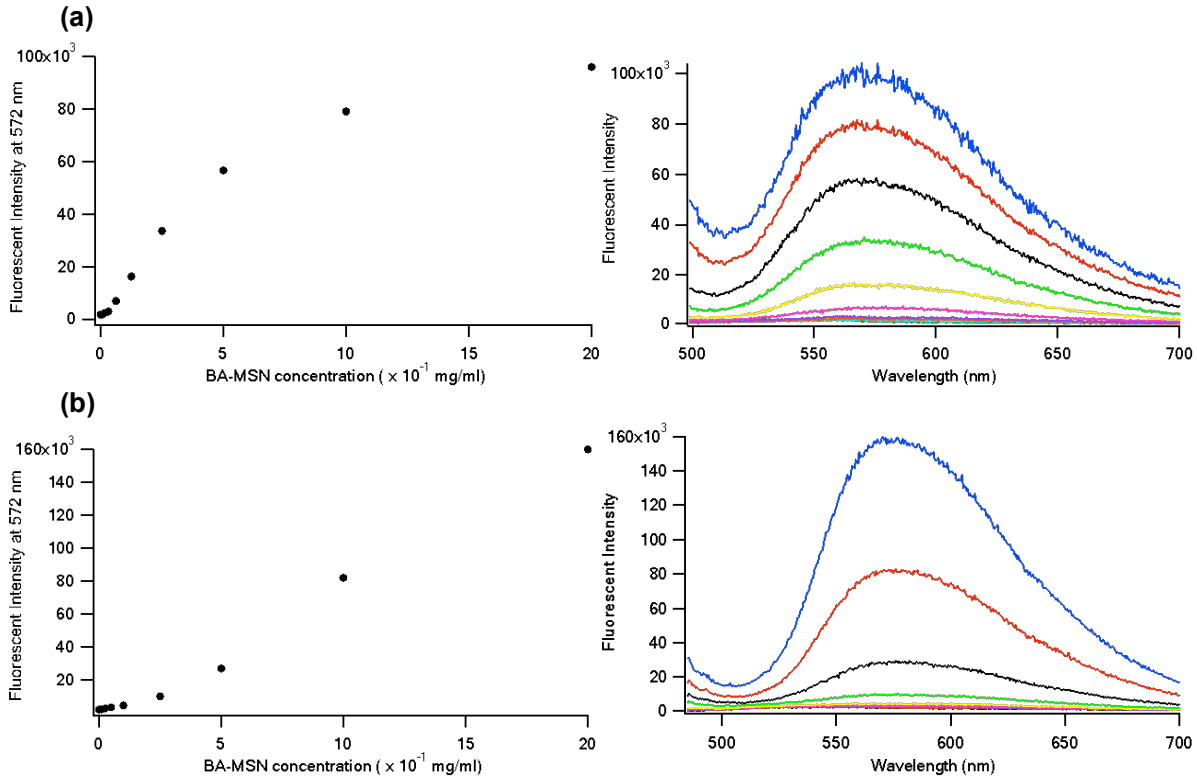

Figure S4. Fluorescent intensity increases (Exc. λ = 468 nm, Em. λ = 572 nm) with added BA-MSN (0 through 2.0 mg/mL) into a solution of ARS (a) 1.0×10^{-5} M (b) 1.0×10^{-4} M, in PBS (pH 7.4).

2.6. Competitive binding examination of BA-MSN with Alizarin Red S. and glucose

When glucose was added to the mixture of BA-MSN and ARS, fluorescence intensity decreases were observed. Titrating glucose into an aqueous solution of 1.0×10^{-4} M ARS and 0.4 mg/mL BA-MSN caused a signification drop in fluorescence intensity at glucose concentration over 50 mM, and a measurable change down to 10 mM.

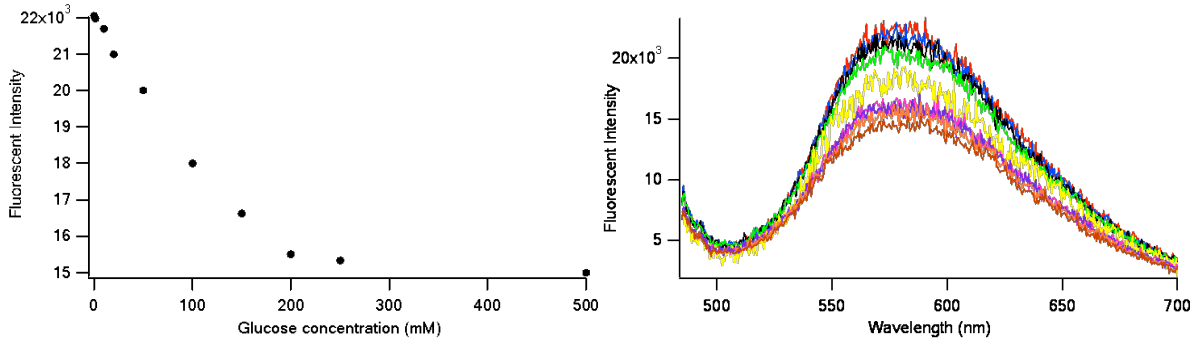

Figure S5. Titration of glucose into a solution of ARS (1.0×10^{-4} M) and BA-MSN (0.4 mg/mL). Fluorescence decreases (Exc. λ = 468 nm, Em. λ = 572 nm) with added glucose (0 through 0.5 M), in PBS (pH 7.4).

2.7. FITC-G-Ins release by stepwise glucose treatment

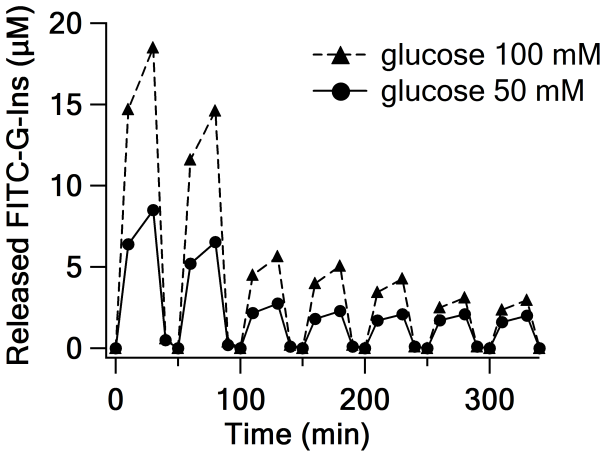

Figure S6. FITC-G-Ins release from FITC-G-Ins-MSN (2 mg mL-1 in PBS, pH 7.4) by stepwise treatment with 50 mM glucose (solid line) and 100 mM glucose (dashed line). Glucose was introduced every 50 min and removed by PBS washing 30 min post-treatment.

3. Biological studies

Reagents and materials for biological studies

Rat islet tumor (RIN-5F), mouse liver, skin fibroblast, HeLa cell line was obtained from American Tissue Culture Collection (ATCC). Formaldehyde solution (37%, w/w) was purchased from Fisher. 4,6-Diamidino-2-phenylindole dihydrochloride (DAPI) and trypan

blue solution (0.4%, w/w) were purchased from Sigma-Aldrich. Trypsin (1×, 0.25%) in 0.1% EDTA-Na without calcium and magnesium was purchased from Fisher Scientific. 8-(2-[Fluoresceinyl]aminoethylthio)-adenosine-3',5'-cyclic monophosphate (8-Fluo-cAMP) was purchased from Axxora, LLC. Cyclic AMP HTS Immunoassay kit was purchased from Millipore.

Cell line maintenance

Rat islet tumor (RIN-5F) cells were maintained in T75 flasks using ATCC formulated RPMI-1640 medium supplemented with 10% (v/v) fetal bovine serum, 100 U/mL penicillin, and 100 μg/mL streptomycin. The medium was renewed every 3-4 days. Subculture was performed every 6-8 days at a ratio of 1:3-1:5.

Mouse liver, skin fibroblast and HeLa cells were maintained in T75 flasks using the base medium DMEM (Dulbucco's modified Eagle's medium) supplemented with 2 mM l-glutamine, 100 U/mL penicillin, 100 μg/mL streptomycin, and 1 mg/mL gentamycin. To make the complete growth medium, 10% (v/v) fetal bovine serum is added for liver and skin fibroblast cells culture, and 10% (v/v) equine serum is added for HeLa cells. Subculture was performed every 3-5 days for liver and skin fibroblast cell lines, and every 2-3 days for HeLa cells at a ratio of 1:3-1:5.

3.1. Cell viability and proliferation study

To eliminate any interference caused by FITC, G-Ins was used instead of FITC-G-Ins for capping upon cAMP loading, and G-Ins capped BA-MSN (G-Ins-MSN) was used for cytotoxicity study described here.

Rat islet tumor (RIN-5F), liver, skin fibroblast and HeLa cells were seeded in 6-well plates at the concentration of 1×10^5 cells/mL and were incubated for 48 h in standard culture

medium at 37 °C in 5% CO_2. After 48 h, the cells were inoculated with 5.0 μg/mL and 20.0 μg/mL of cAMP loaded G-Ins-MSN, and grown for an additional 24 h. As a control experiment, the cells were incubated with standard growth medium without cAMP loaded G-Ins-MSN for another 24 h. Finally, the cytotoxicity of this material with different cell lines was evaluated by Guava ViaCount cytometry assay (Guava Technologies, Inc.; Hayward, CA). Cell viability was calculated as a percentage of viable cells 24 h post-treatment with cAMP loaded G-Ins-MSN compared with untreated cells. Cell proliferation was calculated as a percentage of the total number of cells after G-Ins-MSN treatment out of the total number of untreated cells. Figure S7 shows the results of the cell counts 24 post-treatment. The viability was found to be between 90 and 100%, and the proliferation to be between 80 and 100%.

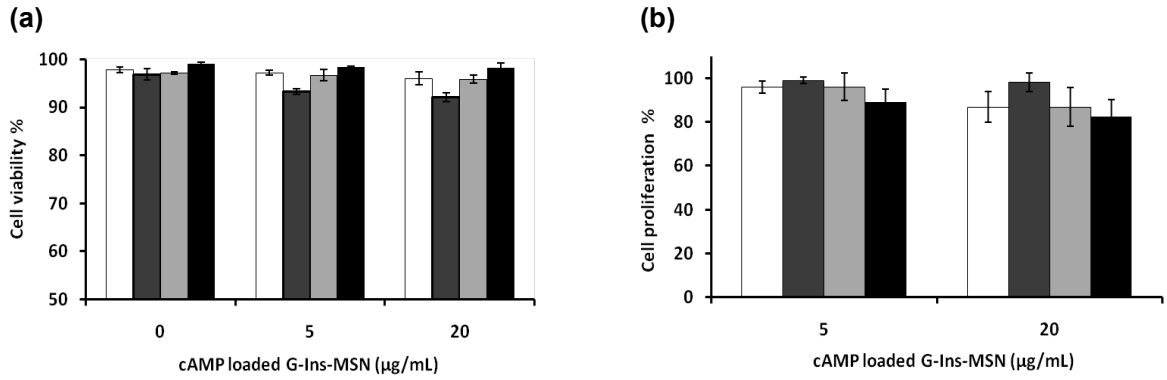

Figure S7. (a) Cell viability and (b) proliferation study of cAMP loaded G-Ins-MSN with rat pancreatic RIN-5F (white), mouse liver (dark grey), skin fibroblast (light grey) and HeLa (black) cells. The concentrations of the material used were 5 and 20 μg/mL.

3.2. Measuring the endocytosis efficiency with RIN-5F cells

BA-MSN was labeled for this endocytosis study by reacting 200 mg of BA-MSN with 7.8 mg (0.1 mmol) fluorescein isothiocyanate (FITC) in 20 mL methanol at room

temperature for 2 h. The resulting product was filtered and washed with methanol extensively to remove physisorbed FITC. cAMP loaded FITC-BA-MSN was then prepared by incubating 10 mg of FITC-BA-MSN with 1 mM cAMP in 2 mL PBS solution (154 mM, pH 7.4) at room temperature in dark for 24 h with stirring, and cAMP loaded G-Ins-FITC-MSN was prepared by further capping with 20 mg of G-Ins in 2 mL of 1 mM cAMP PBS solution for another 24 h incubation, following by filtration and washing with PBS. The zeta potential was determined to be -28.3 mV for the uncapped cAMP loaded FITC-BA-MSN material and -44.5 mV for the G-In-capped cAMP loaded G-Ins-FITC-MSN.

The RIN-5F cells at a concentration of 1×10^5 cells/mL were grown in 6-well plates for 72 h at 37 °C in 5% CO_2. The cells were then treated with 10μg/mL of cAMP loaded FITC-BA-MSN and cAMP loaded G-Ins-FITC-MSN suspended in serum-free media and were incubated for another 1 h at 37 °C in 5% CO_2. After 1 h, the cells were washed once with PBS and trypsinized. The cells were incubated in 830 mM trypan blue for 10 min to quench the fluorescence of any MSN nanoparticles adhered to the exterior of the cells. The cellular uptake was measured by flow cytometry.

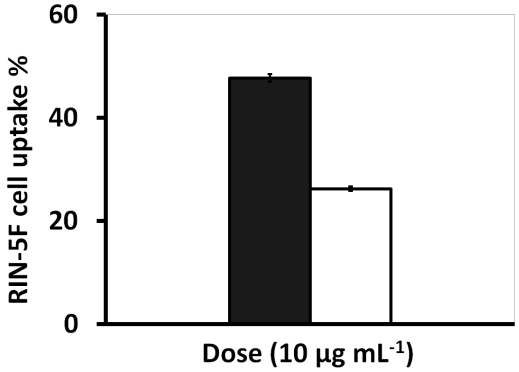

Figure S8. Rat pancreatic RIN-5F cellular uptake of 10 μg/mL of cAMP loaded FITC-BA-MSN (filled) and cAMP loaded G-Ins-FITC-MSN (open).

3.3. Fluorescence confocal microscopy measurements

To visually investigate the endocytosis and intracellular cAMP delivery by this material, fluorescence confocal microscopy measurement was employed. A membrane impermeable cAMP analogue 8-Fluo-cAMP was loaded to BA-MSN for the visualization of drug delivery, same procedure as described above for cAMP loading. Coverslips (22 mm^2) were cleaned with 1.0 M HCl, nanopure water (3×), 50% ethanol, 70% ethanol, and 100% ethanol, and dried overnight at 60 °C. Following cleaning, the coverslips were placed on the bottom of the wells of 6-well plates and covered with 3.0 mL of standard growth media. RIN-5F cells (1.0×10^5 cells/mL) were grown for 72 h on the coverslips. After 72 h, the cells were inoculated with 20.0 μg/mL of Fluo-cAMP loaded FITC-MSN, and grown for an additional 6 h. Afterwards, the growth media was removed, the cells were washed with PBS (2×), and the cells were then reincubated with a PBS solution of 3.7% formaldehyde and 57.0 mM 4,6-Diamidino-2-phenylindole dihydrochloride (DAPI) for 30 min. These coverslips were removed from the PBS solution and fixed to glass slides with liquid adhesive.

3.4. Quantification of intracellular cAMP delivery

The intracellular cAMP concentration was determined by a Millipore's cAMP High Throughput Screening (HTS) Immunoassay kit according to the manufacturer's directions. RIN-5F cells (1×10^5 cells/mL) were seeded in 48-well plates for 72 h at 37 °C in 5% CO_2. The cells were then treated with incremental amounts (0, 1, 5, 10, 20 μg/mL) of cAMP loaded BA-MSN suspended in serum-free media for 6 h at 37 °C in 5% CO_2. After 6 h, Adherent cells were washed five times with PBS to remove extracelluar MSN particles and lysed for the intracellular cAMP assay or trypsinized for cell count by Guava ViaCount cytometry assay. The cellular cAMP levels were reported as pmoles/10^5 cells.

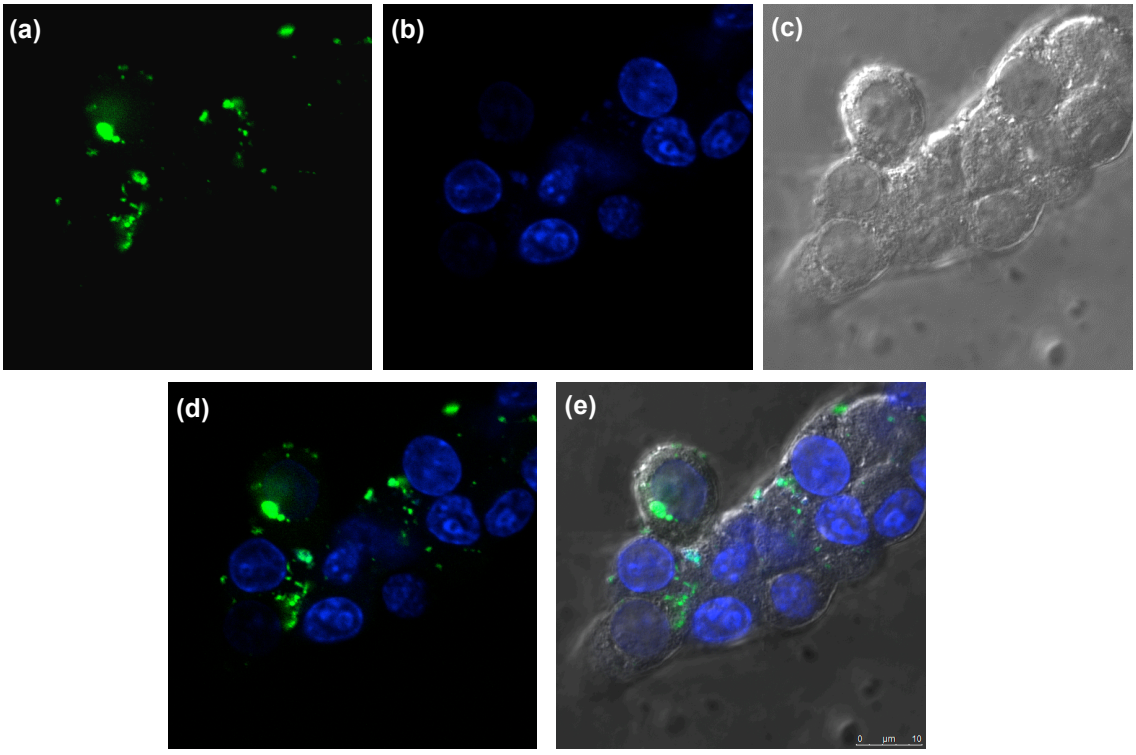

Figure S9. Fluorescence confocal micrographs of RIN-5F cells (a) internalized with 20 μg mL^{-1} suspension of Fluo-cAMP loaded BA-MSN (green) and (b) stained with 57.0 mM of DAPI (blue). The corresponding Differential Interference Contrast (DIC) micrograph is displayed in image (c). The image (a) and (b) merged micrograph and the image (a) (b) and (c) merged micrograph are shown in image (d) and (e), respectively.

References

(1) Leane, M. M.; Nankervis, R.; Smith, A.; Illum, L. *Int. J. Pharm.* **2004**, *271*, 241-249.

(2) Shino, D.; Kataoka, K.; Koyama, Y.; Yokoyama, M.; Okano, T.; Sakurai, Y. *J. Intell. Mater. Syst. Struct.* **1994**, *5*, 311-14.

(3) Hoewer, H.; Zoch, E. *Fresenius' Z. Anal. Chem.* **1987**, *327*, 555-7.

(4) Springsteen, G.; Wang, B. *Chem. Commun.* **2001**, 1608-1609.

(5) Springsteen, G.; Wang, B. *Tetrahedron* **2002**, *58*, 5291-5300.

CHAPTER 4. INTERACTION OF MESOPOROUS SILICA NANOPARTICLES WITH HUMAN RED BLOOD CELL MEMBRANES: SIZE AND SURFACE EFFECTS

A paper published in ***ACS Nano***, **2011**, *5*, 1366-1375

Yannan Zhao, Xiaoxing Sun, Guannan Zhang, Brian G. Trewyn, Igor I. Slowing, and Victor S.-Y. Lin

ABSTRACT

The interactions of mesoporous silica nanoparticles (MSNs) of different particle sizes and surface properties with human red blood cell (RBC) membranes were investigated by membrane filtration, flow cytometry and various microscopic techniques. Small MCM-41-type MSNs (~100 nm) were found to adsorb to the surface of RBCs without disturbing the membrane or morphology. In contrast, adsorption of large SBA-15-type MSNs (~600 nm) to RBCs induced a strong local membrane deformation leading to spiculation of RBCs, internalization of the particles, and eventual hemolysis. In addition, the relationship between the degree of MSN surface functionalization and the degree of its interaction with RBC, as well as the effect of RBC-MSN interaction on cellular deformability were investigated. The results presented here provide a better understanding of the mechanisms of RBC-MSN interaction and the hemolytic activity of MSNs, and will assist in the rational design of hemocompatible MSNs for intravenous drug delivery and *in vivo* imaging.

1. Introduction

Recent advancements in particle size and morphology control of mesoporous materials have led to the creation of nano- and submicron-sized mesoporous silica nanoparticles (MSNs).[1-5] The MSN materials with well-ordered cylindrical pore structures such as MCM-41 and SBA-15, have attracted special interest in the biomedical field.[1] The large surface areas and pore volumes of these materials allow the efficient adsorption of a wide range of molecules, including small drugs,[6-10] therapeutic proteins,[11-13] antibiotics,[14, 15] and antibodies.[16] Therefore, these materials have been proposed for use as potential vehicles for biomedical imaging, real-time diagnosis, and controlled delivery of multiple therapeutic agents.[6-8, 10, 17-25]

Despite the considerable interest in the biomedical applications of MSNs, relatively few studies have been published on the biocompatibility of the two most common types of MSNs (MCM-41 and SBA-15).[26-29] Asefa and co-workers reported that the cellular bioenergetics (cellular respiration and ATP levels) were inhibited remarkably by large SBA-15 nanoparticles, but the inhibition was greatly reduced by smaller MCM-41 type nanoparticles.[26] These differences in the disruption of cellular bioenergetics are believed to be caused by the different surface areas, number of surface silanol groups, and/or particle sizes of both types of material. A recent study by Kohane and collaborators on the systemic effects of MCM-41 (particle size ~ 150 nm) and SBA-15 (particle size ~ 800 nm) MSNs in live animals revealed interesting findings regarding their biocompatibility.[27] While large doses of mesoporous silicas administered subcutaneously to mice appear to be relatively harmless, the same doses given intravenously or intraperitoneally were lethal.[27] A possible

reason for the severe systemic toxicity of MSNs when injected intravenously could be the interactions of the nanoparticles with blood cells.

Our initial studies on the biocompatibility of MCM-41 type MSNs with red blood cells (RBCs), the dominant (99%) cell type in blood, suggested that this material was innocuous in comparison to the highly hemolytic amorphous silica.[30] These results were later confirmed by Lin and Haynes, who demonstrated that the hemocompatibility of MSNs also depended on the size of the nanoparticles.[31] These findings were mainly based on hemolysis assays performed by UV-Vis spectroscopy. The lack of hemolysis, however, does not necessarily warrant the absence of interactions between the particles and the RBCs, which could lead to more subtle side effects. Such side effects could eventually be the ones responsible for the enhanced systemic toxicity observed upon intravenous injection of these materials.[27] Therefore, an in depth study of other possible biological side effects of these materials must be performed if they are intended to be applied as vehicles for drug delivery.

In general, our knowledge of the biocompatibility, bioretention, and biodistribution of MSNs does not match with the rapid pace of research on their syntheses in numerous forms and structures. To date, efforts have focused predominantly on exploiting multifunctional nanoparticles as intravascular drug carriers with different particle sizes ranging from a few tens of nanometers[4,24,32] up to hundreds of nanometers,[3,5] various pore diameters ranging from 2 to 10 nm[5,11,33] and assorted surface functionalities from small organic groups (*e.g.*, amino,[34,35] carboxyl,[35] thiol,[35] phosphate,[19] *etc*) to large molecules (*e.g.*, dendrimers,[36] polyethyleneimine (PEI),[25,37] poly(ethylene glycol) (PEG),[38] phospholipids,39 *etc*). Unfortunately, these endeavors are limited by a poor understanding of particle interactions with cells in circulation.

Herein, we report our investigations on the interactions of the two most common types of MSNs (MCM-41 and SBA-15) with RBC membranes using fluorescence and electron microscopies and cell biology techniques. In addition to studying the effects of particle size and surface area on the hemolytic behavior of MSNs, we explored the effects that the chemical nature and degree of surface functionalization of the particles has on their interactions with RBCs. Understanding these effects will not only offer a guide for the rational design of biocompatible particles, but will also provide an insight into how to control the circulation properties of MSNs in the bloodstream. In fact, a prolonged circulation of polymeric nanoparticles has been recently demonstrated by means of their non-covalent attachment to the RBC membrane.[40] Attachment to the RBC membrane, however, may affect one of its most important properties, namely its deformability (*i.e.* the ability of an erythrocyte to deform so it can flow through microcirculation). To the best of our knowledge, this problem has not yet been addressed for any drug delivery system. In this work, we examined the effect of RBC-MSN interactions on membrane deformability by the Nucleopore filtration technique,[41] and established how size and surface properties can alter this important property. Overall, we propose three fundamental criteria to assess the hemocompatibility of nanoparticles: (1) hemolytic potential, (2) propensity to induce RBC membrane deformation or morphological alteration, and (3) tendency to impair RBC deformability. The evaluation of these conditions will enable a more adequate estimation of the hemocompatibility of many types of nanomaterials. This study suggests a minimal set of criteria that must be met before performing *in vivo* studies involving the intravascular administration of nanoparticles.

2. Results and Discussion

2.1. Size- and surface-dependent MSN interaction with RBC membranes

While particle size effect of MCM-41 type MSNs has already been established with larger particles producing lower hemolysis on RBC,[31] the question remains whether the typically larger SBA-15 type MSNs as hemocompatible. A more critical issue is that the mechanism of how MSNs of different sizes and surface areas correlate and contribute to their hemocompatibility is unclear, although several biological rationales have been suggested.[30,31] To address these questions, we prepared two types of MSNs: MCM-41 and SBA-15, as described in the Methods section. Scanning electron microscopy (SEM) and transmission electron microscopy (TEM) images showed particle sizes of 100 to 200 nm for the MCM-41-type MSNs (referred to as *s*-MSN, Figure 1a,d) and ~600 nm by ~300 nm for the SBA-15-type MSNs (referred as *l*-MSN, Figure 1b,e). The hydrodynamic particle size distributions of the materials suspended in phosphate-buffered saline (PBS) (100 μg mL^{-1}) were determined by dynamic light scattering (DLS), giving average sizes of 122 nm for *s*-MSN and 531 nm for *l*-MSN (Figure 1c). XRD patterns showed that both *s*-MSNs and *l*-MSNs exhibit 2D hexagonal pore arrangements (Figure 1f).

The hemolysis assay was used to evaluate the hemolytic behaviors of *s*-MSN and *l*-MSN on human RBCs. Human RBCs were first isolated by centrifugation and purified by five successive washes with sterile isotonic PBS, then diluted to 5% hematocrit with PBS before incubating with MSN suspensions of various concentrations. Controls were prepared in the same manner as the above RBC samples except adding water (positive control) and PBS (negative control) instead of the MSN suspensions. After a two-hour incubation at room temperature, the samples were spun down for the detection of hemoglobin released

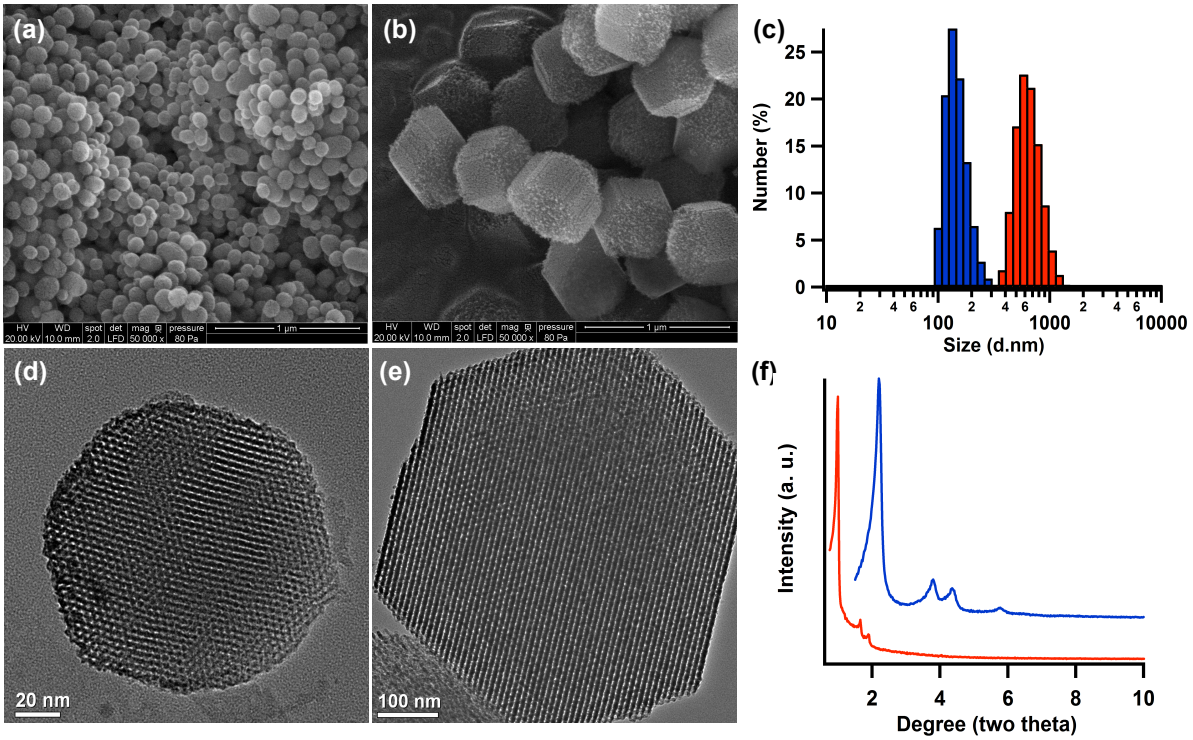

Figure 1. Scanning electron (top) and transmission electron (bottom) images of (a, d) *s*-MSN and (b, e) *l*-MSN. (c) Hydrodynamic size distributions of *s*-MSN (blue) and *l*-MSN (red) suspended in PBS (100 μg mL^{-1}) measured by dynamic light scattering. (f) X-ray diffraction patterns of *s*-MSN (blue) and *l*-MSN (red).

from hemolyzed RBCs. Surprisingly, contrary to the recently reported trend regarding size,[31] MSNs with larger particle size exhibited a higher hemolytic activity than the small particles (Figure 2). The hemolytic activity of *l*-MSNs was first observed at 50 μg mL^{-1} with 5% hemolysis detected, while a good hemocompatibility (< 2% hemolysis) of *s*-MSN was confirmed at concentrations as high as 100 μg mL^{-1}. While a larger particle size may be preferable for hemocompatible MSNs below 225 nm,[31] increasing particle size of MSNs beyond this range will not necessarily improve the hemocompatibility as one might intuitively expect. In addition to particle size, other factors such as the surface area are also expected to affect the hemolytic potential of MSNs.

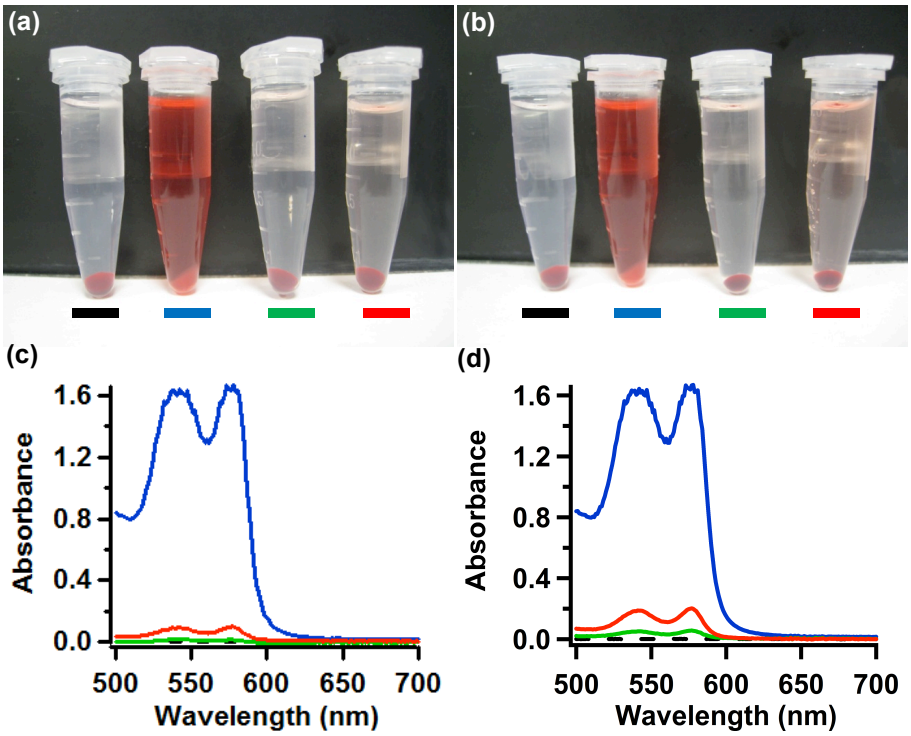

Figure 2. Hemolysis assay for *s*-MSN (green lines) and *l*-MSN (red lines), using water as a positive control (blue lines) and PBS as a negative control (dashed black lines). The materials were suspended at 50 (a, c) and 100 μg mL^{-1} (b, d). The mixtures were centrifuged to detect the presence of hemoglobin in the supernatant visually (a, b) and by absorption at 541 nm (c, d).

To elucidate the mechanism of the observed difference in hemolysis and investigate the underlying particle size and surface effects, the interaction of MSNs with RBCs were visualized by SEM (Figure 3) and TEM (Figure 4). A small proportion of *s*-MSNs were found to adsorb to the surface of RBC. The cell membrane did not show any alteration upon particle binding and RBCs maintained normal biconcave shape compared to control RBCs (Figure 3B and Figure 4 top). In contrast, a large proportion of *l*-MSNs attached to RBC membranes and induced a strong local membrane deformation, which frequently resulted in particle encapsulation by RBCs (Figure 3C and Figure 4 bottom). The membrane wrapping

around *l*-MSNs led to an echinocytic (spiculated) shape transformation of RBCs and a reduction in the ratio of surface area to volume.[42] This inability to maintain their normal surface area and control their cell volume can ultimately lead to the destruction of these cells,[42] which explains the observed high hemolytic activity of *l*-MSNs.

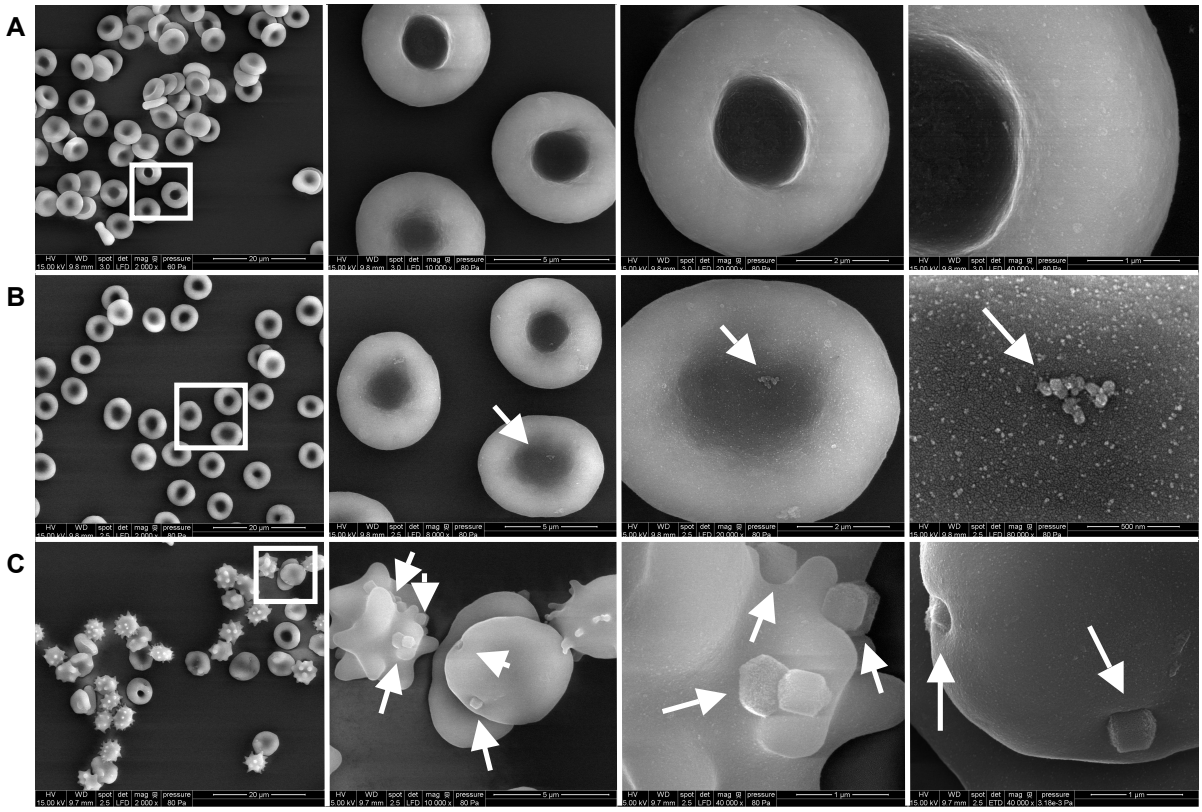

Figure 3. Scanning electron images of RBCs (5% hematocrit) incubated for 2 h at room temperature with (A) PBS as control, (B) 100 μg mL^{-1} of *s*-MSN and (C) 100 μg mL^{-1} of *l*-MSN. Images increase in magnification from left to right with features highlighted with white squares or arrows. The nanoparticles attached on cell surface are distinguished by the particle shape and surface textural difference between the particles and RBCs. (Additional high magnification images are shown in Figure S2.)

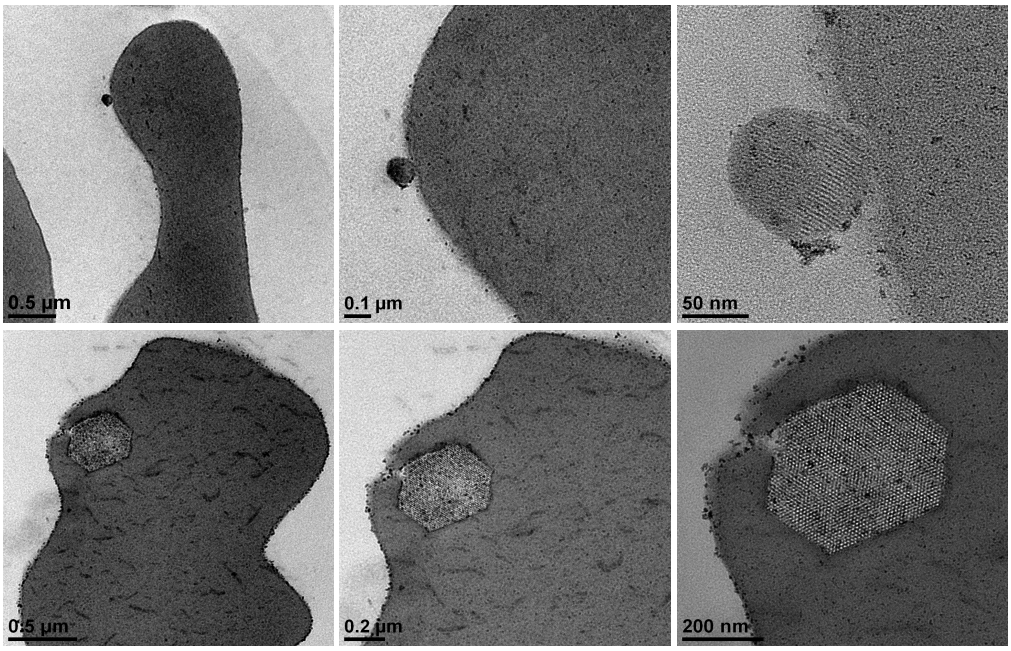

Figure 4. Transmission electron images of RBCs (5% hematocrit) incubated for 2 h at room temperature with 100 μg mL^{-1} *s*-MSN (top) and *l*-MSN (bottom). Images increase in magnification from left to right. The presence of MSNs is confirmed by the visible pores in the higher magnification micrographs.

Two main processes are involved in the interaction of MSN with the membrane of RBC: (1) binding of the silanol-rich surface of MSNs with the phosphatidyl choline-rich RBC membrane,[30] and (2) bending of the RBC membrane to adapt to the rigid surface of MSNs (Scheme 1).[43-47] The occurrence of the interaction depends on whether the amount of energy released from the binding of the MSNs with the RBC membrane (E_i) is able to overcome the amount of free energy required to bend the membrane and adapt to the surface of MSNs (E_b). The former energy is associated with the external surface area (*i.e.*, accessible silanols) of MSN,[30] while the latter is proportional to the curvature or inversely proportional to the square of the radius (r) of the particle.[43,44,47] The external surface areas of *s*-MSNs and *l*-MSNs, calculated from the t-plots of their N_2 adsorption isotherms,[48] were 81.6 and 155.4 m^2 g^{-1}, respectively. The relatively large external surface area of *l*-MSN (40% of total

surface area) in comparison to that of *s*-MSN (8% of total surface area) implies that *l*-MSN can have a larger binding energy (E_i) available for pulling the membrane to the particle surface. In addition, since surface curvature decreases with particle size, the bending energy required to wrap the large particles (E_b) is lower than the one needed to wrap the smaller particles.[43] This combination makes membrane wrapping and engulfment of *l*-MSN thermodynamically favorable. On the contrary, in order for the RBC membranes to wrap around smaller *s*-MSNs, they would have to attain a larger curvature (steeper angles over smaller areas) than they need for wrapping around the larger particles.[43] This would require investing a much higher E_b compared to the small amount of E_i, which thermodynamically prevents the membrane deformation or engulfment of *s*-MSN by RBC, and explains the lower hemolytic activity of *s*-MSNs. Similar explanations on the effect of particle size on membrane wrapping have been reported elsewhere.[43,44] Hence, the interaction of MSNs with RBC membranes and the hemolytic activity depends on not only particle size but on their external surface area as well.

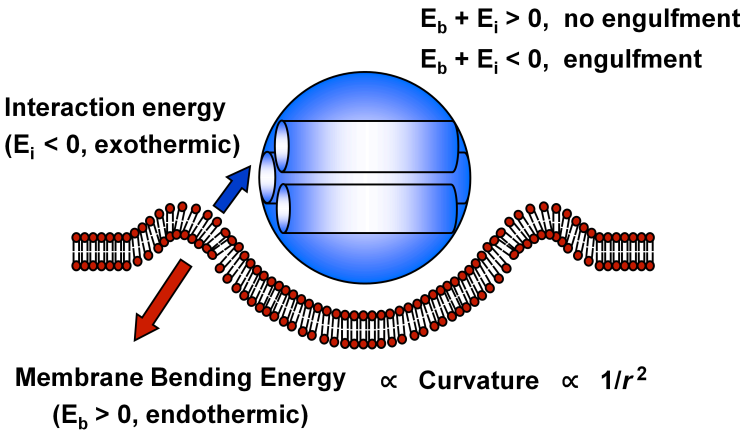

Scheme 1. A schematic illustration of the size- and surface-dependent interaction of MSN and RBC membrane. MSN with radius *r* can be wrapped around or engulfed by RBC if the energy (E_i) released from RBC-MSN interaction is greater than the energy (E_b) required for membrane bending.

2.2. Size- and surface-dependent engulfment of MSNs by RBCs

Though the *in vitro* endocytosis of MSN has been systematically investigated with various mammalian cell lines,[4,11,17,34,36,49-52] little is known about the uptake of nanoparticles by RBCs. This is partly because the interactions between RBC and MSN are still poorly understood. Before investigating the internalization of MSNs by RBC, it is necessary to establish the concentration at which the plasma membrane maintains its integrity and RBCs retain normal biconcave shape. To do so, the RBCs were incubated with *l*-MSNs at different concentrations; and the hemolytic effects as well as the resulting cell morphologies were examined by UV-Vis spectroscopy (Figure S3 in Supporting Information) and SEM (Figure S4). The hemolysis percentage of RBCs increased from 1% to 11% as the concentration of *l*-MSN raised from 20 to 100 μg mL^{-1}, and growing proportions of spiculated RBCs were observed with increasing concentrations of *l*-MSN. As shown in Figure S4, almost 90% of RBCs exhibited spiculated shape with 100 μg mL^{-1} of *l*-MSN. The proportion of spiculated RBCs decreased to 50% when 50 μg mL^{-1} of *l*-MSN was used. Interestingly, only minor shape modifications (less than 10% spiculated cells) in RBCs were observed after incubation with 20 μg mL^{-1} of *l*-MSN, even if many particles were adsorbed to the membranes or underwent internalization (Figure S4 left). Therefore, the cellular uptake process was examined at a concentration of 20 μg mL^{-1} of *l*-MSN (Figure 5). It should be noted that the images in Figure 5 correspond to different cells at different stages of nanoparticle encapsulation. A plausible interpretation of our observations is as follows. The particle interacts with an initially flat cell membrane. Driven by a local reduction in free energy (Scheme 1), the phospholipids in the immediate neighborhood of the site of contact are drawn to the surface of the particle, leading to membrane wrapping and eventual

encapsulation. Such internalization is different from phagocytosis or endocytosis, since it appears to be driven by the balance of two opposing forces rather than by an active uptake of nutrients by the cell. It should be stressed that even if almost no hemolysis or spiculation is observed at this concentration we cannot yet exclude the potential side effects of the internalization of *l*-MSN into RBC. Nevertheless, this preliminary study on MSN engulfment by RBC is an important step toward establishing the plausibility of using MSNs as tools for the treatment of RBC related diseases or intravascular drug delivery. We are currently conducting more studies to understand and control the internalization of MSNs and the delivery of therapeutic agents into RBCs to be published in subsequent manuscripts.

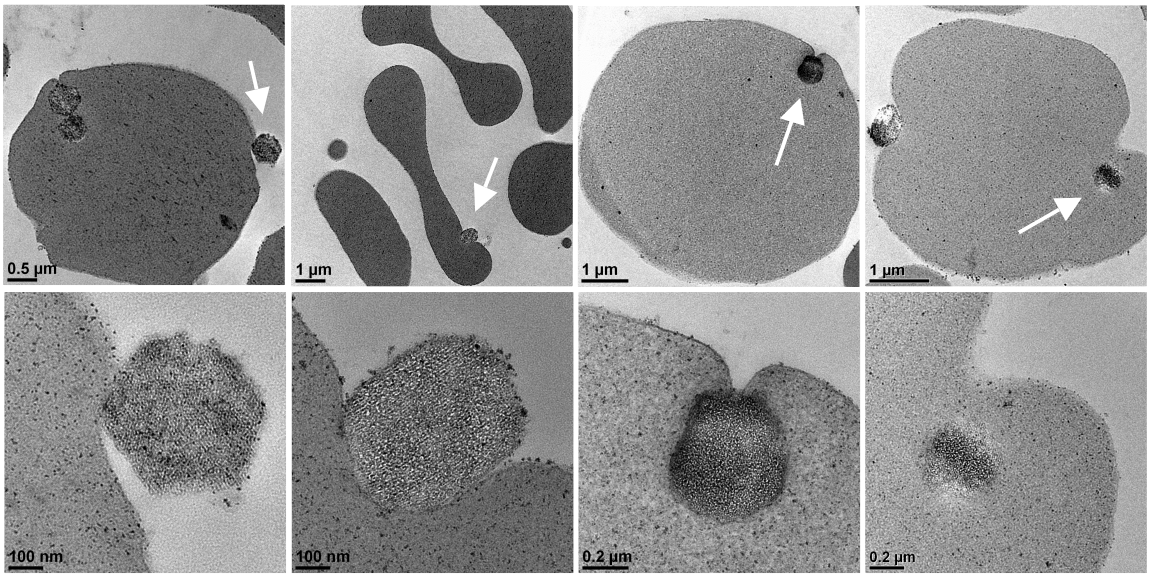

Figure 5. Cellular uptake process (left to right) examined by transmission electron microscopy of RBCs (5% hematocrit) incubated with 20 μg mL^{-1} *l*-MSN. Images increase in magnification from top to bottom, with features highlighted in white arrows. These images (left to right) correspond to different cells at different stages of nanoparticle encapsulation.

2.3. Surface functionality effects on RBC-MSN interaction

The results from the size- and surface-dependent interactions of MSNs with RBCs have demonstrated a superior hemocompatibility of *s*-MSNs over *l*-MSNs. This does not imply, however, that *s*-MSNs lack any interaction with the membranes of RBCs. While the interactions of MSNs with the membranes of RBCs is known to be dependent on the presence of silanol groups on the surface of the particles,[30,31] there is no quantitative information on the magnitude of this association. Given the interest of utilizing *s*-MSNs for intravenous drug delivery it is necessary to be able to measure and control the degree of the abovementioned interactions and, thus, controlling the circulation of the particles in the bloodstream.[40,53]

To study these interactions, *s*-MSNs were first labeled with fluorescein isothiocyanate (FITC), which enabled their tracking by flow cytometry and confocal fluorescence microscopy. FITC-*s*-MSNs were then functionalized with different amounts of aminopropyl (AP), polyethylene glycol (PEG) and carboxyl (CA) groups, as described in the Methods section. These functionalized materials are referred as AP_x-FITC-*s*-MSN, PEG_x-FITC-*s*-MSN and CA_x-FITC-*s*-MSN, respectively; where the subscript *x* corresponds to the number of mmol introduced per gram of material. The amount of functional groups (AP, PEG and CA) grafted on MSNs was quantified by TGA shown in Figure S5 bottom and summarized in Table S1. The quantification of nanoparticle attachment to the membrane of RBCs was performed by flow cytometry. Diluted suspensions of RBCs (5×10^6 cells mL^{-1}) were mixed with equal volumes of nanoparticle suspensions to reach a final concentration of 10 μg mL^{-1} of MSNs and incubated at room temperature for 2 h before flow cytometry analysis. As shown in Figure 6, the functionalized nanoparticles exhibited lower affinity to RBC than FITC-*s*-MSNs, furthermore, the affinity decreased with increasing degree of functionality.

This trend was observed for each functionalized material, independent of the surface charge. In particular, AP and PEG groups (~25% of RBC bound with $AP_{1.5}$-FITC-*s*-MSN and ~20% with PEG_1-FITC-*s*-MSN) showed a significantly better ability to reduce the MSN binding with RBC than CA groups (~65% of RBC bound with $CA_{1.5}$-FITC-*s*-MSN). The inhibitory effect of PEG on the adsorption of MSN to RBC was not surprising, since PEGylation of nanoparticles is generally used to block nonspecific binding of nanoparticles to proteins.[54] On the contrary, the reduction of MSN binding to RBC due to aminopropyl group functionalization, was completely unexpected, since amines are well known to facilitate adsorption of several biomolecules to the surface of nanoparticles and facilitate many nanoparticle-cell interactions.[34,55] The reduced binding of AP-FITC-*s*-MSN to RBC could be explained by the electrostatic interaction between amino groups on the surface of MSNs and surface silanols,[56] which diminishes the accessibility of silanol groups to the cell membrane.

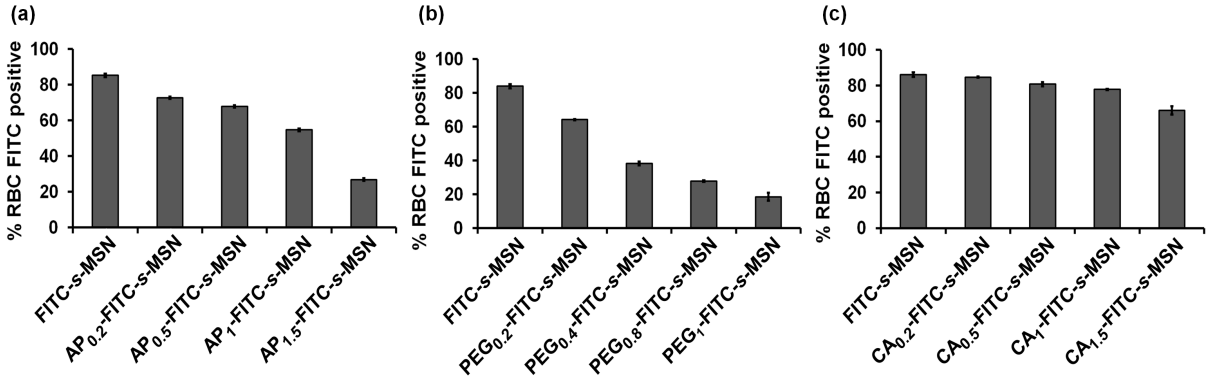

Figure 6. Flow cytometry measurement of RBCs (5×10^6 cells mL^{-1}) incubated with 10 μg mL^{-1} of (a) AP_x-FITC-*s*-MSN, (b) PEG_x-FITC-*s*-MSN and (c) CA_x-FITC-*s*-MSN.

The results obtained by flow cytometry were further confirmed by examination of the mixtures of the derivatized MSNs with RBCs under confocal fluorescence microscopy. For this purpose, RBCs were first labeled with PKH26 red fluorescent dye (Sigma) and incubated

with FITC labeled particles at the same conditions as in the flow cytometry experiment. FITC-*l*-MSNs, FITC-*s*-MSNs and $CA_{1.5}$-FITC-*s*-MSNs (Figure 7a,b,e) were easily observed associated to PKH26-labeled RBCs. Conversely, only a small proportion of $AP_{1.5}$-FITC-*s*-MSNs (Figure 7c) and PEG_1-FITC-*s*-MSNs (Figure 7d) were found co-localized with PKH26-RBCs, while most of the particles were observed in the extracellular space. A series of movies showing each one of these combinations of MSNs and RBCs were prepared from micrographs taken at different z-positions by changing the focal plane every 0.5 μm, these movies can be found in the Supporting Information. The different affinities of each MSN for the RBCs were also confirmed by the different shifts of the green fluorescence intensities in the 2D dot plots from flow cytometry (Figure 7, bottom).

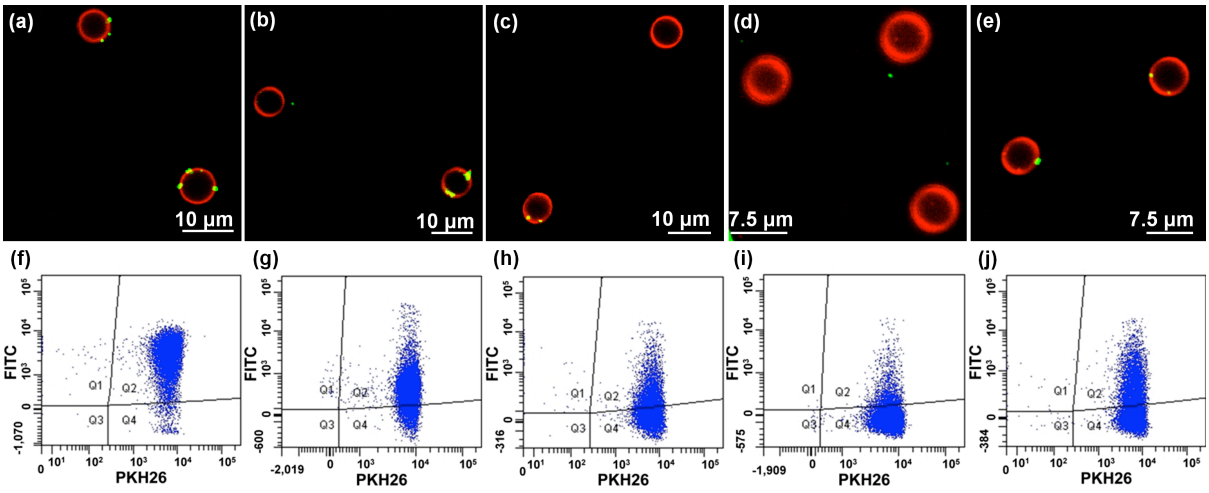

Figure 7. Confocal fluorescence micrographs (top) and dot plots from the flow cytometry analyses (bottom) of PKH26 labeled RBCs (5×10^6 cells mL^{-1}) incubated with 10 μg mL^{-1} of (a, f) FITC-*l*-MSN, (b, g) FITC-*s*-MSN, (c, h) $AP_{1.5}$-FITC-*s*-MSN, (d, i) PEG_1-FITC-*s*-MSN and (e, j) $CA_{1.5}$-FITC-*s*-MSN. The axes correspond to the intensity of red fluorescence due to PKH26 labeling (horizontal axis) and green fluorescence due to the attachment of FITC-MSNs onto PKH26-RBCs (vertical axis). The plot was gated to show PKH26 labeled RBCs in area Q4 and FITC-fluorescent PKH26-RBCs in area Q2. Individual channels for the merged confocal images and enlarged dot plots with PKH26-RBC control are shown in Figure S7 and Figure S8, respectively.

2.4. Effect of RBC-MSN interaction on RBC deformability

The attachment of nanoparticles to the surface of red blood cells has been suggested for extending the circulation time and sustained release of therapeutic agents.[40,53] Such attachment, however, could have an impact on the properties of the membrane affecting the normal function of RBCs. Surprisingly, this potential problem has not been addressed for any nanoparticle-based drug carrier, to the best of our knowledge. One of the key properties of RBCs (6-8 μm in diameter) is their ability to undergo deformation to traverse the capillaries of the microvascular system (2-3 μm in diameter). This remarkable deformability of RBCs is critical for effective blood flow, and depends strongly on the flexibility of the cell membrane. This is the reason why it is important to assess the effects of MSN attachment on the deformability of RBCs.

To study the deformability of RBCs, we used a literature reported method consisting of filtering the cells through polycarbonate membranes with straight channels of 3 μm pore diameter (Nucleopore).[41] This technique is generally accepted as a relative indication of RBC deformability.[41,57-59] We measured the filterability of fresh human RBCs (5% hematocrit) previously incubated with varying concentrations (10, 20, 50 μg mL^{-1}) of MSN under a constant negative pressure (-20 cm H_2O). The time it took each RBC suspension to flow through the membrane was recorded and the deformability index (DI) was expressed as the volume (mL) of red blood cells filtered per minute. As shown in Figure 8a, the deformability of RBC decreased with increasing concentrations of all MSN materials. The RBC deformability was severely impaired by *l*-MSN at concentrations as low as 10 μg mL^{-1}.

This result is not surprising given the strong affinity and shape altering effects already described for *l*-MSN. As expected, the incorporation of AP and PEG groups to the surface of *s*-MSN preserved the elasticity of RBCs better than the non-functionalized *s*-MSN and the CA-*s*-MSN, especially at the higher concentrations (> 20 μg mL^{-1}). These results correlate well with the observed effects on the degree of RBC-MSN interactions (Figure 8b). These observations suggest that the attachment of MSNs to the surface of RBCs restrict the flexibility of the membrane and lead to impairment in the deformability of RBCs. Conversely, the attachment of functional groups to the surface of MSNs reduces the affinity of the particles to the membrane of RBC and allows the cells to preserve their deformability.

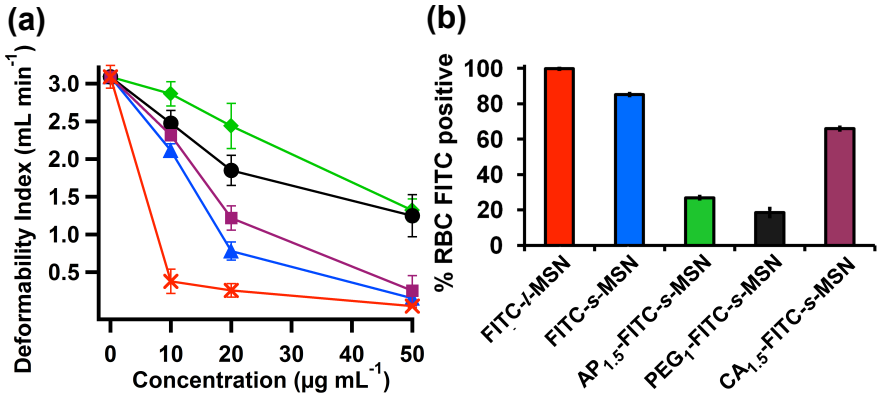

Figure 8. (a) Deformability Index (DI) of RBCs incubated with *s*-MSN (blue), AP$_{1.5}$-*s*-MSN (green), PEG$_1$-*s*-MSN (black), CA$_{1.5}$-*s*-MSN (purple) and *l*-MSN (red). (b) Flow cytometry analyses of RBCs incubated with FITC-*l*-MSN (red), FITC-*s*-MSN (blue), AP$_{1.5}$-FITC-*s*-MSN (green), PEG$_1$-FITC-*s*-MSN (black), and CA$_{1.5}$-FITC-*s*-MSN (purple).

3. Conclusion

In this study, we investigated the interactions between MSNs of different particle sizes and surface properties and RBC membranes by using fluorescence and electron microscopies and cell biology techniques. We compared the size- and surface-dependent hemocompatibility of two types of MSN materials (MCM-41 and SBA-15) and showed, for

the first time, how MSNs are engulfed by RBCs. This size- and surface-dependent process is the resultant of two opposing forces, namely: the attractive interaction between MSNs and RBCs, and the bending of the cell membrane. These results suggest that only small MCM-41 type MSN materials (100-200 nm) may be considered as potentially safe candidates for intravascular drug delivery. It must be noted that although RBCs are the dominant cells in blood, the interactions of these nanoparticles with other blood cells and components[60,61] should be also evaluated to ensure the safe use of these materials for biomedical applications. In addition, we demonstrated that the biocompatibility of these MSN materials with RBCs strongly depends on their surface derivatization to minimize their interaction with red blood cells. Blocking the surface silanols of the particles with organic groups reduces their interactions with the membranes of RBCs. Minimizing these interactions has a dramatic effect on preserving the deformability of RBCs, which is necessary to ensure effective blood circulation. These findings suggest that it is possible to gain control over the interactions of MSNs with RBC membranes in order to regulate their circulation half lives for various therapeutic purposes, while minimizing their toxicity by carefully choosing and tuning their surface functionalities. As new MSN-based drug delivery systems burgeon from many international research groups, our results will provide a practical guide to size and surface considerations when designing MSN-based drug carriers for delivery, diagnostic, and therapeutic applications.

4. Methods

Synthesis of Mesoporous Silica Nanoparticles. *s*-MSN was prepared by our previously reported method.[33] In brief, N-cetyltrimethylammonium bromide (CTAB, 1.00 g,

2.74 mmol) was dissolved in 480 mL nanopure water, followed by the addition of 3.5 mL sodium hydroxide aqueous solution (2.0 M), and the mixture was heated to 80 °C. Tetraethoxysilane (TEOS, 5.0 mL, 22.4 mmol) was added dropwise to the surfactant solution under vigorous stirring. The reaction mixture was stirred at 80 °C for another 2 h. The resulting white solid was filtered, washed thoroughly with water and methanol, and dried under high vacuum at 80 °C overnight. The fluorescent labeled MSN (FITC-*s*-MSN) was synthesized by reacting fluorescein isothiocyanate (FITC, 15 mg, 38.5 μmol) with (3-aminopropyl)trimethoxysilane (APTMS, 10 μL, 57.3 μmol) for 2 hours in dimethyl sulfoxide (DMSO), and adding the resulting product following the addition of TEOS in the above synthesis. The unlabeled FITC was removed by soxhlet extraction with methanol. The amount of FITC labeled on FITC-*s*-MSN was quantified to be 20-30 μmol g^{-1} by TGA. The functionalization of *s*-MSN and FITC-*s*-MSN with aminopropyl (AP), polyethylene glycol (PEG) and carboxylate (CA) groups was performed by refluxing a suspension of the as-made material (200 mg of *s*-MSN or FITC-*s*-MSN) with APTMS, 2-[methoxy(polyethylenoxy)-propyl]trimethoxysilane (PEG-silane) and 3-(triethoxysilyl)propylsuccinic anhydride of various amount (*x* mmol) in anhydrous toluene (50 mL) for 20 h, followed by filtration and washing with toluene and methanol, and dried under high vacuum overnight. The succinic anhydride groups were hydrolyzed by boiling the materials in water for 6 hours and measured by FTIR. The CTAB surfactant was removed by refluxing the materials in 0.37% HCl methanol, followed by filtration and washing with abundant methanol and dried under high vacuum. The amount of functional groups (AP, PEG and CA) grafted on MSNs was quantified by TGA shown in Figure S5 bottom and summarized in Table S1.

l-MSN was prepared by a modified literature procedure.[5] Pluronic P104 (courtesy of BASF, 7.0 g) was dissolved in a mixture of water (164 g) and HCl (109 g, 4M) and stirred at 55 °C for 1 hour. Tetramethyl orthosilicate (10.64 g) was quickly added into the solution at 55 °C. After continuous stirring for 24 hours, the reaction mixture was moved to a teflon-lined, high-pressure autoclave for further hydrothermal treatment at 150 °C for 24 h. The product was isolated by filtration, washed with copious water and methanol, and dried at 80 °C in air. The Pluronic P104 surfactant was removed by calcination at 550 °C for 6 hours. The *l*-MSN was fluorescently labeled (FITC-*l*-MSN) by reacting FITC (15 mg, 38.5 μmol) with APTMS (10 μL, 57.3 μmol) for 2 hours in dimethyl sulfoxide (DMSO), and adding the resulting product to a suspension of *l*-MSN (1 g) in anhydrous toluene (100 mL) for 20 h, followed by filtration and washing with toluene and methanol. The unlabeled FITC was removed by soxhlet extraction with methanol as the solvent. The amount of FITC labeled on FITC-*l*-MSN was quantified to be around 30 μmol g^{-1}.

The products were characterized by X-ray diffraction in a Rigaku Ultima IV diffractometer, nitrogen sorption analysis in a Micromeritics Tristar 3000 surface area and porosity analyzer using Brunauer-Emmett-Teller (BET) equation to calculate apparent surface area and pore volume and the Barret-Joyner-Halenda (BJH) method to calculate pore size distribution, thermogravimetric analysis (TGA) in a TGA 2950 thermogravimetric analyzer with a temperature ramp of 5 °C/min in air, dynamic light scattering size analyses of particle suspensions in a Malvern Nano HT Zetasizer, scanning electron microscopy (SEM) of samples coated with gold in a FEI Quanta 250 FEG microscope, and transmission electron microscopy (TEM) of samples supported on copper grids in a Tecnai G2 F20 microscope

operated at 200 kV. FTIR spectroscopy was performed using a Nicolet Nexus 470 (Madison, EI), equipped with a cooled CT/A detector and an Ever-Glo source.

Isolation and labeling of red blood cells (RBCs). Ethylenediamine tetraacetic acid (EDTA)-stabilized human blood samples were freshly collected in the Occupational Medicine Office of Iowa State University and Ames Laboratory. Whole blood was centrifuged at 1600 rpm for 5 min and the plasma, buffy coat, and top layer of cells were decanted. The remaining packed RBCs were washed five times with sterile isotonic PBS. For labeling with PKH26 (Red fluorescent cell linker kit, Sigma, USA), 100 μL of packed RBCs were resuspended in 1 ml diluent C™ and mixed with 1 ml diluent C™ containing 4 μM PKH26. Cells were incubated for 5 min at room temperature in the dark. The reaction was stopped by adding 1 mL plasma (heat inactivated for 1 hour at 65°C beforehand) for 1 minute and centrifuged at 1600 rpm for 5 min. The stained RBCs were washed five times with PBS to remove free pKH26 dye.

Hemolysis assay. After cell washing, 200 μL of packed RBC was diluted to 4 mL with PBS (5% hematocrit). The diluted RBC suspension (0.2 mL) was then mixed with *s*-MSN and *l*-MSN suspensions in PBS (0.8 mL) at various concentrations. PBS and water (0.8 mL) were used instead of MSN suspensions as negative and positive control, respectively. The mixture was gently vortexed and incubated at room temperature for 2 h, followed by centrifuge (1600 rpm, 5 min) and the absorbance of the supernatant at 541 nm was measured by UV-Visible spectrometry. The percent hemolysis of RBCs was calculated using the following formula: percent hemolysis = ((sample absorbance - negative control absorbance)/(positive control absorbance - negative control absorbance)) × 100.

Scanning electron microscopy (SEM). The diluted RBC suspension (5% hematocrit, 0.2 mL) was mixed with *s*-MSN and *l*-MSN suspensions in PBS (0.8 mL) at various concentrations, and incubated at room temperature for 2 h. The samples were then fixed by adding a 1% glutaraldehyde solution dropwise over 5 min and further incubated at 37 °C for 1.5 h, followed by post-fixation with 1% osmium tetroxide in PBS for 1.5 h. Cells were dehydrated in increasing concentrations of ethanol (50%, 60% 70%, 80%, 90%, and 100%) for 15 min each. The cell suspensions were dropped onto glass coverslips, dried, and coated with Au before viewing under a FEI Quanta 250 FEG scanning electron microscope.

Transmission Electron Microscopy (TEM). The samples were prepared, fixed and dehydrated as above, and stained with 2% uranyl acetate in 70% ethanol at room temperature overnight. The cells were washed three times with acetone and embedded in Epon. The embedded samples were sectioned in 60 nm thick slices on a sliding ultramicrotome. Thin sections supported on copper grids were examined in a Tecnai G2 F20 microscope operated at 200 kV.

Flow cytometry. After cell washing, 200 μL of RBC suspension at 5×10^6 cells mL^{-1} were mixed with 200 μL of FITC-MSN suspensions in PBS at 20 μg mL^{-1}, and incubated at room temperature for 2 h before flow cytometry analysis in a BD FACSCanto instrument.

Confocal Fluorescence Microscopy. 200 μL of PKH26 labeled RBC suspension at 5×10^6 cells mL^{-1} were mixed with 200 μL of FITC-MSN suspensions in PBS at 20 μg mL^{-1}, and incubated at room temperature for 2 h. An aliquot of sample was mounted between plastic coverslips and imaged in a Leica SP5 X confocal system.

Deformability assay. 1.5 mL of packed RBCs were washed and diluted to 30 mL with PBS (5% hematocrit). The diluted RBC suspension (1 mL) was then mixed with MSN

suspensions in PBS (4 mL) at various final concentrations of 10, 20 and 50 μg mL^{-1} with PBS as control. The mixture was gently vortexed and incubated at room temperature for 2 h before filtering through polycarbonate membrane with straight channels of 3 μm pore diameter (Nucleopore, Fisher, USA) under a constant negative pressure (-20 cm H_2O). The time for 0.5 mL RBC suspension to pass through the membrane was recorded and the deformability index (DI) was calculated as the volume of red blood cells filtered per minute. Data were presented as mean values of triplicate experiments. The present method and apparatus for RBC filterability measurement have been described in detail elsewhere.[41]

ACKNOWLEDGEMENT

This manuscript has been dedicated in memory of our dear mentor and friend, Victor S.-Y. Lin. This research is supported by the U.S. National Science Foundation NSF (CHE-0809521).

REFERENCES

(1) Slowing, I. I.; Vivero-Escoto, J. L.; Trewyn, B. G.; Lin, V. S. Y. *J. Mater. Chem.* **2010**, *20*, 7924.

(2) Cai, Q.; Lin, W. Y.; Xiao, F. S.; Pang, W. Q.; Chen, X. H.; Zou, B. S. *Microporous Mesoporous Mater.* **1999**, *32*, 1.

(3) Huh, S.; Wiench, J. W.; Yoo, J.-C.; Pruski, M.; Lin, V. S. Y. *Chem. Mater.* **2003**, *15*, 4247.

(4) Lu, F.; Wu, S.-H.; Hung, Y.; Mou, C.-Y. *Small* **2009**, *5*, 1408.

(5) Linton, P.; Alfredsson, V. *Chem. Mater.* **2008**, *20*, 2878.

(6) Descalzo, A. B.; Martinez-Manez, R.; Sancenon, F.; Hoffmann, K.; Rurack, K. *Angew. Chem., Int. Ed.* **2006**, *45*, 5924.

(7) Coti, K. K.; Belowich, M. E.; Liong, M.; Ambrogio, M. W.; Lau, Y. A.; Khatib, H. A.; Zink, J. I.; Khashab, N. M.; Stoddart, J. F. *Nanoscale* **2009**, *1*, 16.

(8) Zhao, Y.; Vivero-Escoto, J. L.; Slowing, I. I.; Trewyn, B. G.; Lin, V. S. Y. *Expert Opin. Drug Delivery* **2010**, *7*, 1013.

(9) Shen, S.; Chow, P. S.; Chen, F.; Tan, R. B. H. *Chem. Pharm. Bull.* **2007**, *55*, 985.

(10) Vivero-Escoto, J. L.; Slowing, I. I.; Trewyn, B. G.; Lin, V. S. Y. *Small* **2010**, *6*, 1952.

(11) Slowing, I. I.; Trewyn, B. G.; Lin, V. S. Y. *J. Am. Chem. Soc.* **2007**, *129*, 8845.

(12) Kim, S.-I.; Pham, T. T.; Lee, J.-W.; Roh, S.-H. *J. Nanosci. Nanotechnol.* **2010**, *10*, 3467.

(13) Nguyen, T. P. B.; Lee, J.-W.; Shim, W. G.; Moon, H. *Microporous Mesoporous Mater.* **2008**, *110*, 560.

(14) Doadrio, J. C.; Sousa, E. M. B.; Izquierdo-Barba, I.; Doadrio, A. L.; Perez-Pariente, J.; Vallet-Regi, M. *J. Mater. Chem.* **2006**, *16*, 462.

(15) Zhu, Y.; Kaskel, S.; Ikoma, T.; Hanagata, N. *Microporous Mesoporous Mater.* **2009**, *123*, 107.

(16) Mercuri, L. P.; Carvalho, L. V.; Lima, F. A.; Quayle, C.; Fantini, M. C. A.; Tanaka, G. S.; Cabrera, W. H.; Furtado, M. F. D.; Tambourgi, D. V.; Matos, J. d. R.; Jaroniec, M.; Sant'Anna, O. A. *Small* **2006**, *2*, 254.

(17) Zhao, Y.; Trewyn, B. G.; Slowing, I. I.; Lin, V. S. Y. *J. Am. Chem. Soc.* **2009**, *131*, 8398.

(18) Lee, J. E.; Lee, N.; Kim, H.; Kim, J.; Choi, S. H.; Kim, J. H.; Kim, T.; Song, I. C.; Park, S. P.; Moon, W. K.; Hyeon, T. *J. Am. Chem. Soc.* **2010**, *132*, 552.

(19) Liong, M.; Lu, J.; Kovochich, M.; Xia, T.; Ruehm, S. G.; Nel, A. E.; Tamanoi, F.; Zink, J. I. *ACS Nano* **2008**, *2*, 889.

(20) Tu, H.-L.; Lin, Y.-S.; Lin, H.-Y.; Hung, Y.; Lo, L.-W.; Chen, Y.-F.; Mou, C.-Y. *Advanced Materials* **2009**, *21*, 172.

(21) Taylor, K. M. L.; Kim, J. S.; Rieter, W. J.; An, H.; Lin, W.; Lin, W. *J. Am. Chem. Soc.* **2008**, *130*, 2154.

(22) Lee, C.-H.; Cheng, S.-H.; Wang, Y.-J.; Chen, Y.-C.; Chen, N.-T.; Souris, J.; Chen, C.-T.; Mou, C.-Y.; Yang, C.-S.; Lo, L.-W. *Adv. Funct. Mater.* **2009**, *19*, 215.

(23) Lu, J.; Liong, M.; Li, Z.; Zink, J. I.; Tamanoi, F. *Small* **2010**, *6*, 1794.

(24) Kim, J.; Kim, H. S.; Lee, N.; Kim, T.; Kim, H.; Yu, T.; Song, I. C.; Moon, W. K.; Hyeon, T. *Angew. Chem., Int. Ed.* **2008**, *47*, 8438.

(25) Meng, H.; Liong, M.; Xia, T.; Li, Z.; Ji, Z.; Zink, J. I.; Nel, A. E. *ACS Nano* **2010**, *4*, 4539.

(26) Tao, Z.; Morrow, M. P.; Asefa, T.; Sharma, K. K.; Duncan, C.; Anan, A.; Penefsky, H. S.; Goodisman, J.; Souid, A.-K. *Nano Lett.* **2008**, *8*, 1517.

(27) Hudson, S. P.; Padera, R. F.; Langer, R.; Kohane, D. S. *Biomaterials* **2008**, *29*, 4045.

(28) Heikkilae, T.; Santos, H. A.; Kumar, N.; Murzin, D. Y.; Salonen, J.; Laaksonen, T.; Peltonen, L.; Hirvonen, J.; Lehto, V.-P. *Eur. J. Pharm. Biopharm.* **2010**, *74*, 483.

(29) Al Shamsi, M.; Al Samri, M. T.; Al-Salam, S.; Conca, W.; Shaban, S.; Benedict, S.; Tariq, S.; Biradar, A. V.; Penefsky, H. S.; Asefa, T. *Chem. Res. Toxicol.* **2010**, *23*, 1796.

(30) Slowing, I. I.; Wu, C.-W.; Vivero-Escoto, J. L.; Lin, V. S. Y. *Small* **2009**, *5*, 57.

(31) Lin, Y.-S.; Haynes, C. L. *J. Am. Chem. Soc.* **2010**, *132*, 4834.

(32) Lin, Y.-S.; Haynes, C. L. *Chem. Mater.* **2009**, *21*, 3979.

(33) Lai, C.-Y.; Trewyn, B. G.; Jeftinija, D. M.; Jeftinija, K.; Xu, S.; Jeftinija, S.; Lin, V. S. Y. *J. Am. Chem. Soc.* **2003**, *125*, 4451.

(34) Slowing, I.; Trewyn, B. G.; Lin, V. S. Y. *J. Am. Chem. Soc.* **2006**, *128*, 14792.

(35) Radu, D. R.; Lai, C.-Y.; Huang, J.; Shu, X.; Lin, V. S. Y. *Chemical Communications* **2005**, 1264.

(36) Radu, D. R.; Lai, C.-Y.; Jeftinija, K.; Rowe, E. W.; Jeftinija, S.; Lin, V. S. Y. *J. Am. Chem. Soc.* **2004**, *126*, 13216.

(37) Hom, C.; Lu, J.; Liong, M.; Luo, H.; Li, Z.; Zink, J. I.; Tamanoi, F. *Small* **2010**, *6*, 1185.

(38) Torney, F.; Trewyn, B. G.; Lin, V. S. Y.; Wang, K. *Nat. Nanotechnol.* **2007**, *2*, 295.

(39) Wang, L.-S.; Wu, L.-C.; Lu, S.-Y.; Chang, L.-L.; Teng, I. T.; Yang, C.-M.; Ho, J.-a. A. *ACS Nano* **2010**, *4*, 4371.

(40) Chambers, E.; Mitragotri, S. *J. Controlled Release* **2004**, *100*, 111.

(41) Reid, H. L.; Barnes, A. J.; Lock, P. J.; Dormandy, J. A.; Dormandy, T. L. *J Clin Pathol* **1976**, *29*, 855.

(42) Yawata, Y. *Cell membrane : the red blood cell as a model*; Weinheim : Wiley-VCH, 2003.

(43) Roiter, Y.; Ornatska, M.; Rammohan, A. R.; Balakrishnan, J.; Heine, D. R.; Minko, S. *Nano Lett.* **2008**, *8*, 941.

(44) Lipowsky, R.; Dobereiner, H. G. *Europhys. Lett.* **1998**, *43*, 219.

(45) Deserno, M.; Gelbart, W. M. *J. Phys. Chem. B* **2002**, *106*, 5543.

(46) Fleck, C. C.; Netz, R. R. *Europhys. Lett.* **2004**, *67*, 314.

(47) Reynwar, B. J.; Illya, G.; Harmandaris, V. A.; Mueller, M. M.; Kremer, K.; Deserno, M. *Nature* **2007**, *447*, 461.

(48) Zhu, H. Y.; Zhao, X. S.; Lu, G. Q.; Do, D. D. *Langmuir* **1996**, *12*, 6513.

(49) Giri, S.; Trewyn, B. G.; Stellmaker, M. P.; Lin, V. S. Y. *Angew. Chem., Int. Ed.* **2005**, *44*, 5038.

(50) Vivero-Escoto, J. L.; Slowing, I. I.; Wu, C.-W.; Lin, V. S. Y. *J. Am. Chem. Soc.* **2009**, *131*, 3462.

(51) Zhu, C.-L.; Song, X.-Y.; Zhou, W.-H.; Yang, H.-H.; Wen, Y.-H.; Wang, X.-R. *J. Mater. Chem.* **2009**, *19*, 7765.

(52) He, Q.; Zhang, Z.; Gao, Y.; Shi, J.; Li, Y. *Small* **2009**, *5*, 2722.

(53) Hall, S. S.; Mitragotri, S.; Daugherty, P. S. *Biotechnol. Prog.* **2007**, *23*, 749.

(54) He, Q.; Zhang, J.; Shi, J.; Zhu, Z.; Zhang, L.; Bu, W.; Guo, L.; Chen, Y. *Biomaterials* **2010**, *31*, 1085.

(55) Gao, F.; Botella, P.; Corma, A.; Blesa, J.; Dong, L. *J. Phys. Chem. B* **2009**, *113*, 1796.

(56) Caravajal, G. S.; Leyden, D. E.; Quinting, G. R.; Maciel, G. E. *Anal. Chem.* **1988**, *60*, 1776.

(57) Luquita, A.; Urli, L.; Svetaz, M. J.; Gennaro, A. M.; Giorgetti, M. E.; Pistone, G.; Volpintesta, R.; Palatnik, S.; Rasia, M. *Journal of Biomedical Science* **2010**, *17*, 1.

(58) Brown Clinton, D.; Ghali Halim, S.; Zhao, Z.; Thomas Lorraine, L.; Friedman Eli, A. *Kidney Int* **2005**, *67*, 295.

(59) Kikuchi, Y.; Koyama, T. *Am. J. Physiol.* **1984**, *247*, H739.

(60) De Paoli Lacerda, S. H.; Park, J.-J.; Meuse, C.; Pristinski, D.; Becker, M. L.; Karim, A.; Douglas, J. F. *ACS Nano* **2010**, *4*, 365.

(61) Semberova, J.; De Paoli Lacerda, S. H.; Simakova, O.; Holada, K.; Gelderman, M. P.; Simak, J. *Nano Lett*. **2009**, *9*, 3312.

Appendix: Supporting Information

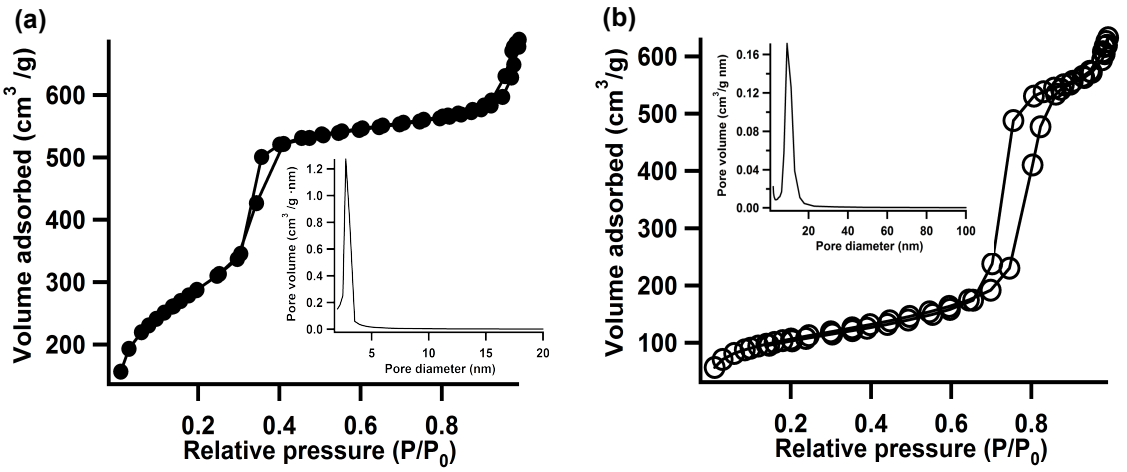

Figure S1. Linear plot of the nitrogen sorption isotherms and pore size distributions of **(a)** *s*-MSN and **(b)** *l*-MSN. Surface areas of *s*-MSN and *l*-MSN were calculated to be 1051.6 ± 2.2 $m^2\ g^{-1}$ and 387.0 ± 1.3 $m^2\ g^{-1}$, respectively.

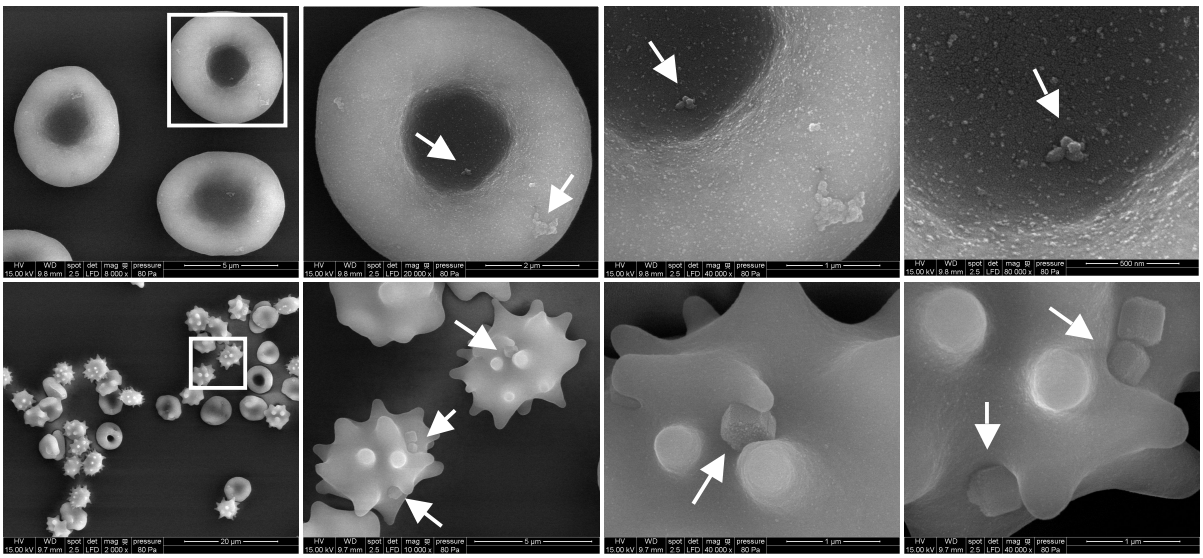

Figure S2. Scanning electron micrographs (SEM) of RBCs (5% hematocrit) incubated with 100 μg mL^{-1} *s*-MSN (top) and *l*-MSN (bottom). Images increase in magnification from left to right with features highlighted with white squares or arrows, indicating the location of particles attached on RBC membrane.

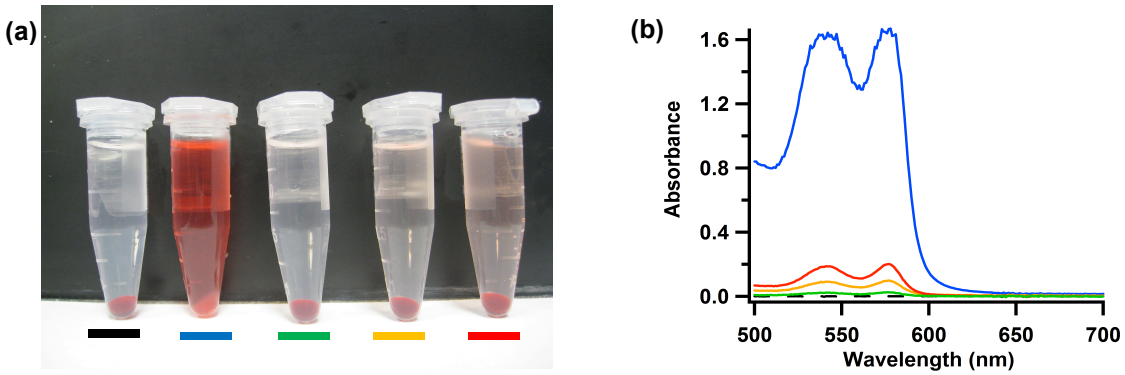

Figure S3. Hemolysis assay for *l*-MSN using water as a positive control (blue lines) and PBS as a negative control (dashed black lines). The materials were suspended at 20 (green), 50 (yellow) and 100 (red) μg mL^{-1}. The mixtures were centrifuged to detect the presence of hemoglobin (red) in the supernatant visually (a) and by absorption at 541 nm (b).

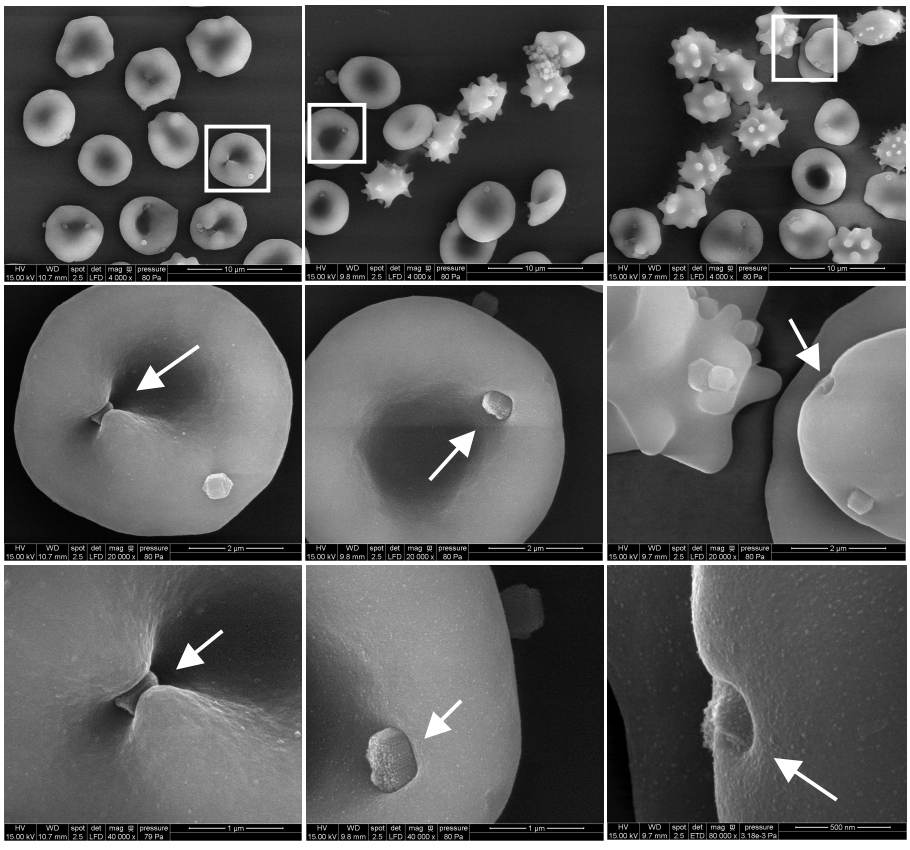

Figure S4. Scanning electron micrographs (SEM) of RBCs (5% hematocrit) incubated with 20 μg mL^{-1} (left), 50 μg mL^{-1}(middle), and 100 μg mL^{-1} of *l*-MSN (right). Percent of spiculated RBCs were observed to be < 10%, ~50% and ~90% from left to right. Images

increase in magnification from top to bottom with features highlighted with white squares or arrows, indicating the location of particles attached on RBC membrane.

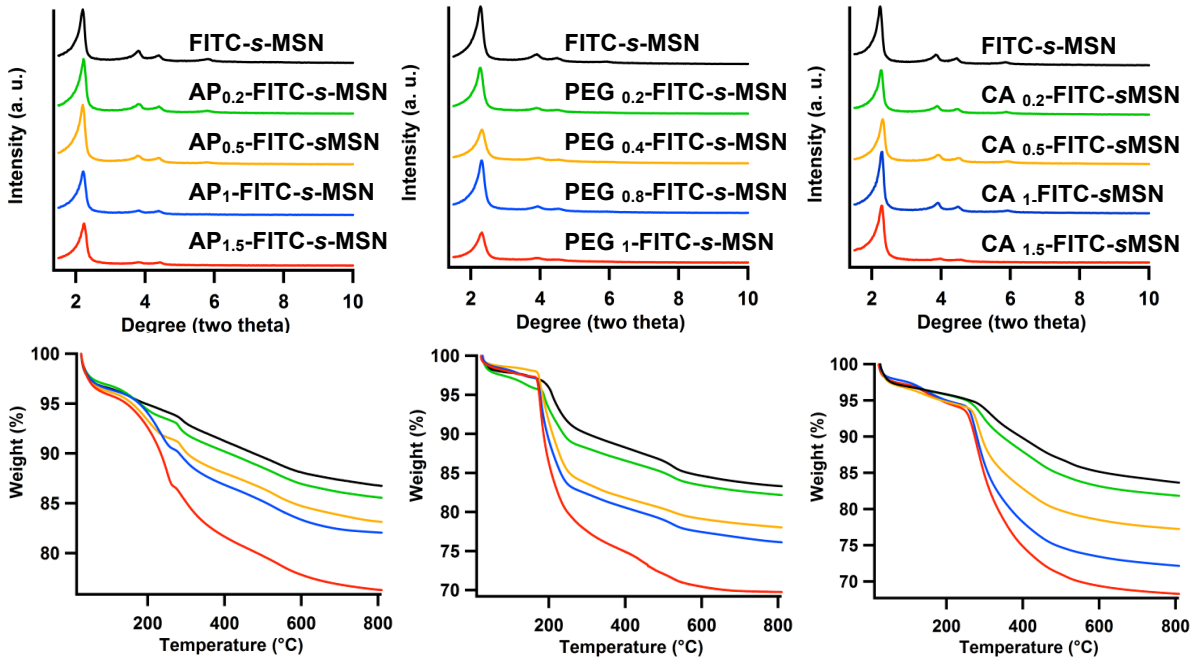

Figure S5. X-ray diffraction patterns (top) and thermogravimetric analysis (bottom) of FITC-*s*-MSN, AP_x-FITC-*s*-MSN (left), PEG_x-FITC-*s*-MSN (middle) and CA_x-FITC-*s*-MSN (right) (*x*: amount of organic groups introduced in mmol g^{-1}).

Table S1. Characteristics of FITC-*s*-MSN, AP_x-FITC-*s*-MSN, PEG_x-FITC-*s*-MSN and CA_x-FITC-*s*-MSN (*x*: amount of organic groups introduced in mmol g^{-1}).

Materials	Surface groups (mmol g^{-1})	Zeta potential (mV)	Surface area (m^2 g^{-1})	Pore size (nm)
FITC-*s*-MSN	0.02	-27.9	1043.4 ± 4.2	3.0
$AP_{0.2}$-FITC--*s*MSN	0.1-0.2	-22.9	948.3 ± 7.9	2.8
$AP_{0.5}$-FITC-*s*-MSN	0.4-0.6	-10.9	878.7 ± 11.7	2.8
AP_1-FITC-*s*-MSN	0.6-0.8	+3.2	796.8 ± 1.6	2.8
$AP_{1.5}$-FITC-*s*-MSN	1.2-1.6	+6.87	689.0 ± 29.0	2.7
FITC-*s*-MSN	0.03	-29.3	1036.4 ± 11.2	2.6
$PEG_{0.2}$-FITC-*s*-MSN	0.03-0.04	-26.1	985.6 ± 9.0	2.6
$PEG_{0.4}$-FITC-*s*-MSN	0.1-0.2	-22.3	839.6 ± 9.3	2.4
$PEG_{0.8}$-FITC-*s*-MSN	0.2-0.3	-20.7	770.8 ± 1.6	2.4
PEG_1-FITC-*s*-MSN	0.4-0.5	-13.1	628.9 ± 2.6	2.4
FITC-*s*-MSN	0.03	-28.6	1107.8 ± 8.6	2.7
$CA_{0.2}$-FITC-*s*-MSN	0.07-0.1	-34.3	967.4 ± 2.9	2.5
$CA_{0.5}$-FITC-*s*-MSN	0.3-0.4	-36.1	913.6 ± 19.2	2.4

CA_1-FITC-*s*-MSN	0.5-0.7	-39.2	863.0 ± 9.2	2.4
$CA_{1.5}$-FITC-*s*-MSN	0.7-1	-42.7	779.2 ± 5.0	2.5

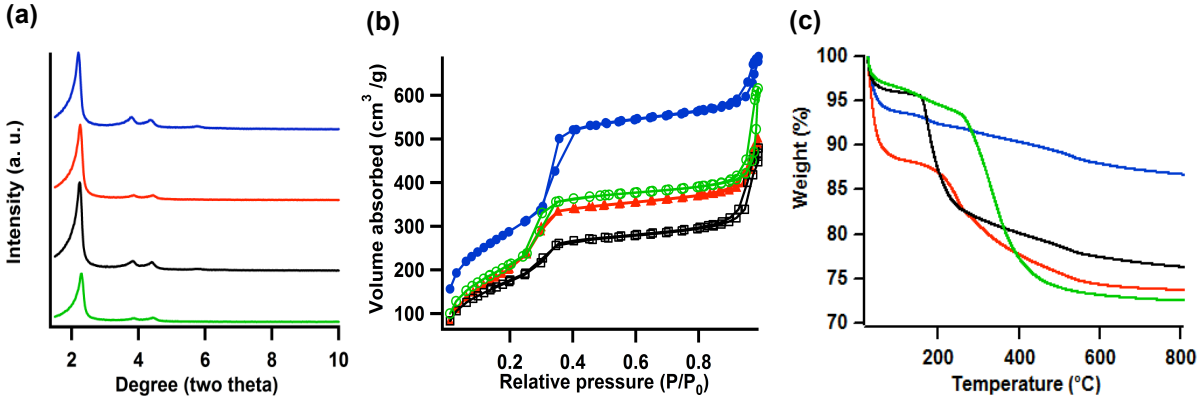

Figure S6. (a) X-ray diffraction (XRD) patterns, (b) linear plot of the nitrogen sorption isotherms and (c) thermogravimetric analysis (TGA) of *s*-MSN (blue), $AP_{1.5}$-*s*-MSN (red), PEG_1-*s*-MSN (black) and $CA_{1.5}$-*s*-MSN (green).

Table S2. Characteristics of *s*-MSN, $AP_{1.5}$-*s*-MSN, PEG_1-*s*-MSN, $CA_{1.5}$-*s*-MSN and *l*-MSN.

Materials	**Surface groups (mmol g^{-1})**	**Zeta potential (mV)**	**Surface area (m^2 g^{-1})**	**Pore size (nm)**	**Hydrodynamic particle size (nm)**
s-MSN		-22.2	1051.6 ± 2.2	3.1	122
$AP_{1.5}$-*s*-MSN	1.1-1.5	+5.79	780.3 ± 9.0	2.4	142
PEG_1-*s*-MSN	0.3-0.4	-11.6	650.5 ± 2.9	2.7	122
$CA_{1.5}$-*s*-MSN	0.6-0.9	-43.1	792.9 ± 4.4	2.9	142
l-MSN		-16.5	387.0 ± 1.3	9.0	531

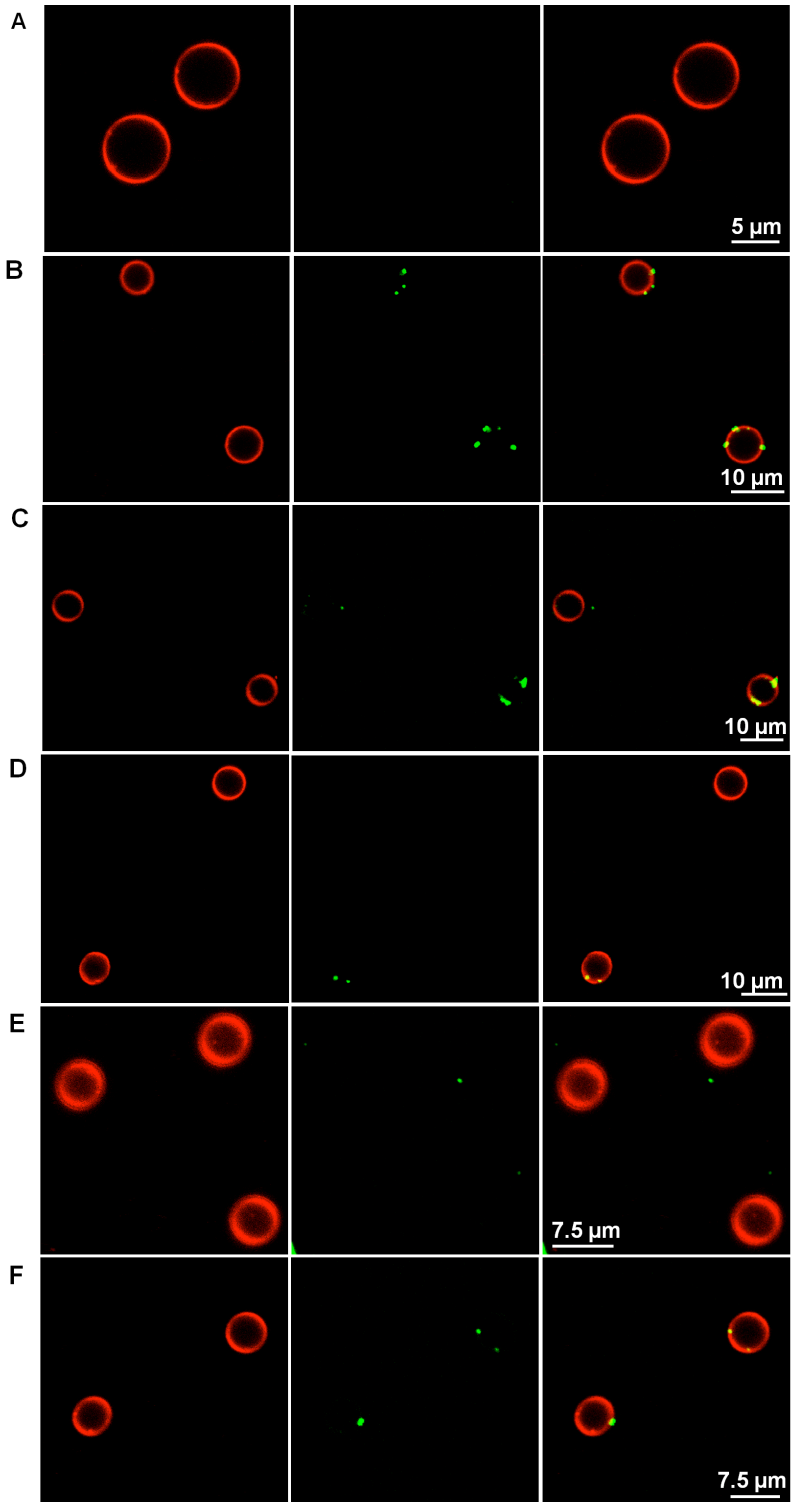
A
5 µm
B
10 µm
C
10 µm
D
10 µm
E
7.5 µm
F
7.5 µm

Figure S7. Confocal fluorescence micrographs of (A) RBCs (5×10^6 cells mL^{-1}) incubated with 20 μg mL^{-1} of (B) FITC-*l*-MSN, (C) FITC-*s*-MSN, (D) $AP_{1.5}$-FITC-*s*-MSN, (E) PEG_1-FITC-*s*-MSN and (F) $CA_{1.5}$-FITC-*s*-MSN. The channels from left to right correspond to red blood cells stained with PKH26 red fluorescence dye, FITC-MSNs and the merged images.

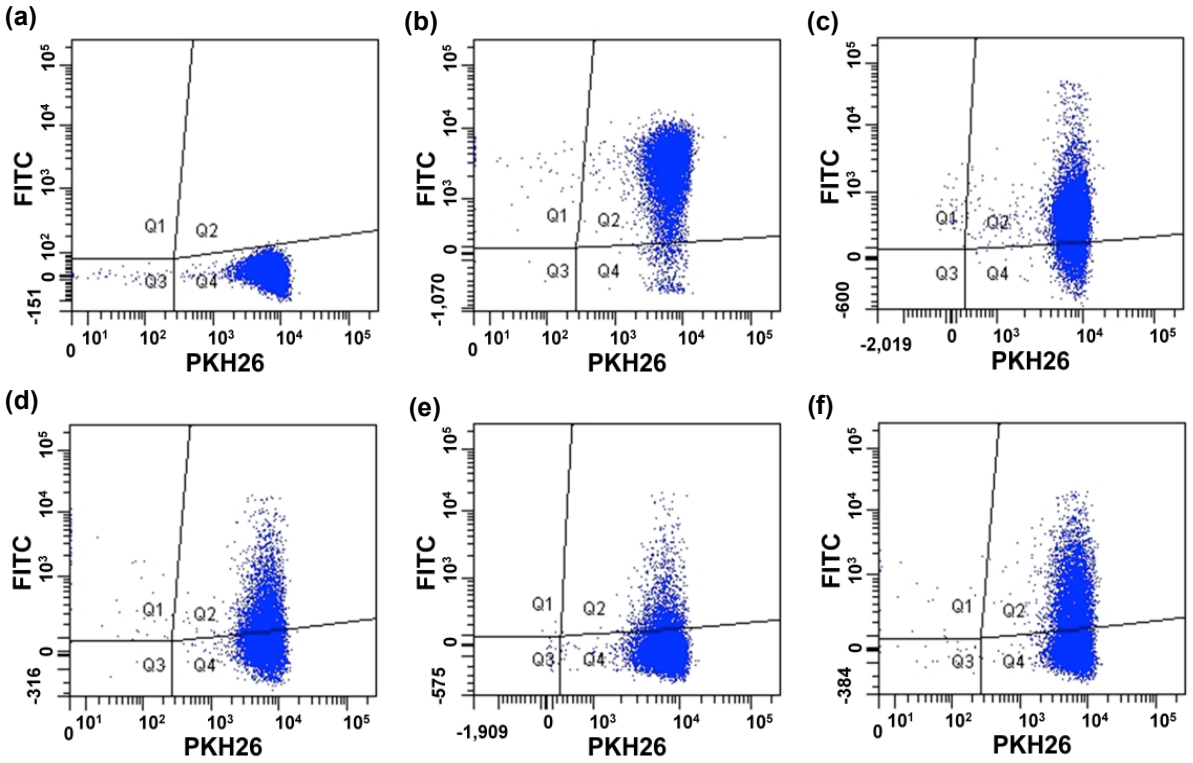

Figure S8. Dot plot from the flow cytometry analysis of (a) PKH26 labled RBC incubated with (b) FITC-*l*-MSN, (c) FITC-*s*-MSN, (d) $AP_{1.5}$-FITC-*s*-MSN, (e) PEG_1-FITC-*s*MSN and (f) $CA_{1.5}$-FITC-*s*-MSN. The axes correspond to the intensity of red fluorescence due to PKH26 labeling (horizontal axis) and green fluorescence due to the attachment of FITC-MSNs onto PKH26-RBCs (vertical axis). The plot was gated to show PKH26 labeled RBCs in area Q4 and FITC-fluorescent PKH26-RBCs in area Q2.

CHAPTER 5. BIOCOMPATIBLE MESOPOROUS SILICA NANOPARTICLES WITH DIFFERENT MORPHOLOGIES FOR ANIMAL CELL MEMBRANE PENETRATION

A paper published in ***Chemical Engineering Journal***, **2008**, *137*, 23-29.

Brian G. Trewyn, Jennifer A. Nieweg, Yannan Zhao and Victor S.-Y. Lin

Abstract

Two MCM-41 type, fluorescein-labeled mesoporous silica nanomaterials (MSNs) consisting of spherical and tube-shaped particles were synthesized and characterized. Both materials have hexagonally arranged mesopores with high surface area (> 950 m^2/g) and a narrow distribution of pore diameters. The cellular uptake efficiency and kinetics of both MSNs were measured in a cancer cell line (CHO) and a normal cell line (fibroblasts) by flow cytometry and fluorescence confocal microscopy. The correlation between the particle morphology and aggregation of MSNs to the effectiveness of cellular uptake was investigated. We envision that our study on the morphology dependent endocytosis of MSNs would lead to future developments of efficient transmembrane nanodevices for intracellular sensing and gene/drug delivery.

1. Introduction

Since the discovery of surfactant-templated synthesis of mesoporous silica materials in 1992,[1,2] many reports in the literature have explored the functionalization and utilization of these structurally ordered materials for applications in a variety of areas, such as catalysis,[3-5]

separation,[6,7] and sensor.[8,9] The unique properties, such as high surface area (> 700 m^2 g^{-1}), large pore volume (> 0.9 cm^3 g^{-1}), tunable pore size with a narrow distribution (2-10 nm), and good chemical and/or thermal stability, of these silica materials also make them potentially suitable for several important biological applications, such as drug delivery, imaging, and controlled release/sequestration.[10-16]

While several research groups worldwide have investigated the controlled release properties of various mesoporous silica materials, the amorphous nature of these materials make them difficult to handle under physiological conditions. The random aggregation of the amorphous and polydisperse particles of mesoporous silicas in aqueous solutions with high ionic strength complicates their circulation lifetime and cell membrane permeability. Because of these issues, it is difficult to predict and regulate the biocompatibility of amorphous mesoporous silica materials both *in vitro* and *in vivo*. In contrast, surface-functionalized solid silica particles with spherical shape and narrow size distribution have been used for biological applications.[17-20]

To construct mesoporous silica-based functional materials for practical applications in biotechnology and biomedicine, the ability of controlling the particle morphology and surface property of these materials is of fundamental importance. Several recent reports on the morphology control and surface functionalization of mesoporous silica nanoparticle (MSN) materials have shown promising results in improving their *in vitro* biocompatibility and cell membrane permeability.[9,21-24] In particular, the recent demonstrations on the endocytosis of these MSN particles into animal and plant cells highlight the possibility of designing nanodevices for controlling cell membrane traffic,[23] which would allow efficient deliveries of a variety of biogenic molecules into cell bodies.

To date, only spherical MSNs with an average particle size around 100-200 nm have been investigated for the endocytosis of live cells.[23] To further advance this burgeoning field of research, it is important to gain fundamental insight on how the different shapes and particle sizes would impact the cell membrane permeability of mesoporous silica materials. Herein, we report on the synthesis and characterization of two kinds of mesoporous silica particles with spherical and tube-like morphologies. The cellular uptake efficiency and kinetics were measured and compared to particle size and aggregation occurrence in aqueous buffer as depicted in Figure 1. We discovered that cancer cells endocytosed both MSNs more efficiently and at a faster rate than fibroblast cells. We also discovered that the rate of endocytosis correlates with the degree of particle aggregation.

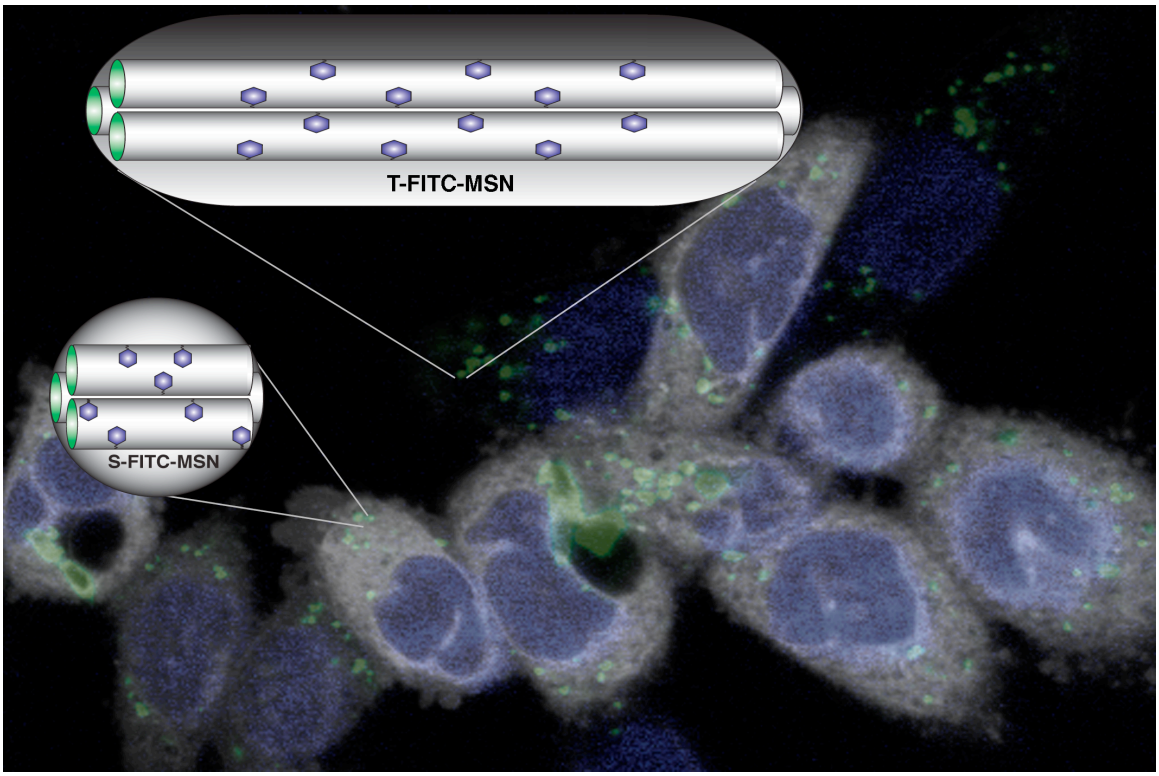

Figure 1. Schematic representation of cell uptake and internalization of spherical and tube-shaped FITC-MSN.

2. Results and Discussion

To prepare morphology controlled MSNs functionalized with fluorescein, we first reacted FITC with an aminopropyltrimethoxysilane in dry DMF to yield a trimethoxysilylated FITC. By using this compound as a precursor, a tube-shaped, FITC-labeled MSN (T-FITC-MSN) and a spherical FITC-labeled MSN (S-FITC-MSN) were successfully synthesized *via* our recently reported co-condensation method.[8,25] As shown in the SEM micrographs (Figure 2a), the S-FITC-MSN is indeed a monodisperse material consisting of spherical particles and has a narrow size distribution ranging from 80 to 150 nm in particle diameter. On the other hand, the SEM image of T-FITC-MSN confirmed the tube-like particle morphology with an average particle size of 600 nm in length and 100 nm in width (Figure 2b). Upon removal of the surfactant template via acid/methanol extraction, both T- and S-FITC-MSNs comprised of MCM-41-type, hexagonally arranged pores as determined by TEM (Figure 3a,b) and low angle powder XRD (Figure 3c). Powder XRD analysis confirms hexagonally arranged mesopores in the diffraction pattern of both MSN as evident by the intense d_{100} peak, along with a well-resolved d_{110} and d_{200} (Figure 3c). Nitrogen sorption analysis of both materials exhibited a Type-IV isotherm, typical of mesoporous material with BET surface areas measured at 951.7 ± 3.0 and 991.2 ± 3.8 m^2/g for T-FITC-MSN and S-FITC-MSN (Figure 4), respectively. The average pore diameters were determined to be 27 Å for both materials by the BJH method (Figure 4 inset).

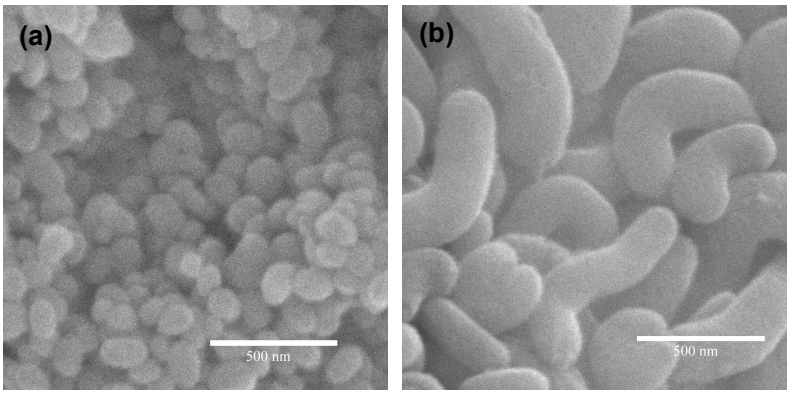

Figure 2. Scanning electron micrographs of (a) S-FITC-MSN and (b) T-FITC-MSN, giving evidence of morphology control during MSN synthesis.

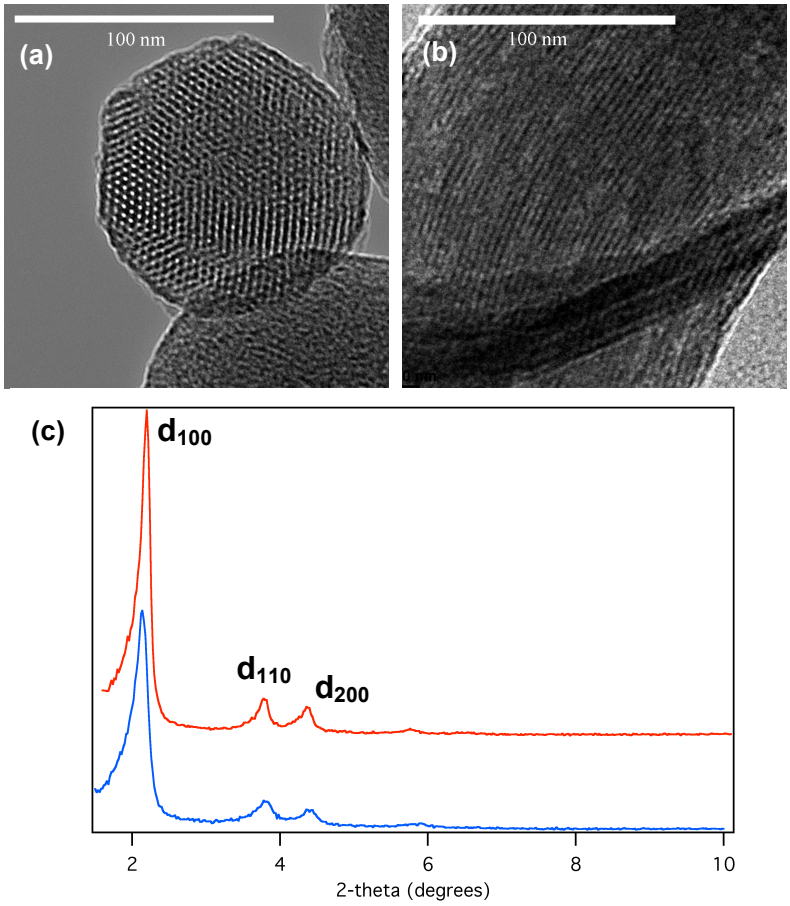

Figure 3. Transmission electron micrographs of (a) S-FITC-MSN and (b) T-FITC-MSN, showing respective particle morphologies at high magnification, and the internal mesopore structure. (c) Low angle X-ray diffraction spectra of S-FITC-MSN (blue) and T-FITC-MSN (red) measured after surfactant-template removal verifying hexagonal mesopore structures.

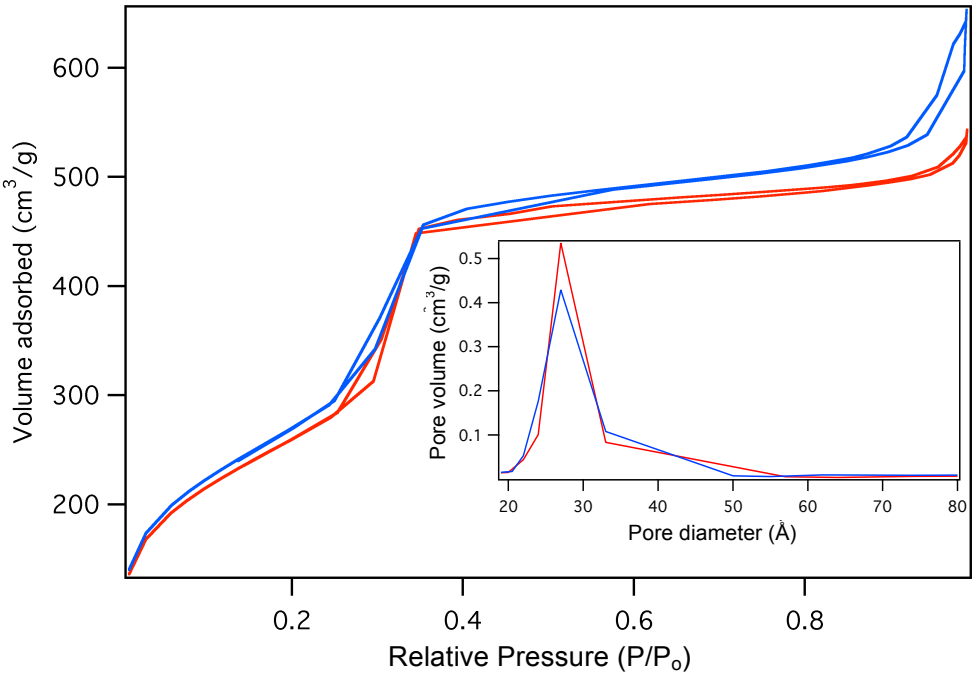

Figure 4. BET Nitrogen adsorption/desorption isotherms of S-FITC-MSN (blue) and T-FITC-MSN (red). BJH pore size distribution of S-FITC-MSN (blue) and T-FITC-MSN (red) (inset).

The cellular uptake of both materials was analyzed by flow cytometry. Both materials were covalently labeled with fluorescein as a fluorescent marker to determine the number of cells that internalized S-FITC-MSN and T-FITC-MSN. Flow cytometry neasures the fluorescence of individual cells and counts the number of cells that are above the cellular autofluorescence at each concentration of MSN. As the dosage of MSN increased, the number of cells showed a positive FITC signal also increased. We discovered that the uptake of MSN was both morphology and cell line dependent. Both materials showed more efficient uptake in the cancer cell line (CHO) than fibroblast cells (Figure 5a). In fact, T-FITC-MSN showed 100% efficient endocytosis between 50.0 and 100.0 μg mL^{-1} with an EC_{50} of 4.6 μg mL^{-1}, while S-FITC-MSN did not reach 100% efficient endocytosis below the highest measured concentration of 100.0 μg mL^{-1} and an EC_{50} of 56.0 μg mL^{-1}. However,

both materials showed less efficient endocytosis for fibroblast cells (Figure 5b). In fact, neither material reached 100% efficiency in fibroblast cells; specifically, T-FITC-MSN reached ~60% efficiency at 100.0 μg mL^{-1} with an EC_{50} of 82.0 μg mL^{-1}. S-FITC-MSN seemed to reach a maximum efficiency at 100.0 μg mL^{-1}, where 21% of the fibroblast cells showed uptake of spherical MSN. To avoid false positives, trypan blue was incorporated in the flow cytometry measurements to quench the fluorescence of MSN that were not internalized but may be attached to the outside of the cell.

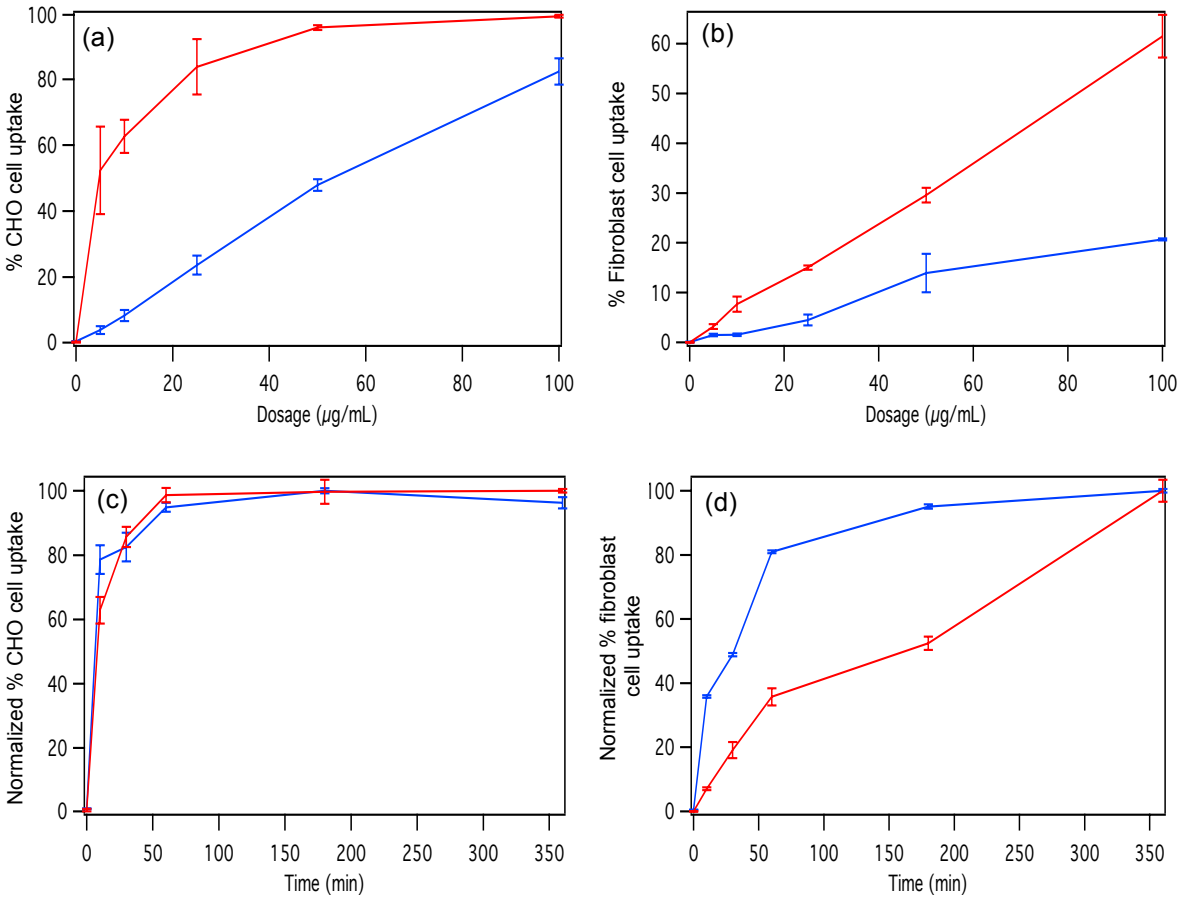

Figure 5. Dosage efficiency and kinetic measurements in CHO and fibroblast cells S-FITC-MSN (blue) and T-FITC-MSN (red). Dosage efficiency of (a) CHO and (b) fibroblast cells measured after 12 h incubation at 37 °C. Normalized endocytosis kinetics of (c) CHO and (d) fibroblast cells of 50 μg mL^{-1} incubated at 37 °C.

In addition to investigating the efficiency of endocytosis, the kinetics of endocytosis for both MSNs was studied. We discovered that the rates of endocytosis for both MSNs were similar and rapid for CHO cells (Figure 5c). However, the rates of endocytosis for fibroblast cells were different for the MSN with different morphologies. Specifically, the rate of endocytosis for S-FITC–MSN was significantly faster than that of T-FITC-MSN. In the case of S-FITC-MSN, the endocytosis reached nearly 100% uptake in 180 min, while T-FITC-MSN required 360 min to reach 100% endocytosis. This difference in endocytosis kinetics may be attributed to two variables. One is the particle size, S-FITC-MSN are much smaller as is evident from the SEM and TEM analyses (Figure 2a and 3a). The particle size of S-FITC-MSN is on the order of 80-150 nm in diameter, while T-FITC-MSN have a similar width of 80-150 nm but can vary in length. SEM and TEM data revealed that T-FITC-MSN could reach 400-1000 nm in length. This size variation may account for the difference in the rate of MSN endocytosis.

The other variable, which can also explain the difference in endocytosis kinetics, is the different aggregation ability between the MSN particles with different shapes. We have previously demonstrated that the uptake of S-FITC-MSN is a clathrin-mediated endocytosis process[23] and there are numerous examples of enhanced uptake of cancer cells and receptor overexpressed cells over noncancerous cells.[26,27]

To investigate the aggregation ability of these MSNs in aqueous solutions, the zeta potential (ζ-potential) of both materials were measured using a Malvern Nano Zetasizer to determine the surface charges that correspond to T-FITC-MSN and S-FITC-MSN. The ζ-potentials were measured to be -1.90 mV and -1.50 mV for T-FITC-MSN and S-FITC-MSN, respectively. Since the surface charges of the MSN are statistically equivalent, we assumed

that endocytosis efficiency and rate were dependent exclusively upon morphology and particle aggregation. The aggregation and particle sizes were measured using a dynamic light scattering technique. Both morphologies were discovered to aggregate at 500.0 μg mL^{-1} (Figure 6). Specifically, S-FITC-MSN showed a rather sharp peak at 712 nm, representing a small aggregation distribution while T-FITC-MSN showed a broader distribution ranging from 955 to 1480 nm. The fact that T-FITC-MSN aggregates into larger particles may be another reason for the slower cellular uptake of T-FITC-MSN.

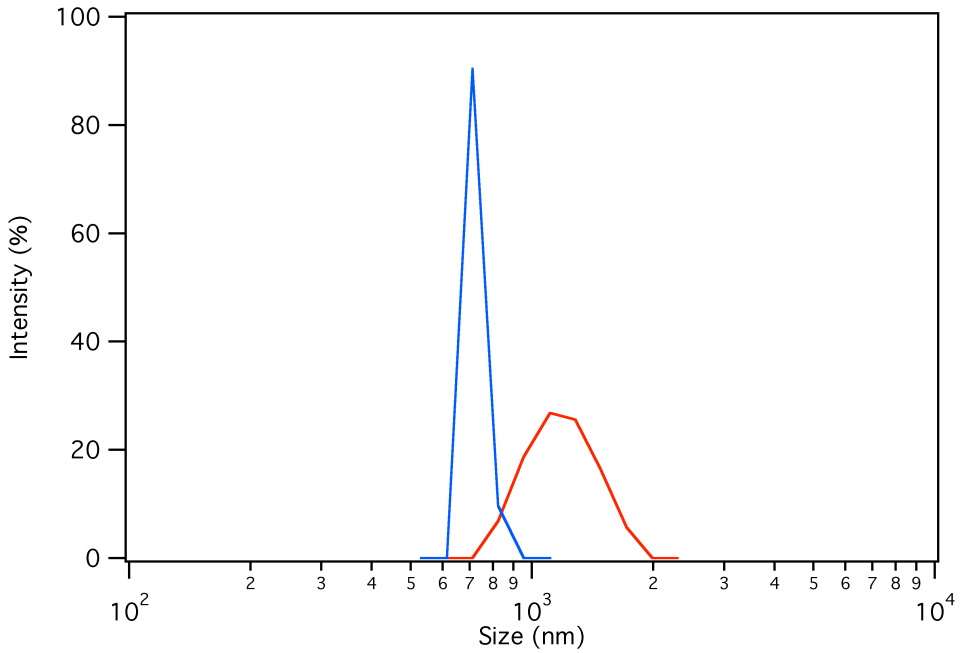

Figure 6. Dynamic light scattering data of S-FITC-MSN (blue) and T-FITC-MSN (red) measured at a concentration of 500 μg mL^{-1} in PBS.

To further investigate the cellular uptake and biocompatibility of the MSNs, CHO cells (~1 × 10^5 cells mL^{-1}) were incubated overnight (~12 h) with T-FITC-MSN and S-FITC-MSN (50.0 μg mL^{-1}). The first fluorescence confocal micrographs in each series (Figure 7a,d) showed the presence of healthy, round nuclei, stained blue by 4',6-diamidino-2-

phenylindole (DAPI) and excited at 340 nm. DAPI is a blue-fluorescent dye known to complex with double–stranded DNA. Green fluorescence from T-FITC-MSN and S-FITC-MSN were observed in the cell bodies of these CHO cells in Figure 7b and e. The DAPI and green fluorescent excited micrographs were recorded at the same focal depth. As we are able to clearly observe the nuclei, we can be assured that we are observing a focal plane that intersects the cell. The existence of oval, seemingly healthy nuclei lead us to believe that these MSN are in fact biocompatible, and do not affect the cell cycles in a detrimental way during the endocytosis process.

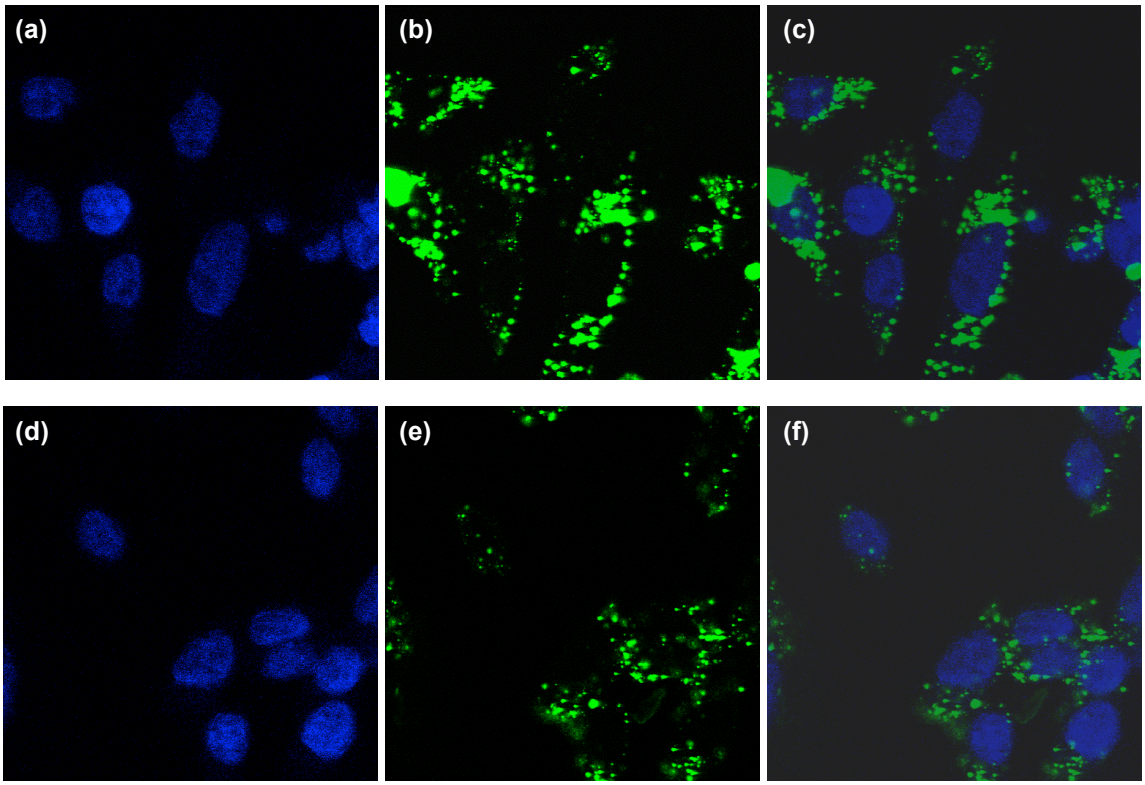

Figure 7. Fluorescence confocal micrographs of CHO cells incubated with 50 μg mL^{-1} T-FITC-MSN (a-c) and S-FITC-MSN (d-f). (a and d) Fluorescence image excited at 340 nm to visualize the cell nuclei stained with DAPI. (b and e) Fluorescence image excited at 488 nm to visualize the FITC doped MSN that have been internalized by cells. (c and f) Overlaid micrographs of a & b and d & e, respectively.

3. Conclusion

In summary, we demonstrated the endocytosis of MSN with spherical- and tube-like morphology in cancer and normal cell lines. These MSN have unique efficiencies of endocytosis, which are both morphology and cell line dependent. We have rationalized the size and aggregation tendencies to be determining factors in endocytosis efficiency and kinetics. We envision that understanding this difference in efficiency and kinetics may allow researchers to more accurately control the rate of drug and therapeutics delivery.

4. Methods

Synthesis of Spherical Fluorescein Isothiocyanate-doped MSNs (S-FITC-MSN). The MSN material was prepared by the following procedures: First, 1.0 mg fluorescein isothiocyanate was stirred for 30 min at room temperature with 5.0 mL 3-aminopropyltrimethoxysilane (APTMS) in 500.0 mL anhydrous DMF. Next, n-cetyltrimethylammonium bromide (CTAB, 1.0 g, 2.7×10^{-3} mol) was dissolved in 480.0 mL nanopure water. This solution was made basic by the addition of 3.5 mL 2.0 M NaOH, followed by adjusting the solution temperature to 353 K. Tetraethyl orthosilicate (TEOS) (5.0 mL, 2.6×10^{-3} mol) was first introduced dropwise to the CTAB-containing solution, followed by the dropwise addition of the FITC-APTMS/DMF solution. The mixture was stirred for 2 h at 353 K to give rise to orange precipitates (as synthesized S-FITC-MSNs). The solid product was filtered, washed with deionized water and methanol, and dried under high vacuum at 353 K. To remove the surfactant template (CTAB), the as-synthesized FITC-MSN (1.0 g) was refluxed for 18 h in a solution of 1.0 mL of HCl (37.4%) and 100.0 mL of methanol, followed by washing with methanol and water. The surfactant-removed FITC-

MSNs (washed S-FITC-MSNs) were placed under high vacuum to remove solvent from the mesopores, shown previously to remove surfactant to completion by ^{13}C solid state NMR.[25] The amount of fluorescein incorporated to the mesoporous material was determined to be 1.3 ± 0.5×10^{-4} mol/g by ^{29}Si direct polarization solid-state NMR using a previously reported method.[25,28]

Synthesis of Tube-shaped Fluorescein Isothiocyanate-doped MSNs (T-FITC-MSN). The MSN material was prepared by the following procedures: First, fluorescein isothiocyanate (2.0 mg) was stirred for 30 min at room temperature with 500.0 mL 3-aminopropyltrimethoxysilane (APTMS) in 500.0 mL anhydrous DMF. Next, n-cetyltrimethylammonium bromide (CTAB, 2.0 g, 5.5×10^{-3} mol) was dissolved in 480.0 mL nanopure water. This solution was made basic by the addition of 7.0 mL 2.0 M NaOH, followed by adjusting the solution temperature to 353 K. TEOS (10.0 mL, 5.1×10^{-3} mol) was first introduced quickly to the CTAB-containing solution, followed by the rapid addition of the FITC-APTMS/DMF solution. The mixture was stirred for 2 h at 353 K to give rise to orange precipitates (as synthesized T-FITC-MSN). The solid product was filtered, washed with deionized water and methanol, and dried in under high vacuum at 353 K. To remove the surfactant template (CTAB), the as-synthesized FITC-MSN (1.0 g) was refluxed for 18 h in a solution of 1.0 mL of HCl (37.4%) and 100.0 mL of methanol, followed by washing with methanol and water. The surfactant-removed FITC-MSNs (washed T-FITC-MSN) were placed under high vacuum to remove solvent from the mesopores. The amount of fluorescein incorporated to the mesoporous material was determined to be 1.1 ± 0.6×10^{-4} mol/g by ^{29}Si direct polarization solid-state NMR using a previously reported method.[25,28]

Reagents and Materials for Biological Studies. Chinese Hamster Ovarian (CHO) and Human fibroblast cell lines were obtained from American Tissue Culture Collection (ATCC). Formaldehyde solution (37% w/w) was purchased from Fisher. 4,6-Diamidino-2-phenylindole, dihydrochloride (DAPI) and trypan blue were purchased from Sigma-Aldrich. Trypsin (1×, 0.25%) in 0.1% EDTA-Na without calcium and magnesium was purchased from Fisher Scientific.

Cell Line Maintenance. CHO and fibroblast cells were maintained in T75 flasks using DMEM (Dulbucco's modified Eagle's medium) supplemented with 10% equine serum, 2 mM L-glutamine, 100 U mL^{-1} penicillin, 100 mg mL^{-1} streptomycin, and 1 mg mL^{-1} gentamycin. CHO and fibroblast cells were split every 2-3 days.

Measuring the Dosage of Spherical-FITC-MSN and Tubular-FITC-MSN Uptake. To investigate the maximum amount of material that can be incorporated by CHO and fibroblast cells, a dosage experiment was designed. The cells were grown in 6-well plates for 24 h or until visual confluency developed. The cells were then treated with incremental amounts of T-FITC-MSN and S-FITC-MSN suspended in media. Experiments were designed for both T-FITC-MSN and S-FITC-MSN with concentrations of 0, 5, 10, 25, 50, and 100 mg mL^{-1}. The cells were incubated with the different concentrations of MSNs for 12 h at 37 °C in 5% CO_2. After 12 h, the cells were washed two times with PBS (phosphate-buffered saline) and trypsinized. The cells were incubated in 830 mM trypan blue for 10 min to quench the fluorescence of any MSNs adhered to the exterior of the cells. The MSN uptake was measured by flow cytometry.

Measuring the Kinetics of Spherical-FITC-MSN and Tubular-FITC-MSN Uptake. To investigate the rate of MSN uptake into CHO and fibroblast cells, a kinetic

experiment study was conceived. The cells were grown in 6-well plates for 24 h, or until visual confluency developed. The cells were incubated with a uniform amount of MSNs (50 mg mL^{-1}) for varying amounts of time. Uptake was measured at 0, 10, 30, 60, 180, and 360 min time intervals. After the pre-determined amount of time, the cells were washed twice with PBS, and incubated in standard growth media. Fourteen hours after initial inoculation, the cells were trypsinized, and the MSN uptake was measured by flow cytometry.

Fluorescence Confocal Microscopy Measurements. To visually investigate the endocytosis of T-FITC-MSN and S-FITC-MSN, fluorescence confocal microscopy was employed. Coverslips (22 mm^2) were cleaned with 1.0 M HCl, nanopure water (3×), 50% ethanol, 70% ethanol, and 100% ethanol, and dried overnight at 60 °C. Following cleaning, the coverslips were placed on the bottom of the wells of 6-well plates and covered with 3.0 mL of standard growth media. CHO (1.0×10^5 cells mL^{-1}) were grown for 24 h on the coverslips. After 24 h, the cells were inoculated with 50.0 mg mL^{-1} MSNs, and grown for an additional 12 h. Afterwards, the growth media was removed, the cells were washed with PBS (2×), and the cells were then reincubated with a PBS solution of 3.7% formaldehyde and 57.0 mM DAPI for 30 min. These coverslips were removed from the PBS solution and fixed to glass slides with liquid adhesive.

Nitrogen adsorption/desorption isotherms. Surface analysis of the T- and S-FITC-MSN materials was performed by nitrogen sorption isotherms in a Micromeritics Tristar 3000 sorptometer. The surface areas were calculated by the Brunauer-Emmett-Teller (BET), and the pore size distribution was calculated by the Barrett-Joyner-Halenda method.

X-ray diffraction measurement. X-ray diffraction patterns of the MSN materials were obtained in a Scintag XDS-2000 powder diffractometer using Cu Kα irradiation. Both

materials possess a hexagonal structure typical of MCM-41 with three characteristic d_{100}, d_{110}, and d_{200} peaks.

ζ-Potential measurement. **T**he ζ-potential of the MSN materials was measured in a Malvern Nano HT Zetasizer. 500.0 μg/mL suspensions of each of the materials in phosphate buffer saline buffer were prepared. The pH 7.5 buffer was composed of 2.7 mM KCl, 1.5 mM KH_2PO_4, 136.0 mM NaCl and 8.1 mM $Na_2HPO_4 \cdot 7H_2O$ in nanopure water.

Scanning and transmission electron microscopy. Particle morphology was studied with a JEOL 840A scanning electron microscope with a 10 kV acceleration voltage. For transmission electron microscopy measurements, an aliquot of the powder was sonicated in nanopure water for 15 min. A single drop of this suspension was placed on a lacey carbon coated copper TEM grid and dried in air. The TEM examination was completed on a Tecnai G2 F20 electron microscope operated at 200 kV to examine at electron optical magnification of 64,000 to 550,000.

ACKNOWLEDGEMENT

The authors thank U.S. NSF (CHE-0239570), U.S. DOE, Office of Basic Energy Sciences (DE-AC02-07CH11358), and the Plant Science Institute at Iowa State University for financial support.

REFERENCES

(1) Beck, J. S.; Vartuli, J. C.; Roth, W. J.; Leonowicz, M. E.; Kresge, C. T.; Schmitt, K. D.; Chu, C. T. W.; Olson, D. H.; Sheppard, E. W.; et al. *J. Am. Chem. Soc.* **1992**, *114*, 10834.

(2) Kresge, C. T.; Leonowicz, M. E.; Roth, W. J.; Vartuli, J. C.; Beck, J. S. *Nature (London)* **1992**, *359*, 710.

(3) Chen, H.-T.; Huh, S.; Wiench, J. W.; Pruski, M.; Lin, V. S. Y. *J. Am. Chem. Soc.* **2005**, *127*, 13305.

(4) Huh, S.; Chen, H.-T.; Wiench, J. W.; Pruski, M.; Lin, V. S. Y. *Angew. Chem., Int. Ed.* **2005**, *44*, 1826.

(5) Huh, S.; Chen, H.-T.; Wiench, J. W.; Pruski, M.; Lin, V. S. Y. *J. Am. Chem. Soc.* **2004**, *126*, 1010.

(6) Mehraban, Z.; Farzaneh, F. *Microporous Mesoporous Mater.* **2006**, *88*, 84.

(7) Zhao, Y. X.; Ding, M. Y.; Chen, D. P. *Anal. Chim. Acta* **2005**, *542*, 193.

(8) Lin, V. S. Y.; Lai, C.-Y.; Huang, J.; Song, S.-A.; Xu, S. *J. Am. Chem. Soc.* **2001**, *123*, 11510.

(9) Radu, D. R.; Lai, C.-Y.; Jeftinija, K.; Rowe, E. W.; Jeftinija, S.; Lin, V. S. Y. *J. Am. Chem. Soc.* **2004**, *126*, 13216.

(10) Lai, C.-Y.; Trewyn, B. G.; Jeftinija, D. M.; Jeftinija, K.; Xu, S.; Jeftinija, S.; Lin, V. S. Y. *J. Am. Chem. Soc.* **2003**, *125*, 4451.

(11) Mal, N. K.; Fujiwara, M.; Tanaka, Y. *Nature (London)* **2003**, *421*, 350.

(12) Nguyen, T. D.; Tseng, H.-R.; Celestre, P. C.; Flood, A. H.; Liu, Y.; Stoddart, J. F.; Zink, J. I. *Proc. Natl. Acad. Sci. U.S.A.* **2005**, *102*, 10029.

(13) Trewyn, B. G.; Whitman, C. M.; Lin, V. S. Y. *Nano Lett.* **2004**, *4*, 2139.

(14) Vallet-Regi, M.; Ramila, A.; del Real, R. P.; Perez-Pariente, J. *Chem. Mater.* **2001**, *13*, 308.

(15) Giri, S.; Trewyn, B. G.; Stellmaker, M. P.; Lin, V. S. Y. *Angew. Chem., Int. Ed.* **2005**, *44*, 5038.

(16) Ramila, A.; Munoz, B.; Perez-Pariente, J.; Vallet-Regi, M. *J. Sol.-Gel Sci Technol.* **2003**, *26*, 1199.

(17) Xing, X.; He, X.; Peng, J.; Wang, K.; Tan, W. *J. Nanosci. Nanotechnol.* **2005**, *5*, 1688.

(18) Suh, W. H.; Jang, A. R.; Suh, Y.-H.; Suslick, K. S. *Adv. Mater. (Weinheim, Germany)* **2006**, *18*, 1832.

(19) Gemeinhart, R. A.; Luo, D.; Saltzman, W. M. *Biotechnol. Prog.* **2005**, *21*, 532.

(20) Lu, C.-W.; Hung, Y.; Hsiao, J.-K.; Yao, M.; Chung, T.-H.; Lin, Y.-S.; Wu, S.-H.; Hsu, S.-C.; Liu, H.-M.; Mou, C.-Y.; Yang, C.-S.; Huang, D.-M.; Chen, Y.-C. *Nano Lett.* **2007**, *7*, 149.

(21) Huang, D.-M.; Hung, Y.; Ko, B.-S.; Hsu, S.-C.; Chen, W.-H.; Chien, C.-L.; Tsai, C.-P.; Kuo, C.-T.; Kang, J.-C.; Yang, C.-S.; Mou, C.-Y.; Chen, Y.-C. *FASEB J.* **2005**, *19*, 2014.

(22) Lin, Y.-S.; Tsai, C.-P.; Huang, H.-Y.; Kuo, C.-T.; Hung, Y.; Huang, D.-M.; Chen, Y.-C.; Mou, C.-Y. *Chem. Mater.* **2005**, *17*, 4570.

(23) Slowing, I.; Trewyn, B. G.; Lin, V. S. Y. *J. Am. Chem. Soc.* **2006**, *128*, 14792.

(24) Torney, F.; Trewyn, B. G.; Lin, V. S.-Y.; Wang, K. *Nature Nanotech.* **2007**, *2*, 295.

(25) Huh, S.; Wiench, J. W.; Yoo, J.-C.; Pruski, M.; Lin, V. S. Y. *Chem. Mater.* **2003**, *15*, 4247.

(26) Kohler, N.; Sun, C.; Wang, J.; Zhang, M. *Langmuir* **2005**, *21*, 8858.

(27) Steinhauser, I.; Spaenkuch, B.; Strebhardt, K.; Langer, K.; *Biomaterials* **2006**, *27*, 4975.

(28) Huh, S.; Wiench, J. W.; Trewyn, B.G.; Song, S.; Pruski, M.; Lin, V.S.-Y. *Chem. Commun.* **2003**, *18*, 2364.

CHAPTER 6. EXOCYTOSIS OF MESOPOROUS SILICA NANOPARTICLES FROM MAMMALIAN CELLS: ASYMMETRIC CELL-TO-CELL TRANSFER

Modified from a paper accepted for publication in ***Small***.

Igor I. Slowing, Juan L. Vivero-Escoto, Yannan Zhao, Kapil Kandel, Chorthip Peeraphatdit, Brian G. Trewyn and Victor S.-Y. Lin

Abstract

Here we demonstrate how endothelial cells can take up mesoporous silica nanoparticles (MSNs) and then expel them back into the medium. The exocytosis of mesoporous silica nanoparticles (MSNs) from mammalian cells is demonstrated for the first time. The differences in the degree of exocytosis of MSNs between healthy and cancer cells are shown to be responsible for the asymmetric transfer of the particles between both cell types. This behavior demonstrates that cell specific drug delivery does not depend only on the efficiency of cellular uptake, but also on the ability of the cells to retain the drug carriers.

ARTICLE

Mesoporous silica nanoparticles (MSNs) have raised considerable interest as vehicles for drug delivery because of their capacity to encapsulate large amounts of bioactive species and the ease with which their surface can be chemically modified.[1, 2] The versatile chemistry of MSNs has enabled their functionalization with several groups to render a variety of gated nanodevices, capable of controlling the loading and release of guest molecules in a stimuli-

responsive fashion.[3-17] MSNs are readily endocytosed by animal and plant cells,[18-20] and their nanopatterned surface has proven to have a significant impact in their biocompatibility.[21, 22] All these properties have enabled the successful application of these materials to the delivery of drugs, genes and proteins into living cells, and more recently, into animal models of cancer.[1, 2, 8-10, 23-27] Since MSNs are readily taken up by a wide variety of cell types,[18-20] their use as vehicles for cell type-specific intracellular drug delivery might be conditioned to the incorporation of cell-targeting moieties.[28, 29] Cellular uptake, however, is not the only factor determining the selectivity of a drug delivery system: the relative abilities of the host cells to retain the nanoparticles also decide their ultimate fate. Herein we report an investigation on the relative abilities of healthy and cancerous cells to retain endocytosed MSNs, with the goal of further understanding the enhanced permeability and retention of nanoparticles recently observed in murine models of cancer.[27, 30, 31]

Even if the *in vitro* endocytosis and the *in vivo* administration of MSNs have been systematically investigated, it is surprising to realize there are no studies on the exocytosis or cellular transport of these particles. This lack of reports could be related to the idea that MSNs may be too large for the cells to handle. In fact, a size retention factor has been recently suggested to account for the cellular withholding of aggregates of gold nanoparticles.[32, 33] However, even if MSNs are relatively large, their cellular uptake has been repeatedly proven to be energy-dependent, which suggests that cells employ their machinery to take these particles up.[20, 29, 34]

In contrast to MSNs, the exocytosis of non-porous nanoparticles has been studied several times. Most of the reports on the exocytosis of nanoparticles have been based on two main approaches: microscopic tracking, and measurement of intra- and extra-cellular particle

concentrations.[32, 33, 35-39] These measurements have allowed the use of kinetic models to understand the dynamics of nanoparticle endo- and exocytosis.[36] Following these investigations, this study explores the role of exocytosis as a potential contributor to the enhanced permeability and retention of nanoparticles by cancer cells, which is known to take place mainly through hypervasculature.[27, 30, 31] These new results place nanoparticle exocytosis in a context, demonstrating it is not only an interesting phenomenon, but it also plays an important role in biological processes, and has the potential to lead to valuable biotechnological applications.

Before investigating the processes resulting from the exocytosis of MSNs, it was necessary to establish the timeframe in which the ejection of the particles was most likely to occur. To do so, we studied the uptake of fluorescein isothiocyanate-labeled MSNs (FITC-MSNs) by human umbilical vein endothelial cells (HUVECs) over time. These cells were chosen as models of healthy cells that surround diseased tissue in cancer. The cells were incubated in presence of the particles for increasing periods of time. The intracellular levels of FITC-MSNs were then monitored by flow cytometry, using the trypan blue exclusion method for quenching the fluorescence of extracellular particles.[40] The average fluorescence intensities of the cells suggested that the amounts of endocytosed FITC-MSNs increased gradually with time until reaching a plateau at approximately 2 h of contact (Figure 1a). This plateau can be considered as a state of equilibrium between the rates of endo- and exocytosis of the nanoparticles.[36] A similar behavior was observed when FITC-MSNs were incubated with human cervical cancer cells (HeLa) over the same period of time (Figure 1b). We also monitored the uptake of FITC-labeled MSNs by a culture of Chinese Hamster Ovarian (CHO) cells under fluorescence confocal microscope using a stage heated at 37°C. Under

these conditions it was possible to observe how a single cell used lamellipodia to drag FITC-MSNs to its body over a time span of 30 min (Figure 1c).

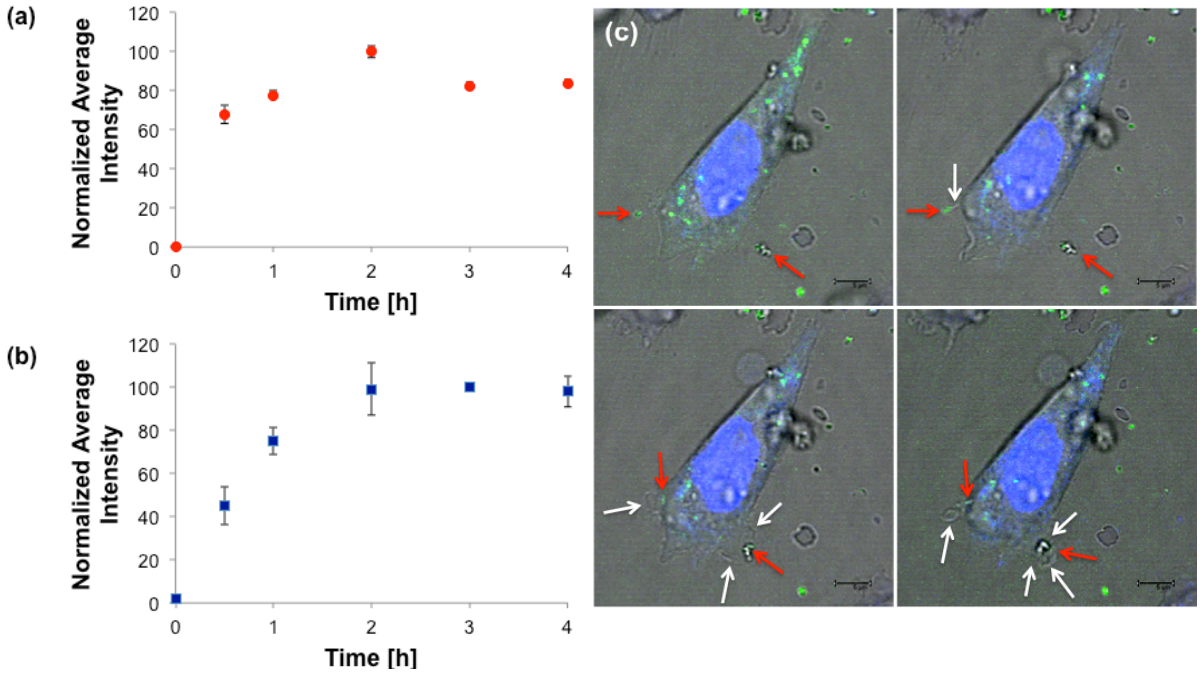

Figure 1. Changes in average fluorescence intensity of HUVEC (a) and HeLa (b) cells when incubated with suspensions of FITC-MSNs for different times. (Sample size $N = 3$). (c) Sequence of laser confocal micrographs of a chinese hamster ovarian (CHO) cell taking up two MSNs. The red arrows point to the MSNs being up taken by the cell, and the white arrows point to the lamellipodia used to capture and engulf the nanoparticles.

Based on these results we proceeded to follow the exocytosis of FITC-MSNs from particle-saturated cells under fluorescence confocal microscope. After incubating HUVECs for 3 h in presence of FITC-MSNs, the particles were observed within the cell body at the same focal plane as the cell nucleus. Upon replenishing the culture with fresh media at 37°C, the exocytosis of FITC-MSNs was observed within 40 min. As can be observed in the upper set of frames of Figure 2, the fluorescent particles were initially co-localized with the cell body. During the first 15 to 20 min, the particles migrated gradually to the boundary of the

cell membrane defining the shape of the cell (central set of frames). After some 40 min (lower set of frames of Figure 2) the labeled nanoparticles were found mainly in the extracellular space, demonstrating an active process of particle discharge. Interestingly, no exocytosis of FITC-MSNs was evident when performing the same experiment with HeLa or CHO cells. Consistent with previous observations, endocytosis of the particles was less efficient when the cell growth medium contained serum than when it was free of serum.[41] Conversely, the presence of serum in the medium favored exocytosis, as previously reported for other nanoparticles.[38]

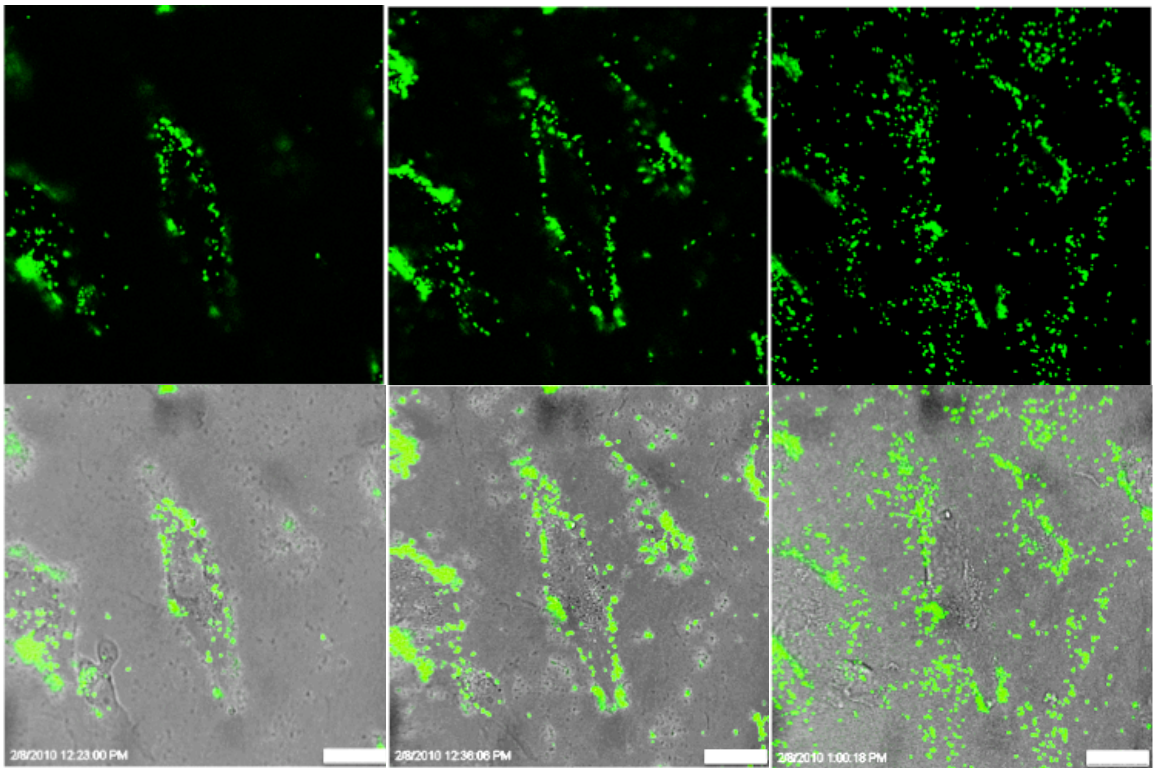

Figure 2. Laser fluorescence confocal micrographs of HUVECs pre-incubated with FITC-MSNs (green spots) after 0 (left), 13 (middle) and 37 (right) minutes of addition of fresh growth medium. The images to the top correspond to the FITC channel, and the ones to the bottom correspond to the overlay of the FITC channel with the corresponding phase contrast images. The images show the migration of the nanoparticles from the interior of the cells to the periphery and eventually to the intercellular space with time. The scale bar is 25 micrometers.

Based on these results we considered the possibility that MSNs exocytosed from one cell could be taken up by a neighboring cell. To do so we performed a series of cross-cell experiments (Scheme 1). In the first experiment, two cultures of HeLa cells were incubated for 3 h with fluorescently labeled MSNs: one using fluorescein isothiocyanate (FITC) and the other one using tetramethyl rhodamine isothiocyanate (TRITC) as a label. The cells were then washed with PBS, harvested by trypsinization, mixed and co-incubated for 20 h with serum-containing media at 37°C under 5.5% CO_2. The mixed cells were then washed, harvested and analyzed by flow cytometry.

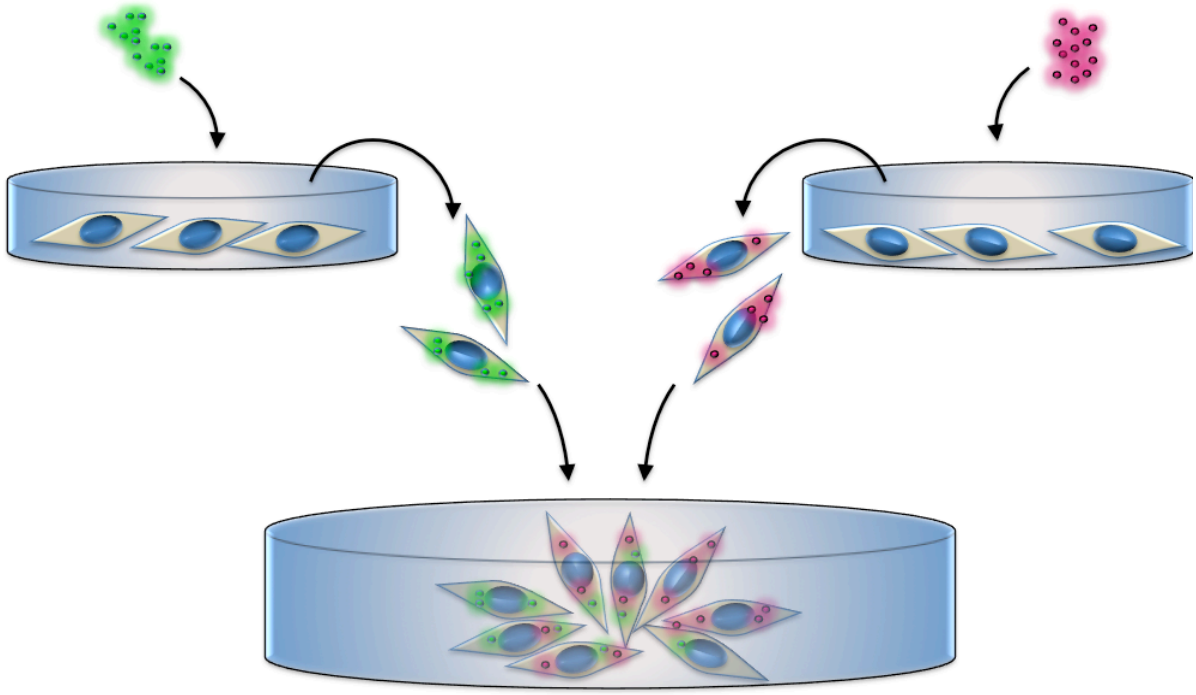

Scheme 1. Cross-cell experiments. Two cultures of cells were incubated separately, each with different labeled MSNs (FITC-MSNs one, TRITC-MSNs the other one). After uptake of the particles each culture was washed and harvested. Both cultures were then mixed and co-incubated to evaluate nanoparticle transfer between each other.

After setting gates using unlabeled cells, cells only loaded with FITC-MSNs, and cells only loaded with TRITC-MSNs as controls, it was possible to estimate that only a small fraction (12.6% ±1.6%) of the cells were FITC and TRITC positive (Figure 3a). We considered this result as a measure of the ability of the cells to exchange particles between each other. A similar result (10.9% ± 0.6%) was obtained when the experiment was performed with CHO cells. Examination under confocal microscope showed that indeed, the amount of double-labeled cells was very low (Figure 3c). When the same experiment was performed with HUVECs we observed a surprisingly large proportion of particle transfer between the cells containing FITC-MSNs and the ones containing TRITC-MSNs. The degree of transfer (89.6% ± 1.2%, Figure 3b) was seven times larger than the one observed with HeLa cells. Interestingly, the flow cytometry analysis of the mixture of HUVECs showed that instead of a single population with homogeneously distributed amounts of both labeled MSNs, two different populations could be clearly identified: one having more FITC-MSNs than TRITC-MSNs, and another one with more TRITC-MSNs than FITC-MSNs. This high efficiency of intercellular MSN transfer in HUVECs was further confirmed by confocal fluorescence microscopy (Figure 3d).

We were further interested in determining if the observed differences between the MSN-transfer capabilities of HUVECs and HeLa cells could have implications in the distribution of MSNs in a co-culture of both types of cells. For that purpose we chose to label one cell type with a long-term cell tracer dye (Cell Trace™ Far Red DDAO-SE, Invitrogen) and treat the other cell type with FITC-MSNs. Since the cell tracer is not exchanged from cell to cell, it was possible to distinguish one cell type from the other throughout the experiment. As can be observed in Figure 4a, when HUVECs were stained

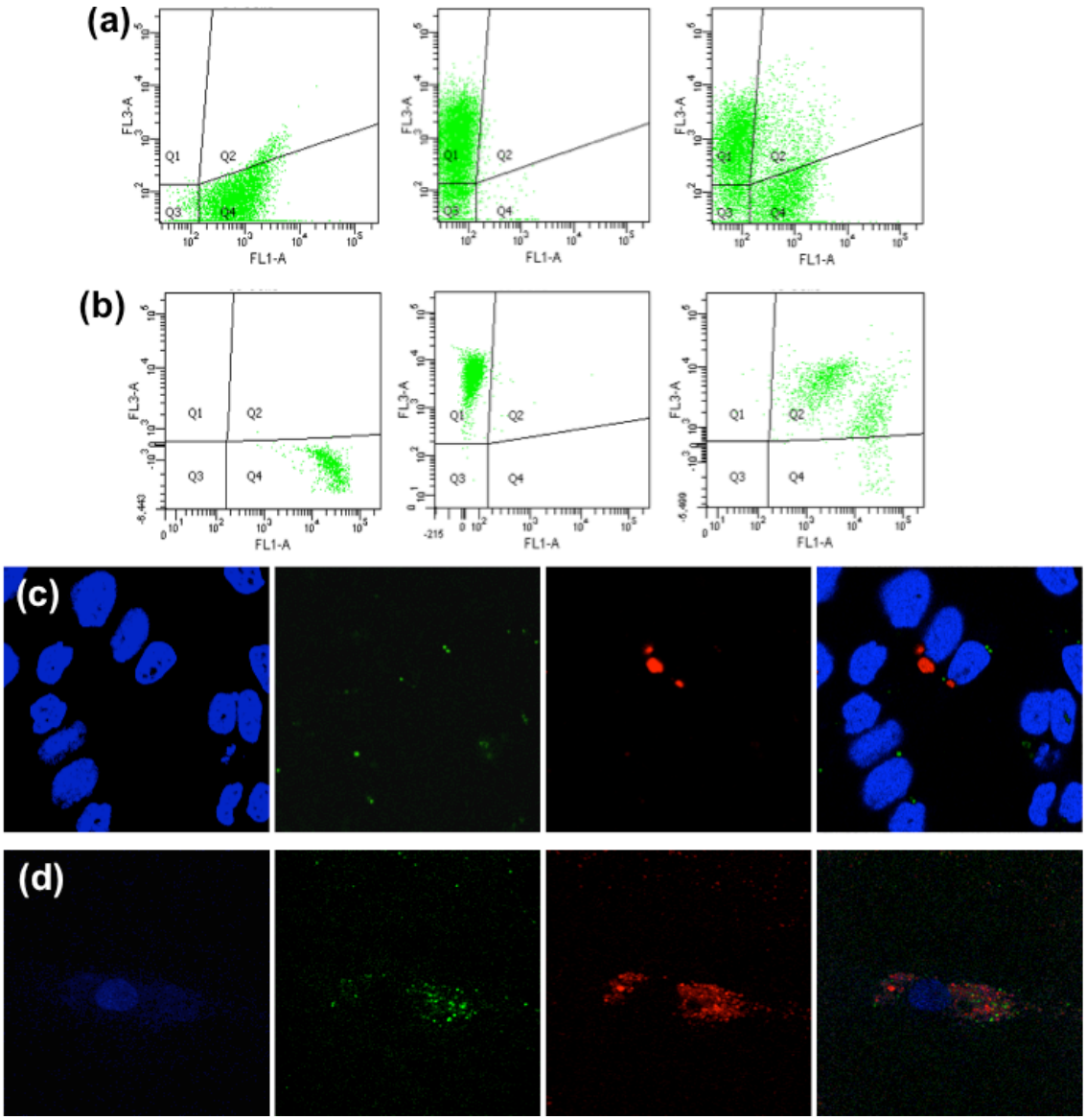

Figure 3. Dot plots from the flow cytometry analysis of the cross-cell experiments using HeLa cells (a) and HUVECs (b). The axes correspond to the intensity of green fluorescence due to uptake of FITC-MSNs (vertical axis) and of red fluorescence due to uptake of TRITC-MSNs (horizontal axis). FITC-fluorescent cells appear in area Q1, TRITC-fluorescent cells in area Q4, and cells with both fluorescent signals appear in area Q2, cells in area Q3 were FITC- and TRITC-negative as determined by a control involving non-labeled cells. Plots at the left correspond to the cells exposed only to FITC-MSNs, center plots correspond to the cells exposed only to TRITC-MSNs, and plots at the right correspond to the co-incubated cells (cross-cell experiment). Confocal fluorescence images of HeLa cells (c) and HUVECs (d) resulting from the cross-cell experiments. The channels from left to right correspond to cell nuclei stained with Hoechst 33258, FITC-MSNs, TRITC-MSNs and the merge of all images.

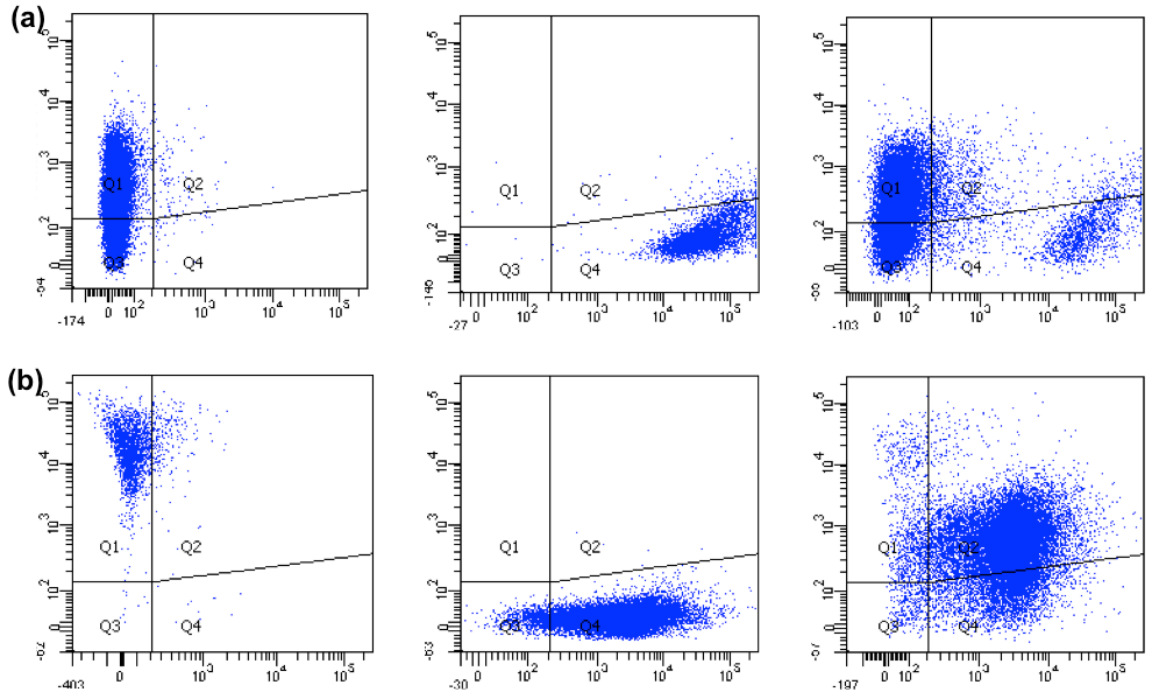

Figure 4. Cross-cell experiments between different cell types. In experiment (a) HUVECs were stained with red fluorescent cell tracer, and HeLa cells were incubated with FITC-MSNs. In experiment (b) HeLa cells were stained with the cell tracer dye and HUVECs were incubated with FITC-MSNs. The vertical axis corresponds to the intensity of green fluorescence due to uptake of FITC-MSNs and the horizontal axis to the intensity of red fluorescence due to dye-labeled cells. Area Q1 corresponds to FITC-fluorescent cells, Q4 to red-labeled cells, Q2 to cells giving both fluorescence signals. Left plots correspond to the cells exposed only to FITC-MSNs, center plots to the red-labeled cells, and the plots to the right to the co-incubated cells (cross-cell experiment). The small proportion of Q2 cells in (a) compared to the large one in (b) suggests an asymmetric nature in the transfer of MSNs between both cell types.

the tracer dye and HeLa cells were loaded with FITC-MSNs, very little particle transfer (7.5% ± 2.4%) could be observed. To the contrary, when HeLa cells were labeled with the tracer and HUVECs were loaded with the FITC-MSNs, the co-incubation of both cell types led to a large (74% ± 2.4%) amount of particle transfer (Figure 4b). It could be noted that, after transferring the FITC-MSNs to the HeLa cells, the fluorescence intensity of the HUVECs decreased, going from a relatively homogeneous distributed population (left plot)

to a much wider distribution (right plot). These results suggest a unidirectional flow in the nanoparticle transfer between the two types of cell, which is consistent with the enhanced permeability and retention recently observed for porous silicon and silica nanoparticles in murine models of cancer.[27, 31]

In conclusion, the results obtained from the studies on the dynamics of cellular uptake of MSNs and cross-cell experiments are all consistent with the hypothesis that mammalian cells can exocytose MSNs despite their relatively large size. We have demonstrated for the first time not only that exocytosis of MSNs takes place, but that there are significant differences between the abilities of different cells to retain or expel these nanoparticles, which lead to asymmetric cell-to-cell transfer of MSNs. We envision that this asymmetric transport of MSNs can have a dramatic impact in the design and use of MSNs as drug delivery agents.

METHODS

Synthesis of MSNs. MSNs were prepared by our previously reported method.[4] In brief, cetyltrimethylammonium bromide (CTAB, 1.02 g, 2.66 mmol) was dissolved in 480 cm^3 water, followed by the addition of 3.5 cm^3 sodium hydroxide solution (2 M). The mixture was heated to 80 ºC with vigorous stirring, and then 5.0 cm^3 (21.9 mmol) tetraethylorthosilicate were added drop wise. The reaction mixture was stirred at this temperature for 2 h. The resulting solid was filtered, washed thoroughly with methanol and dried under vacuum for 20 h. The CTAB surfactant was removed by refluxing 1 g of the material in 100 cm^3 of 0.37 % HCl in methanol. Fluorescent labelling was performed by reacting either fluorescein isothiocyanate (FITC) or tetramethyl rhodamine isothiocyanate

(TRITC) with (3-aminopropyl)trimethoxysilane (APTMS) for 2 h in anhydrous dimethyl sulfoxide, and adding the resulting product to the initial CTAB reaction mixture. The products were characterized by x-ray diffraction in a Rigaku Ultima IV diffractometer, by nitrogen sorption analysis in a micromeritics tristar surface area and porosity analyzer using Brunauer-Emmett-Teller equation to calculate apparent surface area and pore volume and the Barret-Joyner-Halenda method to calculate pore size distribution, and by transmission electron microscopy of samples supported on copper grids in a Tecnai G2 F20 microscope operated at 200 kV.

Cellular uptake and exocytosis studies. Cells were seeded in six-well plates and incubated at 37°C under 5.5% CO_2 in the corresponding growth media (F-12K supplemented with heparin, endothelial growth factor and fetal bovine serum for HUVEC, and DMEM supplemented with penicillin, streptomycin, gentamicin, alanyl-glutamine and equine serum for HeLa). After 24 h incubation the growth media were replaced by suspensions of 50 and 100 $\mu g\ cm^{-3}$ FITC-MSNs in the corresponding growth media, and the cells were incubated for specific times (see main text). The suspensions were then discarded, the cells were harvested by trypsinization and resuspended in trypan blue solution for flow cytometry analysis. Flow cytometry was performed in a BD FACSCanto instrument. For confocal microscopy, glass cover slips were set in the bottom of the wells of the plates followed by addition of the cells. After cell attachment, the cells were incubated with FITC-MSNs for periods of time ranging from 1 to 4 h, the nuclei were then stained with Hoechst 33258 (blue) dye. The cells were imaged in a Leica SP5 X confocal system with Leica AFS Lite 2.1.0 imaging processing software under an oil-immersion 100x objective. For monitoring

exocytosis no fixation of the cells was performed and the cells were imaged using a heated stage (37 °C).

Cross-cell experiments. For each experiment two groups of cells (either both HUVEC or HeLa, or one HUVEC and the other one HeLa) were seeded in T-25 flasks and incubated for 24 h at 37°C and 5.5% CO_2. The growth medium was removed from each flask and replaced with a suspension of the labelled MSNs in growth media (FITC-MSNs in one flask, and TRITC-MSN or Cell Trace™ Far Red DDAO-SE from Invitrogen in the other), and incubated under the same conditions for further 3 h. The cells in each flask were then harvested by trypsinization and transferred into 6-well plates with 3 cm^{-3} of fresh media. The cells were distributed in the wells in the following way: 3 wells with unlabelled cells, 3 wells with cells previously treated with FITC-MSNs, 3 wells with cells previously exposed either to TRITC-MSNs or Cell Trace dye (depending on the experiment), and 3 wells with a mixed suspension of the cells previously exposed to FITC-MSNs and the cells previously exposed to TRITC-MSNs or Cell Trace dye. The cells were incubated for further 20 hours at 37°C and 5.5% CO_2 and then harvested by trypsinization for flow cytometry analysis.

In addition, a well containing a cover slip in the bottom was also filled with the mixture of the cells exposed to FITC-MSNs and cells exposed to TRITC-MSNs and incubated under the abovementioned conditions. After 24 h, the cells attached to the cover slips were treated with the nuclear stain Hoechst 33258, followed by fixation with 3.7% formaldehyde. Then the cells in the cover slips where mounted on microscope slides and imaged under a Leica SP5 X fluorescence confocal microscope with Leica AFS Lite 2.1.0 imaging processing software.

ACKNOWLEDGMENTS

This work is dedicated to the memory of our dear colleague Dr. Victor Shang-Yi Lin. This research was supported by the U.S. National Science Foundation (CHE-0809521).

REFERENCES

(1) Lu, J.; Liong, M.; Zink, J. I.; Tamanoi, F. *Small* **2007**, *3*, 1341.

(2) Slowing, I. I.; Vivero-Escoto, J. L.; Wu, C.-W.; Lin, V. S. Y. *Adv. Drug Deliv. Rev.* **2008**, *60*, 1278.

(3) Mal, N. K.; Fujiwara, M.; Tanaka, Y. *Nature* **2003**, *421*, 350.

(4) Lai, C.-Y.; Trewyn, B. G.; Jeftinija, D. M.; Jeftinija, K.; Xu, S.; Jeftinija, S.; Lin, V. S. Y. *J. Am. Chem. Soc.* **2003**, *125*, 4451.

(5) Angelos, S.; Yang, Y.-W.; Patel, K.; Stoddart, J. F.; Zink, J. I. *Angew. Chem. Int. Ed.* **2008**, *47*, 2222.

(6) Lu, J.; Choi, E.; Tamanoi, F.; Zink, J. I. *Small* **2008**, *4*, 421.

(7) Angelos, S.; Khashab, N. M.; Yang, Y. W.; Trabolsi, A.; Khatib, H. A.; Stoddart, J. F.; Zink, J. I. *J. Am. Chem. Soc.* **2009**, *131*, 12912.

(8) Mortera, R.; Vivero-Escoto, J.; Slowing, I. I.; Garrone, E.; Onida, B.; Lin, V. S. Y. *Chem. Commun.* **2009**, 3219.

(9) Vivero-Escoto, J. L.; Slowing, I. I.; Wu, C.-W.; Lin, V. S.-Y. *J. Am. Chem. Soc.* **2009**, *131*, 3462.

(10) Zhao, Y.; Trewyn, B. G.; Slowing, I. I.; Lin, V. S. Y. *J. Am. Chem. Soc.* **2009**, *131*, 8398.

(11) Bernardos, A.; Aznar, E.; Marcos, M. D.; Martinez-Manez, R.; Sancenon, F.; Soto, J.; Barat, J. M.; Amoros, P. *Angew. Chem.-Int. Ed.* **2009**, *48*, 5884.

(12) Climent, E.; Bernardos, A.; Martinez-Manez, R.; Maquieira, A.; Marcos, M. D.; Pastor-Navarro, N.; Puchades, R.; Sancenon, F.; Soto, J.; Amoros, P. *J. Am. Chem. Soc.* **2009**, *131*, 14075.

(13) Yang, Q.; Wang, S.; Fan, P.; Wang, L.; Di, Y.; Lin, K.; Xiao, F.-S. *Chem. Mater.* **2005**, *17*, 5999.

(14) Yang, Y.; Yan, X.; Cui, Y.; He, Q.; Li, D.; Wang, A.; Fei, J.; Li, J. *J. Mater. Chem.* **2008**, *18*, 5731.

(15) Park, C.; Kim, H.; Kim, S.; Kim, C. *J. Am. Chem. Soc.* **2009**, *131*, 16614.

(16) Schlossbauer, A.; Kecht, J.; Bein, T. *Angew. Chem.-Int. Ed.* **2009**, *48*, 3092.

(17) Schlossbauer, A.; Warncke, S.; Gramlich, P.; Kecht, J.; Manetto, A.; Carell, T.; Bein, T. *Angew. Chem. Int. Ed.* **2010**, *49*, 4734.

(18) Radu, D. R.; Lai, C.-Y.; Jeftinija, K.; Rowe, E. W.; Jeftinija, S.; Lin, V. S. Y. *J. Am. Chem. Soc.* **2004**, *126*, 13216.

(19) Torney, F.; Trewyn, B. G.; Lin, V. S. Y.; Wang, K. *Nature Nanotechnol.* **2007**, *2*, 295.

(20) Huang, D. M.; Hung, Y.; Ko, B. S.; Hsu, S. C.; Chen, W. H.; Chien, C. L.; Tsai, C. P.; Kuo, C. T.; Kang, J. C.; Yang, C. S.; Mou, C. Y.; Chen, Y. C. *Faseb J.* **2005**, *19*, 2014.

(21) Slowing, I. I.; Wu, C.-W.; Vivero-Escoto, J. L.; Lin, V. S. Y. *Small* **2009**, *5*, 57.

(22) Lin, Y.-S.; Haynes, C. L. *J. Am. Chem. Soc.* **2010**, *132*, 4834.

(23) Taylor, K. M. L.; Kim, J. S.; Rieter, W. J.; An, H.; Lin, W.; Lin, W. *J. Am. Chem. Soc.* **2008**, *130*, 2154.

(24) Lee, C.-H.; Cheng, S.-H.; Wang, Y.-J.; Chen, Y.-C.; Chen, N.-T.; Souris, J.; Chen, C.-T.; Mou, C.-Y.; Yang, C.-S.; Lo, L.-W. *Adv. Funct. Mater.* **2009**, *19*, 215.

(25) Slowing, I. I.; Trewyn, B. G.; Lin, V. S. Y. *J. Am. Chem. Soc.* **2007**, *129*, 8845.

(26) Kim, J.; Kim, H. S.; Lee, N.; Kim, T.; Kim, H.; Yu, T.; Song, I. C.; Moon, W. K.; Hyeon, T. *Angew. Chem.-Int. Ed.* **2008**, *47*, 8438.

(27) Lu, J.; Liong, M.; Li, Z.; Zink, J. I.; Tamanoi, F. *Small* **2010**, *6*, 1794.

(28) Tsai, C. P.; Chen, C. Y.; Hung, Y.; Chang, F. H.; Mou, C. Y. *J. Mater. Chem.* **2009**, *19*, 5737.

(29) Slowing, I.; Trewyn, B. G.; Lin, V. S. Y. *J. Am. Chem. Soc.* **2006**, *128*, 14792.

(30) Matsumura, Y.; Maeda, H. *Cancer Research* **1986**, *46*, 6387.

(31) Park, J.-H.; Gu, L.; von Maltzahn, G.; Ruoslahti, E.; Bhatia, S. N.; Sailor, M. J. *Nat Mater* **2009**, *8*, 331.

(32) Nam, J.; Won, N.; Jin, H.; Chung, H.; Kim, S. *J. Am. Chem. Soc.* **2009**, *131*, 13639.

(33) Chithrani, B. D.; Chan, W. C. W. *Nano Lett.* **2007**, *7*, 1542.

(34) Lu, J.; Liong, M;. Sherman, S.; Xia, T.; Kovochich, M.; Nel, A.; Zink, J.; Tamanoi, F. *NanoBioTechnology* **2007**, *3*, 89.

(35) Jin, H.; Heller, D. A.; Strano, M. S. *Nano Lett.* **2008**, *8*, 1577.

(36) Jin, H.; Heller, D. A.; Sharma, R.; . Strano, M. S*ACS Nano* **2009**, *3*, 149.

(37) Stayton, I.; Winiarz, J.; Shannon, K.; Ma, Y. F. *Anal. Bioanal. Chem.* **2009**, *394*, 1595.

(38) Panyam, J.; Labhasetwar, V. *Pharm. Res.* **2003**, *20*, 212.

(39) Alberola, A. P.; Radler, J. O. *Biomater.* **2009**, *30*, 3766.

(40) Hed, J.; Hallden, G.; Johansson, S. G. O.; Larsson, P. *J. Immunol. Methods* **1987**, *101*, 119.

(41) Xing, X. L.; He, X. X.; Peng, J. F.; Wang, K. M.; Tan, W. H. *J. Nanosci. Nanotechnol.* **2005**, *5*, 1688.

Appendix: Supporting Information

1. Characterization of the materials

Mesoporous silica nanoparticles with small pores had a surface area of 971 m^2 g^{-1} (Figure S1), an average pore size of 2.7 nm (Figure S2) and a regular 2D hexagonal pore order as determined by X-ray diffraction (Figure S3) and transmission electron microscopy.

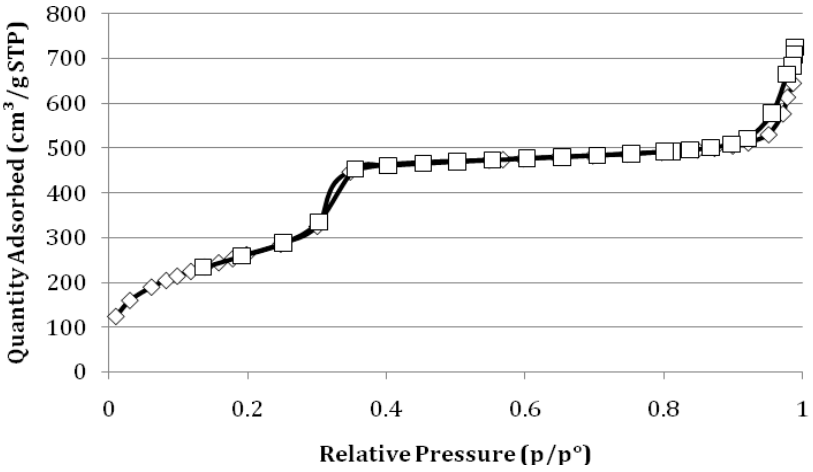

Figure S1. Linear plot of the nitrogen sorption isotherm of MSN.

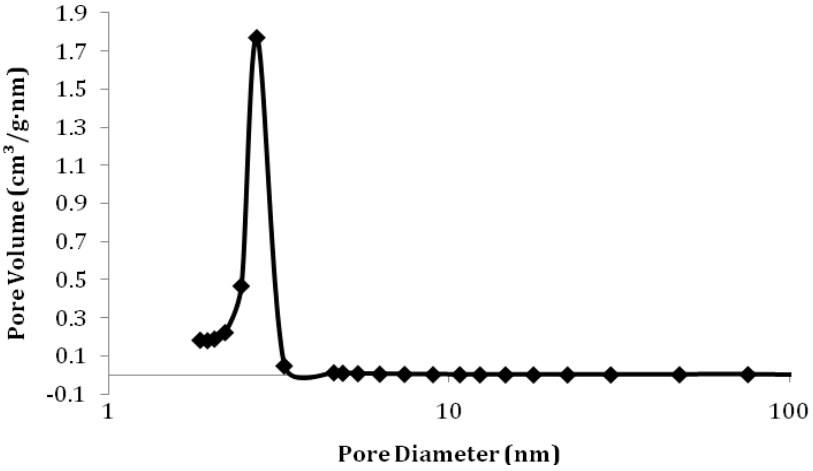

Figure S2. Pore size distribution of MSN measured by nitrogen adsorption.

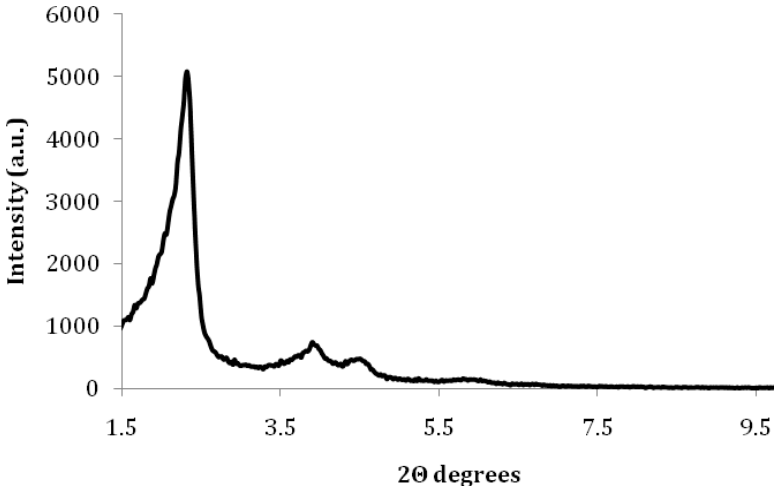

Figure S3. Small angle powder X-ray diffraction pattern of MSN.

2. Cellular trafficking studies

As mentioned above, intracellular levels of FITC-MSNs were assessed by flow cytometry. Sample histograms representing the fluorescence intensity of HUVECs incubated (Figure S4a) with FITC-labelled MSNs for times ranging from 5 minutes to 3 hours (green curves). The gray curves represent the autofluorescence of cells without FITC-MSNs. Similar histograms corresponding to HeLa cells incubated with the FITC-MSNs for the same times (Figure S4b).

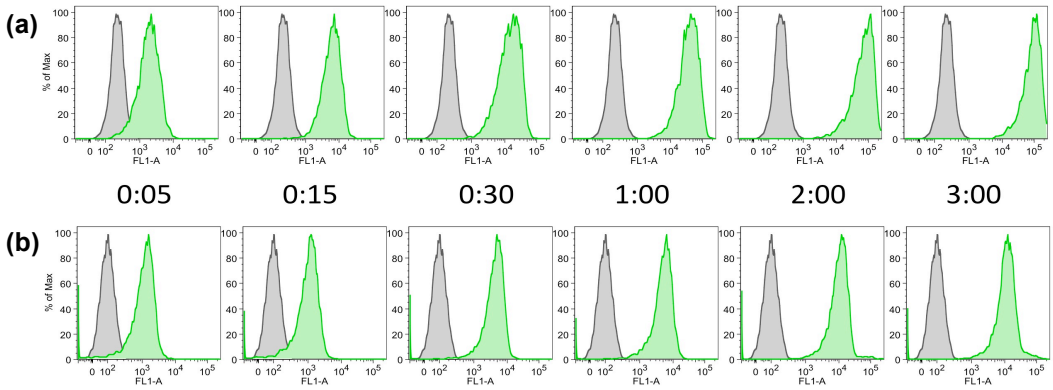

Figure S4. Sample histograms showing the shift in FITC-fluorescence for HUVEC (a) and HeLa (b) cells upon incubation for different times with FITC-MSNs.

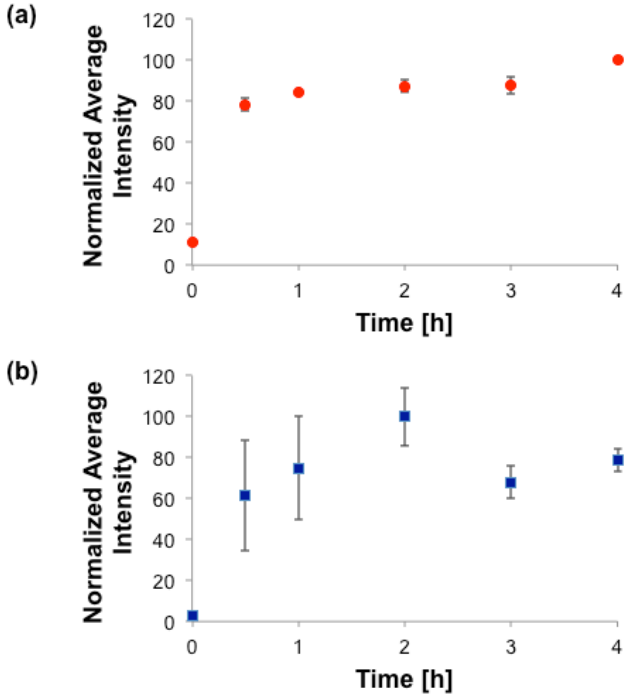

Figure S5. Changes in average fluorescence intensity of HUVEC (a) and HeLa (b) cells when incubated with suspensions of FITC-MSN-10 for different times. (Sample size $N = 3$).

MSNs have been shown previously to be non-toxic to HeLa cells at concentrations lower than 100 μg cm^{-3}.[1] The toxicity towards HUVEC was tested by incubating cultures of the cells for two days in presence of different concentrations of the material. The number of viable cells measured by flow cytometry using Guava Viacount assay (Millipore) did not change significantly at concentrations 50 μg cm^{-3}or lower compared to cells incubated in absence of the particles (Figure S6). The trypan blue exclusion assay performed with 50 μg cm^{-3} of small and large pore MSNs showed also good biocompatibility of the materials with HUVECs at this concentration (Figure S7).

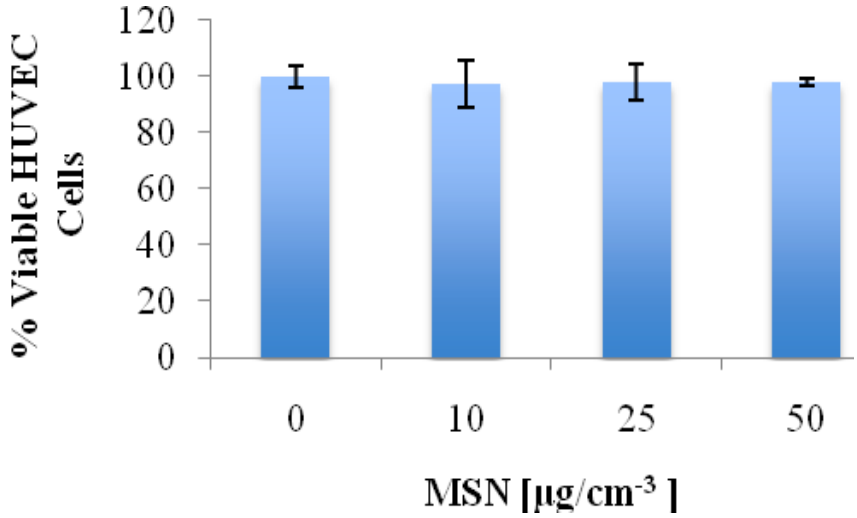

Figure S6. Guava ViaCount biocompatibility assay of MSNs with HUVECs.

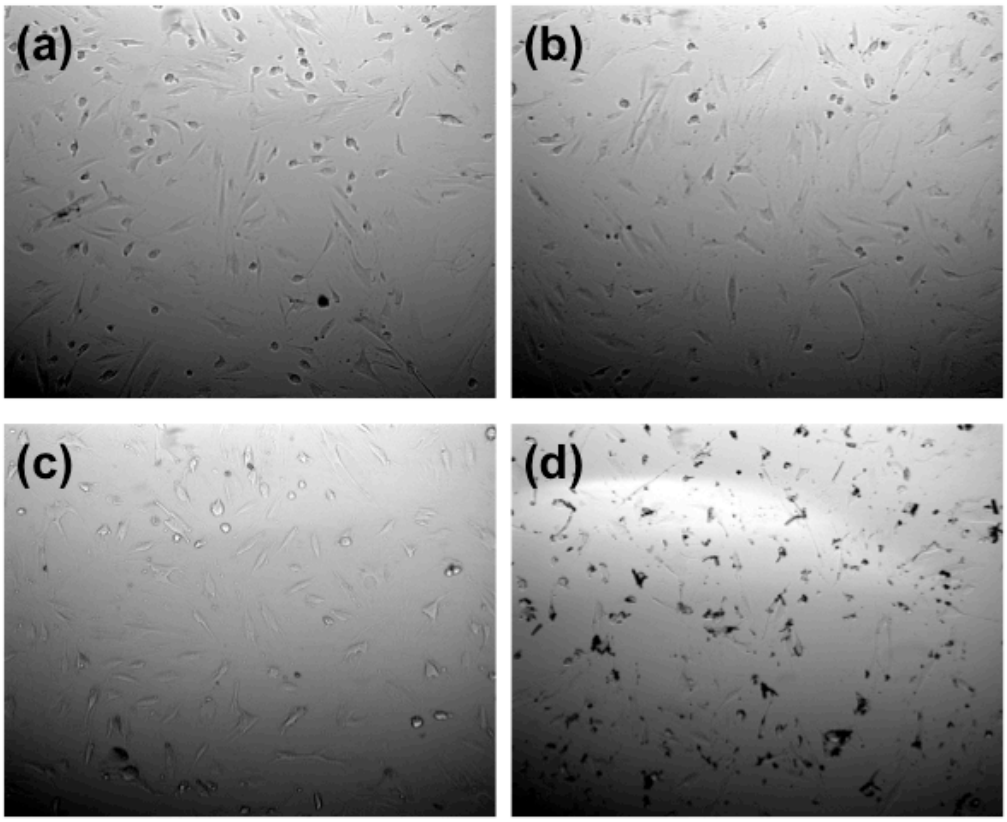

Figure S7. Phase contrast micrographs showing the trypan blue exclusion biocompatibility assay for HUVECs (a) without any MSN, incubated for 5 h with 50 µg cm^{-3} of (b) FITC-MSN, (c) FITC-MSN-10, and incubated for 30 min with 3 µM Doxorubicin. Only the last frame shows significant proportion of the dark dye in the cells.

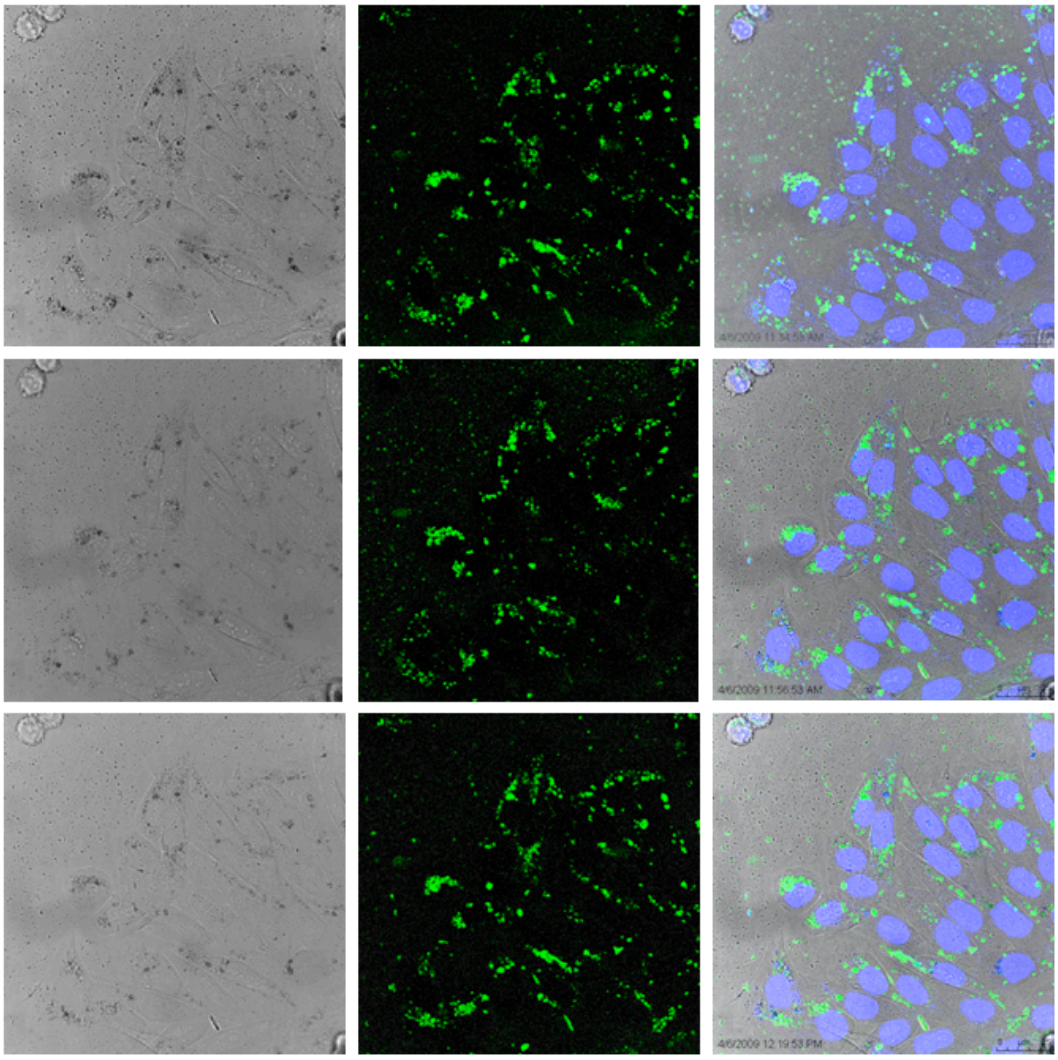

Figure S8. Confocal fluorescence microscopy images of FITC-MSN loaded HeLa cells 0, 22 and 45 minutes following incubation with FITC-MSN free medium.

References

(1) Slowing, I.; Trewyn, B. G.; Lin, V. S. Y. *J. Am. Chem. Soc.* **2006,** *128*, 14792.

CHAPTER 7. GENERAL CONCLUSIONS

The research presented in this dissertation is centered on the biomedical applications of mesoporous silica nanoparticles (MSNs), especially related to their interactions with cell membranes and uptake by live cells, as well as their potential use as drug and biomolecule delivery agents.

One of the unique features of MSN is the presence of both interior pore and exterior particle surfaces. Upon selective modification of its internal and external surface we have been able to employ MSN for the glucose-responsive co-delivery of small biomolecules and proteins with control over the sequence of release. This is accomplished by: (1) modifying insulin with gluconic acid while preserving its bioactivity to encapsulate cyclic AMP inside mesopores and also serve as a therapeutic agent to regulate blood glucose levels; (2) functionalizing the exterior surface of MSN with phenylboronic acid linkers as glucose sensors to regulate the pore opening and closing in response to blood glucose levels. A competitive binding between gluconic acid modified-insulin (G-insulin) and saccharides with phenylboronic acid resulted in the G-insulin uncapping once a higher than normal blood glucose level was encountered. Surface zeta-potential change on the G-insulin uncapping enhanced the cellular uptake of the material for efficient intracellular cAMP delivery. The fast insulin release (within 30 min) is especially important for diabetic patients requiring high dosage of insulin after meals, and the sustained intracellular release of cAMP can induce insulin production from pancreas beta cells in between meals for a long-term effect.

A preliminary condition for using MSN as intravascular biomolecule delivery agents is to understand the hemocompatibility of these materials and the factors that regulate their

interactions with blood cells. To this end, we investigated particle size- and surface-dependent interactions of MSNs with human red blood cell (RBC) membranes using fluorescence and electron microscopies and cell biology techniques, and proposed three fundamental criteria that must be assessed before performing *in vivo* studies involving the intravascular administration of nanoparticles: (1) hemolytic potential, (2) propensity to induce RBC membrane deformation or morphological alteration, and (3) tendency to impair RBC deformability. We showed how the surface of the nanoparticles can be modified to regulate their interaction with RBC membranes and improve their compatibility with RBCs, and discovered, for the first time, how MSNs are internalized by RBCs, which renders the possibility of using this material for drug delivery into non-phagocytic cells.

Another part of this dissertation consists in determining the properties that control the cellular uptake of MSN and their retention inside of living cells. We showed that the cellular uptake of MSNs is morphology and cell line dependent. Tubular MSNs were uptake up more efficiently than spherical MSNs by both cancerous and non-cancerous cells. We also observed that a cancer cell line showed a higher endocytosis efficiency and rate for both spherical and tubular particles compared with a normal cell line.

As an effort to study the relative abilities of healthy and cancerous cells to retain endocytosed MSNs and to further understand the enhanced permeability and retention of nanoparticles, we have demonstrated for the first time not only that exocytosis of MSNs takes place, but that there are significant differences between the abilities of different cells to retain or expel these nanoparticles, which lead to asymmetric cell-to-cell transfer of MSNs.

Further work is required to translate all these exciting findings to *in vivo* applications.